The Spin Structure of the Nucleon
from the SMC Experiments

Habilitationsschrift
zur Erlangung der *venia legendi*

eingereicht bei dem Fachbereich Physik (18)
der Johannes Gutenberg-Universität
in Mainz

Gerhard K. Mallot
geb. in Koblenz

August 1996

to Birgid

Contents

Chapter 1

Introduction

Deep-inelastic scattering of leptons from nucleons has revealed most of what we know about the nucleon structure in terms of quarks and gluons. It played a key rôle in establishing the existence of quarks and in the development of Quantum Chromodymamics (QCD). In the late 1960's scaling of the structure functions in terms of $\omega = 1/x$ was found [1, 2] in the scattering experiments at the 20 GeV electron beam at SLAC. The scaling behaviour had been predicted by Bjorken [3] in the limit of infinite momentum transfers, but it came as a surprise at momentum transfers of a few GeV^2. The observation of scaling revealed the existence of point-like constituents in the nucleon, the partons, and thus gave real existence to the quarks. Quarks had been postulated in 1964 by Gell–Mann and by Zweig [4] based on the symmetries observed in the hadron spectrum. Scaling is easily understood in the quark parton model devised by Feynman [5]. It describes the nucleon as a stream of point-like spin-$\frac{1}{2}$ partons, which as far as the scattering process is concerned behave like free particles. The nucleon scattering cross section is then the incoherent sum of the parton cross sections. The nucleon structure is parametrised by the parton distribution functions, $q(x)$, which are related to the probability to find a parton of a certain type carrying the faction, x, of the nucleon's momentum. Subsequently, deep-inelastic scattering experiments showed that the longitudinal-to-transverse cross section ratio, R, is small as expected for spin-$\frac{1}{2}$ particles. Experiments with (anti)neutrino beams confirmed that the nucleon contains three valence quarks and that the difference of up and down valence quarks in the proton is one. Finally, combining data from charged-lepton and neutrino scattering experiments the averaged square charge of up and down quarks was determined to be in good agreement with the expected value of 5/18. Thus an overwhelming evidence was collected that the charged partons and the quarks are identical.

With the development of QCD in 1973 [6] the asymptotic freedom of the partons could be understood. In QCD scaling violations in the structure functions are predicted due to gluon radiation [7]. These have been mapped out with high precision at the high energetic electron, muon, and neutrino beams of SLAC, CERN, and FNAL. From these measurements the momentum distribution of the gluons in the nucleon could be determined. Recently, the measurements were extended to the very small-x region at the HERA electron-proton collider. The fractions of the nucleon's momentum carried by the gluons and by the quarks consistently add up to unity. Both carry roughly 50 % of the nucleon's momentum.

The history of deep-inelastic scattering is full of surprises starting with the discovery of scaling. The classical EMC effect [8] tells us that even at high momentum transfers bound

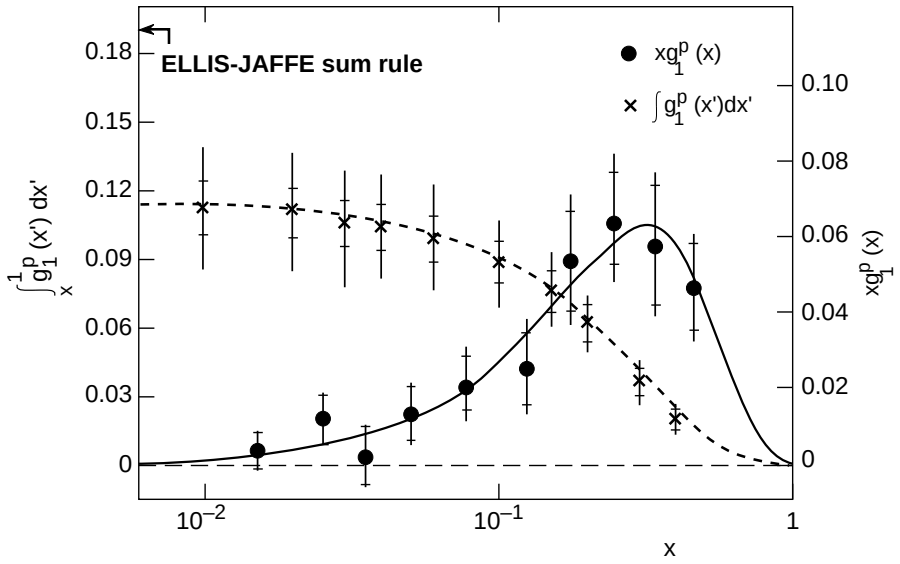

Figure 1.1: The EMC result for the Ellis–Jaffe sum rule: the structure function $xg_1^{\mathrm{p}}(x)$ (solid line) and the integral $\int_x^1 g_1^{\mathrm{p}}(x')\,\mathrm{d}x'$ (dashed line) as a function of x.

nucleons are quite different from free nucleons. Later the EMC discovered the violation of the Ellis-Jaffe sum rule [9], which implies that the nucleon spin is not primarily carried by the quark spins. Finally the violation of the Gottfried sum rule [10] taught us that the light quark sea is not flavour symmetric.

Polarised deep-inelastic scattering experiments began at SLAC shortly after the discovery of scaling. They started in 1972 with the Yale-SLAC experiment E-80 [11] and continued with the E-130 experiment [12, 13]. From the beginning the Bjorken sum rule [14], which was derived already in 1966, was one of the main objectives of the experiments [15]. However, the proposed deuteron experiments where never carried out. The proton results were consistent with quark-model predictions for the asymmetry and with the Ellis–Jaffe sum rule [16] derived in 1974 "to give the experiments something to shoot at". The SLAC experiments were limited to the kinematic range $0.1 < x$. In 1984/85 the EMC proton experiments at the 200 GeV CERN muon beam extended the kinematic range down to $0.01 < x$. The surprising result announced in 1987 [9,17] was that the Ellis–Jaffe sum rule is violated with the implication that only (12 ± 16) % of the nucleon's spin are carried by the quark spins (Fig. 1.1). Now it had become inevitable to test the Bjorken sum rule, which Bjorken initially dismissed as "worthless relation" because it is so hard to access experimentally.

The EMC result triggered a new round of experiments by the Spin Muon Collaboration (SMC) at CERN [18–22], by the E-142 [23] and E-143 [24–27] collaborations at SLAC, and by the HERMES collaboration [28] at DESY. Also an enormous theoretical effort was made to understand the implications of this measurement. It lead to new insight in the rôle of the axial anomaly and demonstrated again that "spin is an essential complication" [29].

This work originated in the Spin Muon Collaboration, of which I am a member since its beginnings in 1988. Many ideas arising from the discussions in the collaboration found the way into this paper, which is organised as follows. After this introduction a summary of some theoretical aspects is given in Chapter 2. In Chapters 3 and 4 the experiments and data analysis of the SMC are discussed in some detail. The discussion of the physics implications of the SMC results is defered to the following chapter. A review of the present status of spin structure functions, including the results from the SLAC experiments and recent developments in theory is presented in Chapter 5. The main goals of the present experiments are now achieved and further progress in the understanding of the nucleon's spin structure requires a direct measurement of the gluon polarisation. The prospects of two such projects, the COMPASS experiment at CERN and a polarised proton beam at HERA, are discussed in the last chapter before we conclude.

Chapter 2

Review of some theoretical aspects

Many good reviews and lectures on deep-inelastic scattering and structure functions exist [30–34]. Also many text books treat this subject in some detail, e.g. [35–38]. The probably most comprehensive text is the book of R. G. Roberts [39] which is entirely dedicated to this topic. In this chapter only a summary of the essential points is given.

2.1 Kinematics

In a typical fixed-target deep-inelastic-scattering experiment a lepton of energy E scatters from a nucleon or nuclear target at rest under an angle ϑ and with a final energy E'. The target remnants are not observed. Three Lorentz invariants can be constructed from these laboratory variables and the nucleon mass M.

$$q^2 = (k-k')^2 \stackrel{lab}{=} -4EE'\sin^2\frac{\vartheta}{2}, \tag{2.1}$$

$$P\cdot q \stackrel{lab}{=} M\nu = M(E-E'), \tag{2.2}$$

$$P\cdot k \stackrel{lab}{=} ME, \tag{2.3}$$

where k, k', and $P = (M,0,0,0)$ are the four-momenta of the incoming and scattered lepton and of the target nucleon, respectively. In Eq. 2.1 the lepton mass was neglected as it will be throughout this paper. The cross section can then be written as a function of the dimensionless scaling variables $0 \le x, y \le 1$

$$x = \frac{-q^2}{2P\cdot q} \stackrel{lab}{=} \frac{Q^2}{2M\nu} \tag{2.4}$$

$$y = \frac{P\cdot q}{P\cdot k} \stackrel{lab}{=} \frac{\nu}{E}. \tag{2.5}$$

This choice of variables is particularly well suited to perform the deep-inelastic limit (Bjorken limit), where both the momentum transfer, $Q^2 = -q^2 > 0$, and the energy transfer, ν, go to infinity keeping their ratio, x, constant. Other characteristic variables of the scattering process are the centre-of-mass (c.m.) energy, $\sqrt{s}$, and the c.m. energy of

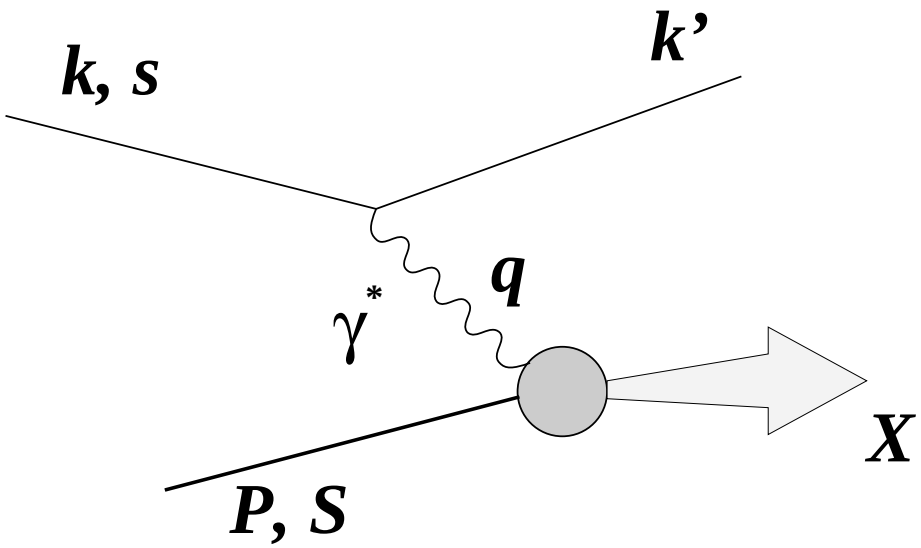

Figure 2.1: Schematic view of the deep-inelastic scattering process.

the hadronic final state, W,

$$s = (k+P)^2 = \frac{Q^2}{xy} + M^2 \tag{2.6}$$

$$W^2 = (q+P)^2 = \frac{1-x}{x}Q^2 + M^2. \tag{2.7}$$

For our experiments with 190 GeV muons the c.m. energy is $\sqrt{s} = 19$ GeV and W ranges from 18 GeV at $x = 0.003$ to $W = 5$–15 GeV at $x = 0.7$. Thus the region of nucleon resonances, $W \leq 2.5$ GeV, is well outside the entire kinematic range of the SMC experiment.

2.2 The deep-inelastic cross section

At the momentum transfers of the SMC experiment Z exchange can safely be neglected and in the following we therefore shall only consider photon exchange (Fig. 2.1). The Born cross section for inclusive inelastic scattering of a charged lepton from a nucleon $\ell \mathrm{N} \to \ell' X$, can be expressed as a product of a leptonic tensor, $l_{\mu\nu}$, and a hadronic tensor, $W^{\mu\nu}$,

$$\frac{\mathrm{d}^3\sigma}{\mathrm{d}x\,\mathrm{d}y\,\mathrm{d}\varphi} = \frac{\alpha^2}{Q^4}\frac{y}{2} l_{\mu\nu} W^{\mu\nu}, \tag{2.8}$$

with the electromagnetic fine-structure constant α. The differential cross section can be expressed in other kinematic variables using

$$\frac{\mathrm{d}^3\sigma}{\mathrm{d}x\,\mathrm{d}y\,\mathrm{d}\varphi} = \frac{M\nu}{E'}\frac{\mathrm{d}^3\sigma}{\mathrm{d}E'\,\mathrm{d}\Omega_{\mathrm{lab}}} = \nu(s-M^2)\frac{\mathrm{d}^3\sigma}{\mathrm{d}\nu\,\mathrm{d}Q^2\,\mathrm{d}\varphi} = x(s-M^2)\frac{\mathrm{d}^3\sigma}{\mathrm{d}x\,\mathrm{d}Q^2\,\mathrm{d}\varphi}, \tag{2.9}$$

where Ω_{lab} is the solid angle in the laboratory frame.

The tensors $l_{\mu\nu}$ and $W^{\mu\nu}$ involve the leptonic and hadronic electromagnetic currents, respectively. While the leptonic current is well known from QED, the hadronic current contains the unknown non-perturbative structure of the nucleon, which is the subject of our experiments. Summing over the lepton spin in the final state one obtains

$$\begin{aligned} l_{\mu\nu}(s,k;k') &= \sum_{s'}[\bar{u}(k',s')\gamma_\mu u(k,s)]^\star\,[\bar{u}(k',s')\gamma_\nu u(k,s)] && (2.10)\\ &= 2(k_\mu k'_\nu + k'_\mu k_\nu) - 2g_{\mu\nu}(k\cdot k' - m^2) + 2im\epsilon_{\mu\nu\alpha\beta}s^\alpha q^\beta && (2.11)\\ &= l^{(\mathrm{S})}_{\mu\nu}(k;k') + il^{(\mathrm{A})}_{\mu\nu}(s,k;k') && (2.12)\end{aligned}$$

with m being the lepton mass, $g_{\mu\nu}$ the metric tensor, and $\epsilon_{\mu\nu\alpha\beta}$ the fully antisymmetric Levi–Civita tensor. The polarisation vector of the lepton in its rest frame, $s = (0,\vec{s})$, can be generalised to an arbitrary Lorentz frame by

$$2ms^\mu = \bar{u}(k,s)\gamma^\mu\gamma_5 u(k,s) \qquad (2.13)$$

with $\vec{s}^{\,2} = 1$, $s^2 = -1$, and $s\cdot k = 0$. The hadronic tensor is defined by

$$\begin{aligned} W^{\mu\nu}(S,P;q) &= \frac{1}{2\pi}\sum_X \langle P,S|J^\mu(0)|X\rangle\langle X|J^\nu(0)|P,S\rangle(2\pi)^4\delta^4(P+q-p_X) && (2.14)\\ &= \frac{1}{2\pi}\int \mathrm{d}^4\xi e^{iq\xi}\langle P,S|[J^\mu(\xi),J^\nu(0)]|P,S\rangle && (2.15)\\ &= W^{\mu\nu(\mathrm{S})}(P;q) + iW^{\mu\nu(\mathrm{A})}(S,P;q), && (2.16)\end{aligned}$$

where S is the nucleon's polarisation vector and p_X is the total momentum of the final hadronic state, X. The step from Eq. 2.14 to 2.15 involves the completeness relation for the final states, X, re-writing of the delta function as a Fourier integral, and translating the hadronic current, J_μ, from 0 to ξ by the factor $e^{i\xi(P-p_X)}$. The term $J^\nu(0)J^\mu(\xi)$, which is subtracted in order to obtain the commutator in Eq. 2.15, vanishes. It corresponds to interchanging P and p_X in the delta function of Eq. 2.14, which implies the unphysical relation $E_X = M - \nu$. The scale of the distance probed in deep-inelastic scattering is determined by the space-time interval, ξ, between the points where the currents act, see Sect. 2.6. Both tensors, $l_{\mu\nu}$ and $W^{\mu\nu}$, can be split in a part symmetric (S) under exchange of the indices and an antisymmetric part (A).

Requiring Lorentz invariance, P and T invariance, and conservation of the lepton current, $q^\mu l_{\mu\nu} = 0$, the general form of the hadronic tensor for a spin-$\frac{1}{2}$ target is

$$\begin{aligned} \frac{1}{2}W^{\mu\nu(S)} &= -\left(g^{\mu\nu} - \frac{q^\mu q^\nu}{q^2}\right)F_1 + \left(P^\mu - \frac{P\cdot q}{q^2}q^\mu\right)\left(P^\nu - \frac{P\cdot q}{q^2}q^\nu\right)\frac{F_2}{P\cdot q}\\ \frac{1}{2}W^{\mu\nu(A)} &= -i\epsilon^{\mu\nu\alpha\beta}q_\alpha\left(\frac{MS_\beta}{P\cdot q}(g_1+g_2) - \frac{M(S\cdot q)P_\beta}{P\cdot q}g_2\right). && (2.17)\end{aligned}$$

The dimensionless structure functions F_1, F_2, g_1, g_2 are in general functions of $P\cdot q$ and Q^2. They are related to another commonly used set of structure functions by

$$MW_1 \equiv F_1, \qquad \nu W_2 \equiv F_2, \qquad M^2\nu G_1 \equiv g_1, \qquad M\nu^2 G_2 \equiv g_2. \qquad (2.18)$$

The differential cross section is then given by

$$\frac{\mathrm{d}^3\sigma}{\mathrm{d}x\,\mathrm{d}y\,\mathrm{d}\varphi} = \frac{\alpha^2}{Q^4}\frac{y}{2}\left(l^{(\mathrm{S})}_{\mu\nu}W^{\mu\nu(\mathrm{S})} - l^{(\mathrm{A})}_{\mu\nu}W^{\mu\nu(\mathrm{A})}\right), \qquad (2.19)$$

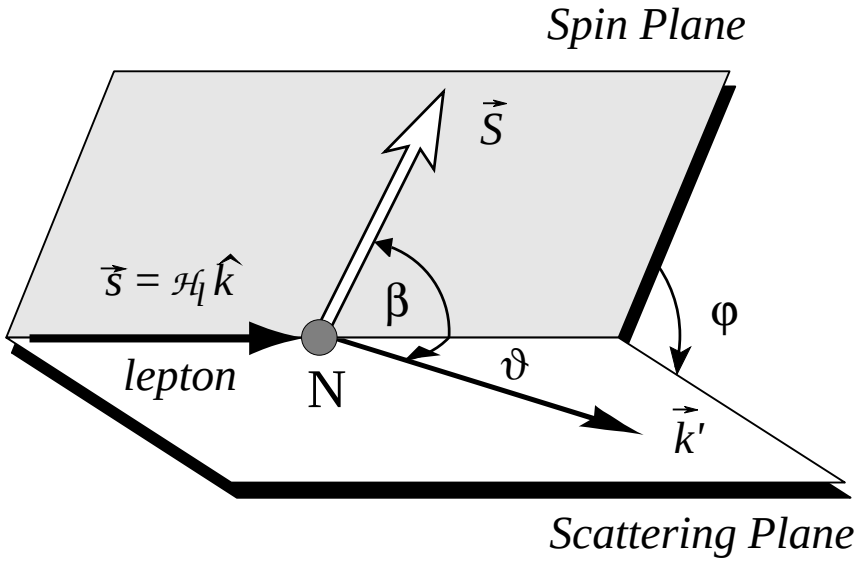

Figure 2.2: Kinematics of polarised deep-inelastic lepton-nucleon scattering.

where the first term in the parentheses corresponds to the spin-averaged and the second term to the spin-dependent part of the cross section involving both, the lepton and the nucleon polarisation vectors. Therefore spin dependent effects can only occur if both, the lepton and the hadron are polarised.

From now on we only consider longitudinal polarisation of the incoming lepton, i.e. $ms^\mu = \mathcal{H}_\ell\,(|\vec{k}|, 0, 0, E) \simeq \mathcal{H}_\ell k$ with $\mathcal{H}_\ell = \pm 1$ for right and left-handed incident leptons. In contrast to the longitudinal polarisation vector, which acquires a factor E/m by the Lorentz boost from the rest frame to laboratory frame, the transverse polarisation vector, $s = (0, s_x, s_y, 0)$, lacks this factor and is therefore suppressed like $m/E \to 0$. Finally the Born cross section has the form [40]

$$\frac{\mathrm{d}^3\sigma}{\mathrm{d}x\,\mathrm{d}y\,\mathrm{d}\varphi} = \frac{\mathrm{d}^3\overline{\sigma}}{\mathrm{d}x\,\mathrm{d}y\,\mathrm{d}\varphi} - \mathcal{H}_\ell \cos\beta \frac{\mathrm{d}^3\Delta_\parallel\sigma}{\mathrm{d}x\,\mathrm{d}y\,\mathrm{d}\varphi} - \mathcal{H}_\ell \sin\beta\cos\varphi \frac{\mathrm{d}^3\Delta_\perp\sigma}{\mathrm{d}x\,\mathrm{d}y\,\mathrm{d}\varphi}, \tag{2.20}$$

where $\overline{\sigma}$ refers to the spin-averaged cross sections and $\sigma_\parallel$ and $\sigma_\perp$ denote the cross section for longitudinal and transverse orientation of the target spin. The angle between the lepton momentum and the target spin is $0 \le \beta \le \pi$ and the azimuthal angle between the scattering plane and the plane containing the lepton and target spins is $0 \le \varphi \le 2\pi$ (Fig. 2.2). Only $\Delta_\perp\sigma$ explicitly depends on φ. The exact formulæ for the three terms (apart from the neglect of the lepton mass) are [40]

$$\frac{\mathrm{d}^3\overline{\sigma}}{\mathrm{d}x\,\mathrm{d}y\,\mathrm{d}\varphi} = \frac{4\alpha^2}{Q^2}\left\{\frac{y}{2}F_1 + \frac{1}{2xy}\left(1 - y - \frac{y^2\gamma^2}{4}\right)F_2\right\}, \tag{2.21}$$

$$\frac{\mathrm{d}^3\Delta_\parallel\sigma}{\mathrm{d}x\,\mathrm{d}y\,\mathrm{d}\varphi} = \frac{4\alpha^2}{Q^2}\left\{\left(1 - \frac{y}{2} - \frac{y^2\gamma^2}{4}\right)g_1 - \frac{y}{2}\gamma^2 g_2\right\}, \tag{2.22}$$

$$\frac{\mathrm{d}^3\Delta_\perp\sigma}{\mathrm{d}x\,\mathrm{d}y\,\mathrm{d}\varphi} = \frac{4\alpha^2}{Q^2}\left\{\gamma\sqrt{1 - y - \frac{y^2\gamma^2}{4}}\,\left(\frac{y}{2}g_1 + g_2\right)\right\}. \tag{2.23}$$

The kinematic factor $\gamma^2 = Q^2/\nu^2 = 4x^2M^2/Q^2$ vanishes for $Q^2 \to \infty$. Thus for longitudinal target polarisation ($\beta = 0°$) the structure function g_1 can be studied, while for transverse polarisation ($\beta = 90°$) the combination $\frac{y}{2}g_1 + g_2$ can be measured. Note that the transverse cross section $\Delta\sigma_\perp$ is suppressed by a factor $\gamma \propto M/Q$, which means that g_2 relates to "higher-twist" effects. Polarised deep-inelastic scattering is an ideal place to study such effects at high Q^2. They can directly be determined from the difference of longitudinal and transverse cross sections, while in most other cases they appear on top of large leading-twist contributions.

2.3 Photoabsorption

Although the equations given in the previous section are sufficient to determine the structure functions experimentally, it is illustrating to look at the scattering process in an alternative way. The differential spin-averaged cross section can be written as a product of the transverse (helicity $\lambda = \pm 1$) and the scalar (or longitudinal, $\lambda = 0$) virtual-photon flux, Γ_T and $\Gamma_S = \varepsilon\Gamma_T$, and the transverse and scalar virtual-photoabsorption cross sections, σ_T and σ_S,

$$\frac{\mathrm{d}\sigma}{\mathrm{d}E'\,\mathrm{d}\Omega_{\mathrm{lab}}} = \Gamma_T(\sigma_T + \varepsilon\sigma_S), \tag{2.24}$$

with

$$\Gamma_T = \frac{\alpha}{2\pi^2}\frac{E'}{E}\frac{K}{Q^2(1-\varepsilon)}, \qquad \varepsilon^{-1} = 1 + 2\left(1 + \frac{\nu^2}{Q^2}\right)\tan^2\frac{\vartheta}{2}. \tag{2.25}$$

The normalisation factor, K, which according to Hand's convention [41] is $K = (\nu - Q^2/2M)$, also appears in the nominator of the unphysical cross section for virtual photons

$$\sigma_\lambda = \frac{2\pi^2\alpha}{MK}\epsilon_\lambda^{\mu\star}(q)W_{\mu\nu}(S,P;q)\epsilon_\lambda^{\nu}(q) \tag{2.26}$$

and thus cancels in the physical cross section. The hadronic tensor, $W^{\mu\nu}$, is the one discussed in the previous section. For a virtual photon with $\vec{q}$ along the z-axis, i.e. $q^\mu = (\nu, 0, 0, \sqrt{\nu^2 + Q^2})$, the polarisation vectors for scalar and transverse photons are

$$\epsilon_0^\mu = \frac{1}{\sqrt{Q^2}}(\sqrt{\nu^2+Q^2}, 0, 0, \nu) \quad \text{and} \quad \epsilon_\pm^\mu = \mp\frac{1}{\sqrt{2}}(0, 1, \pm i, 0). \tag{2.27}$$

For the interaction of scalar and left and right circularly polarised photons with a spin-$\frac{1}{2}$ hadron one finds the cross sections,

$$\sigma_S^0 = \frac{4\pi^2\alpha}{MK}\left(-F_1 + \frac{F_2}{2x}(1+\gamma^2)\right) = \frac{2\pi\alpha}{MK}\,\mathrm{Im}\mathcal{A}(\,0,\uparrow;\;0,\uparrow), \tag{2.28}$$

$$\sigma_T^{\frac{1}{2}} = \frac{4\pi^2\alpha}{MK}\left(F_1 + g_1 - \gamma^2 g_2\right) = \frac{2\pi\alpha}{MK}\,\mathrm{Im}\mathcal{A}(+,\downarrow;+,\downarrow), \tag{2.29}$$

$$\sigma_T^{\frac{3}{2}} = \frac{4\pi^2\alpha}{MK}\left(F_1 - g_1 + \gamma^2 g_2\right) = \frac{2\pi\alpha}{MK}\,\mathrm{Im}\mathcal{A}(+,\uparrow;+,\uparrow), \tag{2.30}$$

$$\sigma_{TS}^{\frac{1}{2}} = \frac{4\pi^2\alpha}{MK}\gamma\,(g_1 + g_2) = \frac{\sqrt{2}\pi\alpha}{MK}\mathrm{Im}\mathcal{A}(+,\downarrow;\;0,\uparrow), \tag{2.31}$$

where $\frac{1}{2}$ and $\frac{3}{2}$ denote the initial state angular momentum along the direction of the virtual photon. It is useful to define the total transverse cross section,

$$\sigma_T = \frac{1}{2}(\sigma_T^{1/2} + \sigma_T^{3/2}) = \frac{4\pi^2\alpha}{MK}F_1, \tag{2.32}$$

which is entirely given by F_1. The term σ_{TS} corresponds to the interference of transverse and scalar photons interacting with a transversely polarised hadron. The virtual-photon cross sections are via the optical theorem related to the imaginary part of the helicity amplitudes for forward Compton scattering, $\gamma_\lambda \mathrm{N}_H \to \gamma_{\lambda'} \mathrm{N}_{H'}$,

$$\mathcal{A}(\lambda, H; \lambda', H') = \epsilon^{\mu\star}_{\lambda'} \epsilon^{\nu}_{\lambda} T_{\mu\nu}(S), \tag{2.33}$$

where H and S denote the hadron's helicity and polarisation vector. The tensor $T_{\mu\nu}$

$$T^{\mu\nu} = i \int \mathrm{d}^4\xi e^{iq\xi} \langle PS | \mathcal{T} J^\mu(\xi) J^\nu(0) | PS \rangle, \tag{2.34}$$

involves the time-ordered product $\mathcal{T}$ of the hadronic electromagnetic currents and has the same structure as $W_{\mu\nu}$

$$W^{\mu\nu} = \frac{1}{\pi}\mathrm{Im}T^{\mu\nu}. \tag{2.35}$$

The number of independent helicity amplitudes corresponds to the number of structure function. The interference term σ_{TL} relates to a spin-flip amplitude, which is suppressed by a factor $\gamma \propto M/Q$.

It is usual to call the combination of F_1 and F_2 in Eq. 2.28 the longitudinal structure function, F_L, and to introduce the longitudinal-to-transverse cross-section ratio, R,

$$F_L = F_2(1+\gamma^2) - 2xF_1, \qquad R = \frac{\sigma_S}{\sigma_T} = \frac{F_L}{2xF_1} \tag{2.36}$$

and

$$F_1 = \frac{F_2(1+\gamma^2)}{2x(1+R)}. \tag{2.37}$$

2.4 Cross-section asymmetries

The observable spin-dependent effects in experiments are small and appear on top of the unpolarised cross section. They must be determined from differences of cross sections, which are vulnerable to small changes of the apparatus' acceptance. These systematic uncertainties largely cancel in the cross-section asymmetries

$$A_\parallel(x, Q^2; E) = \frac{\Delta_\parallel \sigma}{\overline{\sigma}} = \frac{\sigma^{\rightleftarrows} - \sigma^{\rightrightarrows}}{\sigma^{\rightleftarrows} + \sigma^{\rightrightarrows}}, \tag{2.38}$$

$$A_\perp(x, Q^2; E) = \frac{\Delta_\perp \sigma}{\overline{\sigma}} = \frac{\mathcal{H}_\ell}{\cos\varphi} \cdot \frac{\sigma(\varphi) - \sigma(\pi \pm \varphi)}{\sigma(\varphi) + \sigma(\pi \pm \varphi)}, \tag{2.39}$$

where $\rightarrow$ and $\Rightarrow$ indicate the beam and target polarisation, respectively and σ denotes the differential cross section (Eq. 2.20). To obtain $A_\parallel$ the longitudinal lepton or target polarisation must be inverted, while for $A_\perp$ the angle between the spin and scattering

planes, φ, must be changed to $\pi \pm \varphi$ (Fig. 2.2). This can be performed by either inverting the transverse target polarisation and compare events in the same part of the detector $(\pi + \varphi)$, or by comparing events in the upper and lower part of the detector for the same upward or downward-pointing target polarisation $(\pi - \varphi)$.

The parallel and perpendicular lepton asymmetries, $A_{\parallel}$ and $A_{\perp}$, do not have a straight forward physics interpretation and in addition they strongly depend on E or y. Hence, asymmetries obtained in experiments performed at different incident energies cannot be compared directly. Therefore it is customary to express the lepton asymmetries in terms of the virtual-photon asymmetries (Sect. 2.3),

$$A_1 = \frac{\sigma_T^{1/2} - \sigma_T^{3/2}}{2\sigma_T} \qquad \text{and} \qquad A_2 = \frac{\sigma_{TS}}{\sigma_T}, \tag{2.40}$$

which are functions of x and Q^2 only. They fulfil the following positivity constraints

$$0 \leq |A_1| \leq 1 \qquad \text{and} \qquad |A_2| \leq \sqrt{R}, \tag{2.41}$$

where the relation for A_2 [42] corresponds to $|\sigma_{TS}| \leq \sqrt{\sigma_S \sigma_T}$. Note that R and therefore A_2 is small at large Q^2 and not too small x.

From Eqs. 2.28–2.31 one finds for the the photon asymmetries in terms of the structure functions g_1 and g_2

$$\begin{pmatrix} A_1 \\ A_2 \end{pmatrix} = \frac{1}{F_1} \begin{pmatrix} 1 & -\gamma^2 \\ \gamma & \gamma \end{pmatrix} \begin{pmatrix} g_1 \\ g_2 \end{pmatrix}. \tag{2.42}$$

Several kinematic factors appear in the relation of the photon and lepton asymmetries. The depolarisation factor, D, describes the polarisation transfer from the incident lepton to the virtual photon and depends on the angle between their momenta. It also accounts for the contribution of scalar photons to the nominator in Eq. 2.38 and therefore it depends on the ratio $R = \sigma_S/\sigma_T$,

$$D = \frac{y(2-y)(1+\frac{\gamma^2 y}{2})}{(1+\gamma^2)y^2 + 2\left(1 - y - \frac{\gamma^2 y^2}{4}\right)(1+R)}. \tag{2.43}$$

The depolarisation factor, D, (better polarisation factor) vanishes for $y = 0$ and becomes unity for $y = 1$ assuming $R = 0$. Therefore events with high energy transfer, $\nu = yE$, are most sensitive to longitudinal spin effects, while the kinematic factor for transverse spin, d, has a maximum around $y = 0.8$ and vanishes for $y = 1$. With the kinematic factors[1] d, η, and ξ,

$$d = \frac{\sqrt{1 - y - \frac{y^2\gamma^2}{4}}}{1 - \frac{y}{2}} D, \qquad \eta = \gamma \frac{1 - y - \frac{\gamma^2 y^2}{4}}{(1 - \frac{y}{2})(1 + \frac{\gamma^2 y}{2})}, \qquad \xi = \gamma \frac{1 - \frac{y}{2}}{1 + \frac{\gamma^2 y}{2}}, \tag{2.44}$$

we obtain

$$\begin{pmatrix} A_{\parallel}/D \\ A_{\perp}/d \end{pmatrix} = \begin{pmatrix} 1 & \eta \\ -\xi & 1 \end{pmatrix} \begin{pmatrix} A_1 \\ A_2 \end{pmatrix}. \tag{2.45}$$

[1] The kinematic factors as function of ε (Eq. 2.25) are given in Appendix A of Ref. [31]

Combining the inverse of this equation and that of Eq. 2.42,

$$\begin{pmatrix} g_1 \\ g_2 \end{pmatrix} = \frac{F_1}{1+\gamma^2} \begin{pmatrix} 1 & \gamma \\ -1 & 1/\gamma \end{pmatrix} \begin{pmatrix} A_1 \\ A_2 \end{pmatrix}, \tag{2.46}$$

yields for the structure functions in terms of the lepton asymmetries

$$\begin{pmatrix} g_1 \\ g_2 \end{pmatrix} = \frac{F_1}{(1+\gamma^2)(1+\eta\xi)} \begin{pmatrix} 1+\gamma\xi & \gamma-\eta \\ -1+\xi/\gamma & \eta+1/\gamma \end{pmatrix} \begin{pmatrix} A_\parallel/D \\ A_\perp/d \end{pmatrix}. \tag{2.47}$$

Thus in general both, the parallel and the perpendicular asymmetry, are needed to determine the g_1 and/or g_2. However, until recently no measurements of $A_\perp$ were available. Therefore it is useful to express the structure functions in terms of the longitudinal lepton asymmetry, $A_\parallel$, and the photon asymmetry, A_2, which is bounded by $\sqrt{R}$ (Eq. 2.41),

$$\begin{pmatrix} g_1 \\ g_2 \end{pmatrix} = \frac{F_1}{1+\gamma^2} \begin{pmatrix} 1 & \gamma-\eta \\ -1 & \eta+1/\gamma \end{pmatrix} \begin{pmatrix} A_\parallel/D \\ A_2 \end{pmatrix}. \tag{2.48}$$

Note that the contribution of A_2 to g_1 is suppressed by the small kinematic factor $\gamma - \eta$. Neglecting A_2 we obtain

$$g_1 = \frac{F_1}{1+\gamma^2}\frac{A_\parallel}{D} = \frac{F_2}{2x(1+R)}\frac{A_\parallel}{D} \qquad \text{and} \qquad g_2 = -g_1. \tag{2.49}$$

Although in Eq. 2.49 the structure functions F_2 and R appear explicitly, it is important to note that only the spin-averaged cross section, i.e. F_1, is needed. Therefore the dependence of g_1 on R cancels when the spin-averaged cross sections were determined for the same kinematics and when the same values for R are used in both, the g_1 and the F_2 analysis.

2.5 Generalisation for deuteron targets

The representation of the cross sections by helicity amplitudes in Eqs. 2.28–2.31 can be generalised to hadrons with spin greater than $\frac{1}{2}$ [43, 44]. For spin-1 targets, like the deuteron, one finds four additional helicity amplitudes and thus four new structure functions [43], usual called b_1–b_4, of which b_3 and b_4 are like g_2 "higher-twist" contributions suppressed by M/Q and $b_2 = 2xb_1 + \mathcal{O}(M^2/Q^2)$, leaving b_1 as the only new twist-2 structure function. The scalar and transverse cross sections take the form

$$\sigma_S = \frac{1}{2}\left(\sigma_S^0 + \sigma_S^1\right), \quad \sigma_T = \frac{1}{3}\left(\sigma_T^0 + \sigma_T^1 + \sigma_T^2\right), \quad \sigma_{TS} = \frac{1}{2}\left(\sigma_{TS}^0 + \sigma_{TS}^1\right) \tag{2.50}$$

and an additional cross section, $\sigma_{TT}^0 \propto M^2/Q^2$, appears which corresponds to a double helicity-flip amplitude. For a spin-1 nucleus the contribution to b_1 from nucleons in an S-state vanishes in general [43], while for the deuteron a small contribution can arise from the D-state admixture in its wave function. The structure function b_1

$$\frac{b_1}{F_1} = \frac{1}{2}\frac{2\sigma_T^1 - \sigma_T^0 - \sigma_T^2}{\sigma_T} = \frac{3}{2}\frac{\sigma_T^1 - \sigma_T}{\sigma_T} \tag{2.51}$$

can be measured with an unpolarised beam as the cross-section difference for scattering from an unpolarised and a longitudinally a polarised target. With a polarised beam the

average cross section for a parallel and antiparallel polarised target must be taken, to cancel the contribution of g_1. In all analyses up to now $b_1^{\mathrm{d}} \equiv 0$ is assumed yielding for g_1

$$\frac{g_1}{F_1} = \frac{1}{2}\frac{\sigma_T^0 - \sigma_T^2}{\sigma_T} = \frac{3}{2}\frac{\sigma_T^0 - \sigma_T^2}{\sigma_T^0 + \sigma_T^1 + \sigma_T^2} \overset{b_1=0}{=} \frac{\sigma_T^0 - \sigma_T^2}{\sigma_T^0 + \sigma_T^2}. \tag{2.52}$$

Under this assumption it is sufficient to measure with parallel and antiparallel orientation of the target spins and to evaluate g_1 as in the proton case using Eqs. 2.38 and 2.49.

In Ref. [45] an additional double helicity-flip structure function, Δ, for targets with spin greater than $\frac{1}{2}$ is discussed. It is related to gluons not associated with individual nucleons in a nucleus and could be measured with a transversely polarised target and an unpolarised lepton beam. Both structure functions, b_1 [46] and Δ, are expected to be very small and their measurement is out of the scope of the SMC experiment. At measurement will be attempted in the HERMES experiment [28] at HERA.

2.6 Distance scales in deep-inelastic scattering

To investigate the distances relevant in deep-inelastic scattering [30, 38] we start from Eq. 2.15 (p. 6) for the hadronic tensor $W^{\mu\nu}$. The space-time region probed is determined by the distance ξ between the two points where the currents $J^\mu(\xi)$ and $J^\nu(0)$ act. In the Fourier integral the region, $\tilde{q}\xi \sim 1$, where the integrand does not oscillate rapidly, dominates. Here we use $\tilde{q}$ instead of q to avoid a confusion with the helicity distribution function, $q^+(x)$, used in the next section. In light-cone variables, which are defined by $a^\pm = (a^0 \pm a^3)/\sqrt{2}$ with the scalar product $a \cdot b = a^+b^- + a^-b^+ - \vec{a}_\perp \cdot \vec{b}_\perp$, the momentum transfer in the target rest fame becomes in the Bjorken limit

$$\begin{aligned} \tilde{q}^+ &= \frac{1}{\sqrt{2}}\left(\nu - \sqrt{\nu^2 + Q^2}\right) \to -\frac{1}{\sqrt{2}}Mx, \\ \tilde{q}^- &= \frac{1}{\sqrt{2}}\left(\nu + \sqrt{\nu^2 + Q^2}\right) \to \frac{1}{\sqrt{2}}\frac{Q^2}{Mx}. \end{aligned} \tag{2.53}$$

Thus, the limit, x fixed, $Q^2 \to \infty$, corresponds to $\tilde{q}^+$ fixed and $\tilde{q}^- \to \infty$. The condition, $\tilde{q}\xi \sim 1$, requires for the light-cone separations

$$|\xi^+| \leq \sqrt{2}Mx/Q^2 \qquad \text{and} \qquad |\xi^-| \leq \sqrt{2}/Mx. \tag{2.54}$$

Causality implies $\xi^2 = 2\xi^+\xi^- - \vec{\xi}_\perp^2 \geq 0$ and thus $\vec{\xi}_\perp^2 \sim 1/Q^2$. In the Bjorken limit deep-inelastic scattering is therefore dominated by the space-time region close to the light-cone, $\xi^2 = 0$, and the relevant longitudinal and transverse distance scales are

$$\xi^3 \sim \frac{1}{Mx} \qquad \text{and} \qquad \xi_\perp \sim \frac{1}{\sqrt{Q^2}}. \tag{2.55}$$

Note that already for $x \simeq 0.2$ the longitudinal scale is in the order of the nucleon's radius. The proper time, τ, available to the parton to interact with its companions is

$$\tau = \sqrt{(\xi^0)^2 - (\xi^3)^2} \sim \frac{1}{\sqrt{Q^2}}, \tag{2.56}$$

justifying the incoherence assumption of the quark parton model.

2.7 The quark parton model

The quark parton model [5, 47] allows us to understand structure functions in terms of quarks and in the QCD-improved form [7, 48] also of gluons. Deep-inelastic lepton scattering was one of the corner stones in establishing the partonic structure of hadrons [2] and thus in the development of QCD. Due to the asymptotic freedom of QCD at high momentum transfers, Q^2, in deep-inelastic scattering a hadron behaves like an incoherent superposition of free partons. If the hit parton, q, carries the fraction ξ of the hadron's 4-momentum, $p_q = \xi P$, the energy in the hadronic final state, W, is

$$W^2 = (q + p_q)^2 = q^2 + \xi^2 P^2 + 2\xi P \cdot q = Q^2 \left(\frac{\xi}{x} - 1\right) + \xi^2 M^2, \tag{2.57}$$

with the hadron mass, M, and $x = Q^2/2P \cdot q$. For a structureless parton only elastic scattering can occur requiring $W^2 = \xi^2 M^2$ or $\xi = x$. Thus the Bjorken variable, x, has a very intuitive interpretation as the fraction of hadron's momentum carried by the parton. The unphysical x dependence of the parton mass vanishes in the Breit–frame, where the hadron moves very fast towards a virtual photon with energy $\nu = 0$. In this frame all masses and transverse momenta can be neglected and x is the fraction of the hadron's longitudinal momentum carried by the struck parton.

For scattering from a free massless spin-$\frac{1}{2}$ parton inside a hadron, the hadronic tensor, $W^{\mu\nu}$, can easily be calculated and one finds the structure functions [34]

$$\hat{F}_1 = \frac{1}{2} e_P^2 \delta(\xi - x), \quad \hat{F}_2 = e_P^2 \xi \delta(\xi - x), \quad \hat{g}_1 = \lambda \frac{1}{2} e_P^2 \delta(\xi - x), \quad \hat{g}_2 = 0, \tag{2.58}$$

where e_P is the parton's charge. The factor $\lambda = \pm 1$ accounts for the fact that g_1 is defined using the hadron's spin orientation and therefore an additional minus sign is needed when the parton's spin is oriented opposite to the one of the hadron. From Eq. 2.58 it follows that g_2 does not have a simple interpretation in the quark parton model. The probability to find inside a hadron a parton of a certain type carrying a momentum fraction, ξ, is parametrised by the parton distribution functions, $q_i^\lambda(\xi)$. For the quarks we use $q_i = u, d, s, \ldots$ and for the gluon $q_i = g$. For a longitudinally polarised hadron, parallel and antiparallel orientation of the parton spin with respect to the hadron spin are denoted by $\lambda = \pm 1$. For a transversely polarised hadron, parallel and antiparallel orientation of the parton spin with respect to the hadron spin are denoted by $\lambda = (\uparrow, \downarrow)$. These functions are number densities normalised to the total number of partons of the considered type in the hadron. Usually the $q_i(x)$ are understood as the sum of the distribution functions of quarks and antiquarks in both helicity states. For clarity we therefore introduce $\widehat{q}$ for quarks and $\overline{q}$ for antiquarks and denote the difference of the helicity states by Δq,

$$q = \widehat{q} + \overline{q}, \qquad q = q^+ + q^-, \qquad \Delta q = q^+ - q^-, \qquad \Delta_T q = q^\uparrow - q^\downarrow. \tag{2.59}$$

The hadron structure functions are then given by

$$\mathcal{F}(x) = \sum_{i,\lambda} \int_0^1 q_i^\lambda(\xi) \hat{\mathcal{F}}_i^\lambda(x, \xi)\, \mathrm{d}\xi, \tag{2.60}$$

where i runs over all quark flavours and $\mathcal{F} = F_1$, F_2, g_1, and g_2, yielding

$$F_1(x) = \frac{1}{2} \sum_i e_i^2 \left\{ q_i^+(x) + q_i^-(x) \right\}, \tag{2.61}$$

$$F_2(x) = x \sum_i e_i^2 \left\{ q_i^+(x) + q_i^-(x) \right\}, \tag{2.62}$$

$$g_1(x) = \frac{1}{2} \sum_i e_i^2 \left\{ q_i^+(x) - q_i^-(x) \right\}, \tag{2.63}$$

$$h_1(x) = \frac{1}{2} \sum_i e_i^2 \left\{ q_i^\uparrow(x) - q_i^\downarrow(x) \right\}, \tag{2.64}$$

$$g_2(x) = 0, \tag{2.65}$$

with the quark charges, e_i, in units of e. An important result is the scaling of the structure functions first pointed out by Bjorken [3]. In the limit $Q^2 \to \infty$, where the quark parton model is applicable, the structure functions do not depend on ν and Q^2 separately, but become functions of x only. In QCD gluon radiation causes a logarithmic Q^2 dependence known as scaling violations, which is discussed in Sect. 2.9. Another consequence of the quark parton model is the Callan–Gross relation [49]

$$F_2(x) = 2xF_1(x), \qquad \text{i.e.} \qquad F_L \equiv 0, \qquad R \equiv 0, \tag{2.66}$$

expressing the fact that massless spin-$\frac{1}{2}$ particles cannot absorb scalar photons. This relation receives corrections in order α_s in QCD.

Other combinations of the quark distribution functions appear in the structure functions for weak interactions. In particular charged-current neutrino scattering has contributed much of what we know about the parton distribution functions. From the cross sections for neutrino and antineutrino-nucleon scattering one obtains the parity-violating structure functions,

$$F_3^{\mathrm{W}^-}(x) = 2\{\widehat{u}(x) + \widehat{c}(x) - \overline{d}(x) - \overline{s}(x)\}, \tag{2.67}$$

$$F_3^{\mathrm{W}^+}(x) = 2\{\widehat{d}(x) + \widehat{s}(x) - \overline{u}(x) - \overline{c}(x)\}. \tag{2.68}$$

Their average measures the valence-quark distribution functions, $q_{\mathrm{v}} = \widehat{q} - \overline{q}$. If the proton beam at HERA can be polarised, one might have access to similar structure functions in the polarised case [31, 50] at large Q^2,

$$\begin{aligned} g_5^{\mathrm{W}^-}(x) &= \Delta\widehat{u}(x) + \Delta\widehat{c}(x) - \Delta\overline{d}(x) - \Delta\overline{s}(x), \\ g_5^{\mathrm{W}^+}(x) &= \Delta\widehat{d}(x) + \Delta\widehat{s}(x) - \Delta\overline{u}(x) - \Delta\overline{c}(x), \end{aligned} \tag{2.69}$$

and also

$$\begin{aligned} g_1^{\mathrm{W}^-}(x) &= \Delta\widehat{u}(x) + \Delta\widehat{c}(x) + \Delta\overline{d}(x) + \Delta\overline{s}(x), \\ g_1^{\mathrm{W}^+}(x) &= \Delta\widehat{d}(x) + \Delta\widehat{s}(x) + \Delta\overline{u}(x) + \Delta\overline{c}(x). \end{aligned} \tag{2.70}$$

At present only semi-inclusive scattering can provide insight into other combinations of polarised parton distribution functions through the additional weight introduced by the fragmentation functions, see Sect. 5.7.

Parton distribution functions are universal in the sense that a distribution function determined in one process can be used to calculate other processes. Thus, the parton distribution functions determined in deep-inelastic scattering are the basis for the prediction of hadron-hadron cross sections at e.g. LHC.

2.8 Sum rules in the quark parton model

The Ellis-Jaffe [16] and Bjorken sum rules [14] for the first moment of g_1,

$$\Gamma_1 = \int_0^1 g_1(x)\,\mathrm{d}x \tag{2.71}$$

follow — in the quark parton model — immeadiately from Eq. 2.63. We introduce the somewhat unprecise but widely used notation

$$\Delta q = \int_0^1 \Delta q(x)\,\mathrm{d}x, \tag{2.72}$$

for the spin carried by the quarks and antiquarks of a certain flavour in units of $\hbar/2$. For the proton we then can write

$$\Gamma_1^{\mathrm{p}} = \frac{1}{2}\left\{\frac{4}{9}\Delta u + \frac{1}{9}\Delta d + \frac{1}{9}\Delta s\right\} \tag{2.73}$$

$$= \frac{1}{12}\underbrace{(\Delta u - \Delta d)}_{a_3} + \frac{1}{36}\underbrace{(\Delta u + \Delta d - 2\Delta s)}_{\sqrt{3}a_8} + \frac{1}{9}\underbrace{(\Delta u + \Delta d + \Delta s)}_{a_0}. \tag{2.74}$$

Using isospin symmetry the same formula holds for the neutron with $u \leftrightarrow d$, i.e. $a_3 \leftrightarrow -a_3$, exchanged

$$\Gamma_1^{\mathrm{p,n}} = \frac{1}{12}\left(\pm a_3 + \frac{1}{\sqrt{3}}a_8\right) + \frac{1}{9}a_0. \tag{2.75}$$

The difference, Δq, of right and left-handed quarks in a proton with momentum P and spin S is obtained with the projection operators $(1 \pm \gamma_5)/2$ as

$$2MS_\mu \Delta q = \langle P,S|\bar{q}\gamma_\mu\gamma_5 q|P,S\rangle, \tag{2.76}$$

where S^μ is the covariant spin vector (Eq. 2.13). The proton matrix elements, a_0 and a_i, are then given by

$$\langle P,S|J^i_{5\mu}|P,S\rangle = MS_\mu a_i \qquad (i = 1,2,\ldots,8) \tag{2.77}$$

$$\langle P,S|J^0_{5\mu}|P,S\rangle = 2MS_\mu a_0, \tag{2.78}$$

with the flavour-singlet axial-vector current

$$J^0_{5\mu} = \overline{\psi}\gamma_\mu\gamma_5\psi \qquad \text{with} \quad \psi = \begin{pmatrix} \psi_u \\ \psi_d \\ \psi_s \end{pmatrix}, \tag{2.79}$$

and the octet of axial-vector currents

$$J^i_{5\mu} = \overline{\psi}\gamma_\mu\gamma_5\frac{\lambda_i}{2}\psi, \quad \text{with} \qquad (i = 1,2,\ldots,8). \tag{2.80}$$

The matrices λ_i are the generators of flavour SU(3) in the Gell–Mann standard representation. The nonsinglet axial-vector currents also describe together with the vector currents, J^i_μ, the weak decays of the hyperons in the spin-$\frac{1}{2}$ baryon octet consisting of n, p, $\Sigma^\pm$, Σ^0, Λ, Ξ^-, and the Ξ^0. Assuming SU(3) flavour symmetry, all matrix elements of the

axial currents in this octet are given by two coupling constants, F and D, which were determined experimentally, for details see [31] and references therein.

For a_3 and a_8 one obtains

$$a_3 = F + D = g_a, \qquad \sqrt{3}a_8 = 3F - D. \tag{2.81}$$

No decay is related to the singlet matrix element a_0. The matrix element a_3 is given by the neutron decay constant, $g_a = |G_A/G_V| = 1.2573 \pm 0.0028$ [51]. Only isospin symmetry has to be assumed for the relation $a_3 = g_a$. From Eq. 2.75 we thus find the Bjorken sum rule [14]

$$\Gamma_1^{\mathrm{p}} - \Gamma_1^{\mathrm{n}} = \frac{1}{6} g_a \qquad \text{(Bjorken sum rule)}. \tag{2.82}$$

To obtain separate sum rules for the proton and the neutron a value for a_0 is needed, which cannot be fixed from hyperon decay data. Ellis and Jaffe [16] assumed that the strange quarks are not polarised, $\Delta s \equiv 0$, leading to $a_0 = \sqrt{3}a_8$ and thus

$$\Gamma_1^{\mathrm{p,n}} = \frac{1}{12} g_a \left\{ \pm 1 + \frac{5}{3} \frac{3F/D - 1}{F/D + 1} \right\} \qquad \text{(Ellis–Jaffe sum rules)}. \tag{2.83}$$

The QCD corrections to these sum rules are discussed in Sect. 2.11.

In the quark parton model the total contributions of the quarks to the nucleon's spin is given by

$$\Delta\Sigma = \Delta u + \Delta d + \Delta s = a_0. \tag{2.84}$$

Naïvely one expects $\Delta\Sigma = 1$. The value obtained from $\sqrt{3}a_8$ is $\Delta\Sigma = 0.579 \pm 0.026$ [52]. A reduction from unity is expected from relativistic effects and in line with the fraction of the longitudinal momentum of the nucleon carried by the quarks of about 0.5. The value of $\Delta\Sigma = 0.12 \pm 0.16$ found in the EMC experiment [17] came as a big surprise.

2.9 Scaling violations

In QCD partons can radiate other partons, leading to a cloud of gluons and a sea of quark-antiquark pairs surrounding each quark. The shortest distance, which can be resolved by a photon with 4-momentum q, is proportional to $1/\sqrt{Q^2}$ with $Q^2 = -q^2$. Hence, with increasing Q^2 the one finds more and more partons in the nucleon. This implies that the average momentum fraction carried by each parton decreases with increasing Q^2 leading to a depletion of the spin-averaged parton distribution functions at large x and a corresponding enhancement at small x. The situation for the spin-dependent distribution functions is not as straight forward.

The probability to radiate from a parton i with momentum p a parton j with momentum zp is described by the so-called splitting function, $P_{ij}(z)$, where i and j stand for quarks or gluons, $i, j = q, g$. The splitting functions can be calculated using Feynman's rules. In the process $\gamma^\star q \to qg$ the integration over the gluon phase space results in a logarithmic Q^2 dependence of the cross section. This Q^2 dependence can be absorbed into the definition of the parton distribution functions, $q(x, Q^2)$ and $g(x, Q^2)$, leading to the famous Altarelli–Parisi equations [7, 48, 53, 54].

Apart from the splitting functions the equations for the spin-averaged and spin-dependent case are identical. The flavour-singlet combination, i.e. the sum of all quark distribution

functions,

$$\Delta\Sigma(x,Q^2) = \sum_{i=1}^{n_f} \Delta q(x,Q^2) \tag{2.85}$$

evolves together with the gluon distribution function, $\Delta g(x,Q^2)$. Flavour-nonsinglet combinations, i.e. differences of quark distribution functions, evolve independently from the gluons. Following Ref. [55] we use

$$\Delta q^{\mathrm{ns}}(x,Q^2) = \sum_{i=1}^{n_f} \left(\frac{e_i^2}{\langle e^2 \rangle} - 1 \right) \Delta q_i(x,Q^2) \tag{2.86}$$

with $\langle e^2 \rangle = \sum e_i^2/n_f$. In the Q^2 range for the present experiments only up, down, and strange quarks contribute significantly and the number of active flavours, n_f, is three. With these definitions and the notation,

$$(a \otimes b)(x) := \int_x^1 \frac{\mathrm{d}y}{y} a\left(\frac{x}{y}\right) b(y), \tag{2.87}$$

the Altarelli–Parisi equations read for the spin-dependent case [7]

$$\frac{\mathrm{d}}{\mathrm{d}\ln Q^2} \Delta q^{\mathrm{ns}} = \frac{\alpha_s}{2\pi} \Delta P_{qq}^{\mathrm{ns}} \otimes \Delta q^{\mathrm{ns}} \tag{2.88}$$

$$\frac{\mathrm{d}}{\mathrm{d}\ln Q^2} \begin{pmatrix} \Delta\Sigma \\ \Delta g \end{pmatrix} = \frac{\alpha_s}{2\pi} \begin{pmatrix} \Delta P_{qq}^{\mathrm{s}} & 2n_f \Delta P_{qg}^{\mathrm{s}} \\ \Delta P_{gq}^{\mathrm{s}} & \Delta P_{gg}^{\mathrm{s}} \end{pmatrix} \otimes \begin{pmatrix} \Delta\Sigma \\ \Delta g \end{pmatrix}, \tag{2.89}$$

with the obvious notation $\Delta P_{ab} = P_{a^+b^+} - P_{a^+b^-}$. The structure function g_1 is given by a convolution of the singlet and nonsinglet coefficient functions, C_{s} and C_{ns}, and C_g with the parton distribution functions

$$g_1 = \frac{1}{2}\langle e^2 \rangle \left\{ C_{\mathrm{ns}} \otimes \Delta q^{\mathrm{ns}} + C_{\mathrm{s}} \otimes \Delta\Sigma + 2n_f C_g \otimes \Delta g \right\}. \tag{2.90}$$

The coefficient functions are discussed in Sect. 2.10. The splitting and coefficient functions, P and C, depend on x and α_s and can be expanded in a power series in α_s

$$C(x,\alpha_s) = C^{(0)}(x) + \frac{\alpha_s}{2\pi} C^{(1)} + \mathcal{O}(\alpha_s^2) \tag{2.91}$$

$$P(x,\alpha_s) = P^{(0)}(x) + \frac{\alpha_s}{2\pi} P^{(1)} + \mathcal{O}(\alpha_s^2). \tag{2.92}$$

With the leading-order coefficient functions $C_{\mathrm{s}}^{(0)} = C_{\mathrm{ns}}^{(0)} = \delta(1-x)$ and $C_g^{(0)} = 0$ the parton model formula Eq. 2.63 is recovered. The next-to-leading order coefficient functions were calculated by Kodaira *et al.* [56] in 1979. However, full next-to-leading order calculations became only possible after the determination of the two-loop splitting functions, $P^{(1)}$, by Mertig and van Neerven [57] and by Vogelsang [58] in 1995. In next-to-leading order the separation between $\Delta\Sigma$ and Δg becomes factorisation scheme dependent and thus in principle ambiguous.

Similarities and differences of the spin-dependent and spin-averaged splitting functions are discussed e.g. in Refs. [59, 60]. Due to helicity conservation for massless quarks at the quark-gluon vertex the polarised and unpolarised leading-order splitting functions, ΔP_{qq}

and P_{qq}, are identical. The spin of the emitted gluon must be compensated by orbital angular momentum. Therefore, one expects a similar Q^2 dependence of the structure functions g_1 and F_1 in the large-x region, where the nonsinglet valence-quark content dominates. The unpolarised structure function, F_1, grows at small x due to soft gluon emission, which causes singularities in the singlet splitting functions, P_{gq} and P_{gg}. In the polarised case however, the process $g \to q\bar{q}$ leads to a quark pair with opposite helicity of the quark and the antiquark due to helicity conservation at the vertex. Thus, no increase in g_1 can be expected from this process.

2.10 The operator-product expansion

The theoretical basis of the quark parton model in QCD is Wilson's operator-product expansion [61]. For short distances, ξ, the product of two local operators can be expanded into a sum of nonsingular local operators multiplied by singular complex coefficient functions, $C(\xi^2)$. They are functions of the space-time separation of the points where the two operators act. The operator-product expansion cannot be applied directly to the product of the hadronic electromagnetic currents $J^\mu(\xi)J^\nu(0)$ in Eq. 2.15 (p. 6), because as discussed in Sect. 2.6 the Bjorken limit is not a short distance limit, in which all components of q become large. However, the operator-product expansion is applicable to forward Compton scattering of a virtual photon in Eq. 2.34 (p. 9) and can be carried over to the hadronic tensor $W^{\mu\nu}$ and hence the structure functions using the optical theorem and dispersion relations. It is important to realise, that Eq. 2.15 and thus the relation to the forward Compton amplitude, Eq. 2.35, is only valid for truly inclusive scattering. The observation of a particular final state invalidates the completeness relation, used in the derivation of Eq. 2.15.

The application of the operator-product expansion to deep-inelastic scattering is sketched in this section following the discussion by Kodaira [62]. More details can also be found there and e.g. in Refs. [30, 34, 38]. We start from Eq. 2.34, which dropping the Lorentz indices for simplicity, takes the form

$$T(x, Q^2) = i \int \mathrm{d}^4\xi e^{iq\xi} \langle P|\mathcal{T} J(\xi)J(0)|P\rangle. \tag{2.93}$$

The operator-product expansion of the time-ordered product of the two currents yields

$$\mathcal{T} J(\xi)J(0) \sim \sum_{i,n} C_i^n(\xi^2)\xi^{\mu_1} \cdots \xi^{\mu_n} \mathcal{O}^i_{\mu_1\cdots\mu_n}(0), \tag{2.94}$$

where the operators are labelled by their spin, n. The superscript, i, distinguishes different operators with the same spin. To see the relative importance of the terms, we study their mass dimensions. The coordinate ξ has mass dimension -1 yielding dimension $-n$ for the factors ξ^{μ_i}. Taking into account the mass dimensions of the currents on the left-hand side, $d_J = 3$, and that of the operator itself, d_n^i, the mass dimension of the coefficient function is given by

$$C_i^n(\xi^2) \sim \left(\xi^2\right)^{(d_n^i - n - 2d_J)/2}. \tag{2.95}$$

Thus the dominant effects for $\xi^2 \to 0$ are ordered by the *twist*,

$$t = d - n, \tag{2.96}$$

of the related operators, i.e. the difference of their mass dimension and spin. The lowest twist operators in QCD have twist two, involving e.g. two quark fields with spin 1/2 and mass dimension 3/2.

The matrix elements of the operators $\mathcal{O}^i_{\mu_1\cdots\mu_n}$ needed when inserting Eq. 2.94 into Eq. 2.93 can be written in the form

$$\langle P|\mathcal{O}^i_{\mu_1\cdots\mu_n}(0)|P\rangle = 2a^i_n P_{\mu_1}\cdots P_{\mu_n}. \tag{2.97}$$

With this definition of the reduced matrix elements, a^i_n, and the Fourier transform of Eq. 2.94

$$i\int \mathrm{d}^4\xi e^{iq\xi}\mathcal{T}J(\xi)J(0) \sim \sum_{i,n} C^n_i(Q^2)\left(\frac{2}{Q^2}\right)^n q^{\mu_1}\cdots q^{\mu_n}\mathcal{O}^i_{\mu_1\cdots\mu_n}(0) \tag{2.98}$$

one obtains

$$T(x,Q^2) = 2\sum_{i,n}\left(\frac{1}{x}\right)^n a^i_n C^n_i(Q^2), \tag{2.99}$$

with $x = Q^2/2Pq$. Using contour integration of T in the complex $1/x$ plane and $W = \frac{1}{\pi}\mathrm{Im}T$ (Eq. 2.35) one obtains for the nth moment of W

$$M^n(Q^2) = \int_0^1 \mathrm{d}x\, x^{n-1}W(x,Q^2) = \sum_i a^i_n C^n_i(Q^2). \tag{2.100}$$

Thus, the nth moment of a structure function is given by operators with spin n only. The important point is that the moments factorise in a calculable perturbative part, the coefficient functions, and a non-perturbative part containing the hadron structure, the a^i_n.

The coefficient functions $C^n_i\left(Q^2/\mu^2, \alpha_s(\mu^2)\right)$ depend on the renormalisation scheme and on the renormalisation point μ^2. Also the operators, and thus the matrix elements a^i_n can depend on μ^2. Physical quantities like the moments of structure functions must be independent of the renormalisation point. This requirement leads to the renormalisation group equations, which couple the μ^2 dependence of the fundamental fields and of the strong coupling constant, $\alpha_s(\mu^2)$. The variation of the coupling constant with μ^2 is described by the beta-function of QCD

$$\beta(a_s) = \mu^2\frac{\partial a_s}{\partial\mu^2} = -\beta_0 a_s^2 - \beta_1 a_s^3 - \cdots \qquad \text{with} \quad a_s = \frac{\alpha_s}{4\pi}, \tag{2.101}$$

where $\beta_0 = 11 - \frac{2}{3}n_f$, $\beta_1 = 102 - \frac{38}{3}n_f$, and n_f is the number of active quark flavours. Following Ref. [63] we use $a_s = \alpha_s/4\pi$. The μ^2 dependence of the renormalised operator is given by its so-called anomalous dimension $\gamma^n_{\mathcal{O}}$

$$\gamma^n_{\mathcal{O}} = \mu^2\frac{\mathrm{d}}{\mathrm{d}\mu^2}\log Z^n_{\mathcal{O}} = \gamma^{(0)}a_s + \gamma^{(1)}a_s^2\cdots, \tag{2.102}$$

where $Z^n_{\mathcal{O}}$ is the renormalisation constant and $\mathcal{O}^0_n$ is the bare operator

$$\mathcal{O}_n(\mu^2) = \mathcal{O}^0_n/Z^n_{\mathcal{O}}(\mu^2). \tag{2.103}$$

Operators corresponding to physical quantities have vanishing anomalous dimension, i.e. are independent of the renormalisation point μ^2. Both, the beta function and the anomalous dimension can be expanded in power series in a_s and the coefficients can be calculated

in perturbative QCD. The renormalisation group equations for the coefficient functions read

$$\mu^2 \frac{\mathrm{d}}{\mathrm{d}\mu^2} M^n(Q^2) \equiv 0 \quad \Rightarrow \quad \left(\mu^2 \frac{\partial}{\partial \mu^2} + \beta(a_s) \frac{\partial}{\partial a_s} - \gamma_{\mathcal{O}}^n \right) C^n = 0 \tag{2.104}$$

with the solution

$$C^n \left(\frac{Q^2}{\mu^2}, a_s(Q^2) \right) = C^n(1, a_s(Q^2)) \exp \left\{ \int_{a_s(\mu^2)}^{a_s(Q^2)} \frac{\gamma_{\mathcal{O}}^n(a_s')}{\beta(a_s')} \, \mathrm{d}a_s' \right\}. \tag{2.105}$$

By construction the moments, M^n, are now independent of μ^2. However, for operators with non-vanishing anomalous dimension the matrix elements, a_n^i, depend on μ^2. This applies in particular to the matrix element, $\Delta\Sigma(\mu^2)$, of the flavour-singlet axial-vector current, $J_{5\mu}^0$, which we discuss here as an example. The natural scale in deep-inelastic scattering is $\mu^2 = Q^2$. For this choice the renormalisation group exponent in Eq. 2.105 is unity and the μ^2 dependence turns into a Q^2 dependence, $\Delta\Sigma(Q^2)$. It is also possible to split the exponent into a μ^2 and a Q^2-dependent part and to define the μ^2-independent quantity [63]

$$\Delta\Sigma_{\mathrm{inv}} = \exp \left\{ -\int^{a_s(\mu^2)} \frac{\gamma^{\mathrm{s}}(a_s')}{\beta(a_s')} \, \mathrm{d}a_s' \right\} \Delta\Sigma(\mu^2). \tag{2.106}$$

In this case the Q^2 dependent part of the exponent

$$1 - a_s(Q^2) \frac{\gamma^{(1)}}{\beta_0} + \mathcal{O}(a_s^2) \tag{2.107}$$

must be accounted for in $C(Q^2/\mu^2, a_s)$. The Q^2 dependence of $\Delta\Sigma$ appears beyond leading order and is due to the axial anomaly.

2.11 Sum rules for the moments of g_1 and g_2

When the Lorentz structure of the currents is kept and the operator mixing in renormalisation is taken into account, the operator product expansion yields for the moment sum rules of g_1 and g_2 [64]

$$\int_0^1 x^{n-1} g_1(x, Q^2) \, \mathrm{d}x = \frac{1}{2} \sum_i \varepsilon_i a_n^i C_{1,i}^n(Q^2), \qquad n = 1, 3, \ldots \tag{2.108}$$

$$\int_0^1 x^{n-1} g_2(x, Q^2) \, \mathrm{d}x = \frac{1-n}{2n} \sum_i \varepsilon_i \left[a_n^i C_{1,i}^n(Q^2) - d_n^i C_{2,i}^n(Q^2) \right], \quad n = 3, 5, \ldots \tag{2.109}$$

where $i = 1, \ldots, 8, \psi, g$ runs over the flavour nonsinglet operators ($i = 1 \ldots 8$) and the quark flavour-singlet and gluon operators ($i = \psi, g$). Following the notation of Ref. [31] the constants ε_i account for the charge and the isospin structure of the involved currents. For the proton they are given by

$$\varepsilon_3 = \frac{1}{3}, \qquad \varepsilon_8 = \frac{1}{3\sqrt{3}}, \qquad \varepsilon_\psi = \varepsilon_g = \frac{2}{9}, \qquad \varepsilon_i = 0 \ \text{ for } \ i \neq 3, 8, \psi, g. \tag{2.110}$$

The coefficient functions, $C_{1,i}^n$, and the matrix elements, a_n^i, refer to twist-2 operators, while $C_{2,i}^n$ and d_n^i correspond to twist-3 operators.

Table 2.1: Higher-order coefficients of the flavour-singlet and nonsinglet coefficient functions, $C^{\rm ns}$ and $C^{\rm s}$, in the $\overline{\rm MS}$ scheme. The coefficients $c_4^{\rm ns}$ and $c_3^{\rm s}$ are estimates; $c_3^{\rm s}$ is unknown for $n_f = 4$ flavours.

n_f	nonsinglet				singlet ($\Delta\Sigma_{\rm inv}$)			singlet ($\Delta\Sigma(Q^2)$)		
	$c_1^{\rm ns}$	$c_2^{\rm ns}$	$c_3^{\rm ns}$	$c_4^{\rm ns}$	$c_1^{\rm s}$	$c_2^{\rm s}$	$c_3^{\rm s}$	$c_1^{\rm s}$	$c_2^{\rm s}$	$c_3^{\rm s}$
3	1	3.5833	20.2153	130	0.3333	0.5496	2	1	1.0959	3.7
4	1	3.2500	13.8503	68	0.0400	−1.0815	—	1	−0.0666	—

The Ellis–Jaffe and Bjorken sum rules follow immeadiately from Eq. 2.108 for $n = 1$. No gluon operator exist for spin $n = 1$ and hence there is no direct gluon contribution, a_1^g, to the first moment of g_1. The remaining matrix elements, a_n^i, are those of the singlet and nonsinglet axial vector currents, a_0, a_3, and a_8. The definitions of the a_n^i differ slightly from those of in Eqs. 2.77 leading to the following identities

$$2a_1^3 = a_3 = g_a, \qquad 2a_1^8 = a_8 = \frac{1}{\sqrt{3}}(3F - D), \qquad a_1^\psi = a_0 = \Delta\Sigma. \tag{2.111}$$

With these relations we obtain the QCD-corrected Ellis–Jaffe sum rules

$$\Gamma_1^{\rm p,n}(Q^2) = \frac{1}{12}\left\{\pm g_a + \frac{1}{3}(3F - D)\right\} C^{\rm ns}(Q^2) + \frac{1}{9}\Delta\Sigma\, C^{\rm s}(Q^2) \tag{2.112}$$

and the Bjorken sum rule

$$\Gamma_1^{\rm p}(Q^2) - \Gamma_1^{\rm n}(Q^2) = \frac{1}{6} g_a C^{\rm ns}(Q^2). \tag{2.113}$$

The singlet and nonsinglet coefficient functions, $C^{\rm s}$ and $C^{\rm ns}$, can be expanded into a power series in α_s/π

$$C(\alpha_s) = 1 - c_1\left(\frac{\alpha_s}{\pi}\right) - c_2\left(\frac{\alpha_s}{\pi}\right)^2 - c_3\left(\frac{\alpha_s}{\pi}\right)^3 - \cdots \tag{2.114}$$

The coefficients, $c_1^{\rm s,ns}$ were calculated in the $\overline{\rm MS}$ scheme in the original work by Kodaira *et al.* [56, 64] back in 1979/80. Recently, also the coefficients up to $c_3^{\rm ns}$ [65] for the nonsinglet and up to $c_2^{\rm s}$ [63] for the singlet coefficient function were calculated. The results are summarised for the case of three and four active quark flavours in Table 2.1 together with estimates of the constants $c_4^{\rm ns}$ and $c_3^{\rm s}$ [66]. The two sets given for the singlet coefficients correspond to the two possible choices, $\Delta\Sigma_{\rm inv}$ and $\Delta\Sigma(Q^2)$, discussed at the end of Sect. 2.10 (Eq. 2.106, p. 20). The nonsinglet currents are conserved and thus the matrix elements a_3 and a_8 are Q^2 independent.

We now turn to the second spin dependent structure function, g_2. For $n = 1$ one obtains from Eq. 2.109 the Burkhardt–Cottingham sum rule, first derived in 1975 using dispersion relations and Regge theory [67]

$$\int_0^1 g_2(x, Q^2)\,{\rm d}x = 0. \tag{2.115}$$

However, none of the operators corresponding to $n = 1$ in Eq. 2.109 exists and therefore this sum rule does not follow from the operator product expansion [40]. There has been

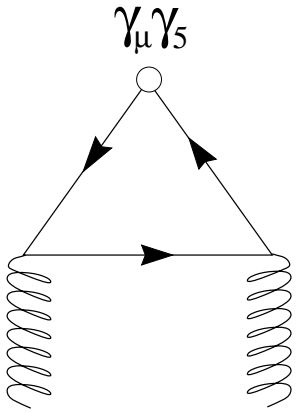

Figure 2.3: Triangle graph causing the anomalous gluon contribution to the singlet axial vector current.

some controversy in the literature about the validity of the Burkhardt–Cottingham sum rule [31, 40, 68–70] and an experimental determination of the integral would be of high interest.

A relation between the structure functions g_1 and g_2 can be obtained by considering the sum of Eqs. 2.108 and 2.109,

$$\int_0^1 x^{n-1} \left\{ g_1(x,Q^2) + g_2(x,Q^2) \right\} \mathrm{d}x = \sum_i \varepsilon_i \left\{ \frac{1}{2} a_n^i C_{1,i}^n(Q^2) + \frac{n-1}{2n} d_n^i C_{2,i}^n(Q^2) \right\}. \tag{2.116}$$

If this relation is assumed to be valid also for $n = 1$, i.e. assuming the validity of the Burkhardt–Cottingham sum rule, it can by an inverse Mellin transformation be cast in the form

$$g_2(x,Q^2) = g_2^{\mathrm{ww}}(x,Q^2) + \bar{g}_2(x,Q^2) \tag{2.117}$$

with the twist-2 part

$$g_2^{\mathrm{ww}}(x,Q^2) = -g_1(x,Q^2) + \int_x^1 \frac{g_1(y,Q^2)}{y} \mathrm{d}y. \tag{2.118}$$

The twist-2 part, g_2^{ww}, was first derived by Wandzura and Wilczek [71] in 1977 assuming $\bar{g}_2(x,Q^2)$ to vanish. The pure twist-3 part, $\bar{g}_2(x,Q^2)$, describes quark-gluon correlations and arises from the d_n^i in Eq. 2.116 while the a_n^i correspond to g_2^{ww}. In addition to the contributions given here, g_2 also receives a twist-2 contribution from transverse quark polarisation [72, 73], which in deep-inelastic scattering is suppressed by the quark-to-gluon mass ratio.

2.12 The axial anomaly

In contrast to the conserved vector currents the axial currents are expected to be conserved only in the limit of massless quarks,

$$\partial_\mu \bar{\psi}_f \gamma^\mu \gamma_5 \psi_f = 2mi\bar{\psi}_f \gamma_5 \psi_f \overset{m\to 0}{\to} 0. \tag{2.119}$$

However, this relation breaks down in quantum theory due to an additional anomalous gluon contribution [74–76] owing to the triangle graph shown in Fig. 2.3. Originally this was found by Adler and by Bell and Jackiw [77] in the context of QED, where an analogous graph is responsible for the decay $\pi^0 \to 2\gamma$. The anomalous gluon contribution affects only the singlet axial current, while it cancels between flavours in the conserved nonsinglet currents. Anomalies are e.g. discussed in Refs. [78, 79] and for a review in the context of polarised scattering see Ref. [31]. Also for massless quarks one finds a non-vanishing divergence

$$\partial_\mu \bar{\psi}\gamma^\mu\gamma_5\psi = \frac{\alpha}{2\pi} n_f \mathrm{Tr}\left(G_{\mu\nu}\widetilde{G}^{\mu\nu}\right), \tag{2.120}$$

where $G_{\mu\nu}$ is the gluon field tensor and $n_f = 3$ the number of active (light) flavours. The actual result for the anomalous contribution depends on the quark-to-gluon mass ratio [31]. In obtaining the result of Eq. 2.120 it was assumed that the mass of bound, slightly off-shell gluons is large compared to the up, down, and strange quark masses and small compared to the charm, bottom, and top quark masses. It is widely believed [31] that higher order graphs do not contribute to the anomaly [80]. Then a conserved current can be constructed by subtracting an axial gluon current, K_μ, from the quark current

$$\widetilde{J}^0_{5\mu} = J^0_{5\mu} - n_f \frac{\alpha_s}{2\pi} K_\mu, \qquad \text{with} \quad \partial_\mu K^\mu = \mathrm{Tr}\left(G_{\mu\nu}\widetilde{G}^{\mu\nu}\right). \tag{2.121}$$

The modified current, $\widetilde{J}^0_{5\mu}$, is independent of the renormalisation point, μ^2, and the corresponding matrix element (Eq. 2.78, p. 15) is thus independent of Q^2,

$$\widetilde{a}_0 = a_0 + n_f \frac{\alpha_s}{2\pi} \Delta g. \tag{2.122}$$

It is attractive to re-interpret now $\widetilde{a}_0$ as the fraction of the nucleon's spin carried by quarks and to 'explain' the small value found in experiments for $\Delta\Sigma$ by a large negative gluon contribution

$$\Delta\Sigma = \widetilde{\Delta\Sigma} - n_f \frac{\alpha_s}{2\pi} \Delta g. \tag{2.123}$$

However, the axial gluon current, K_μ, is not gauge invariant and corresponds to the gluon polarisation only in a certain gauge. Therefore this interpretation is not commonly accepted and has been criticised [81]. In this paper we use $\Delta\Sigma$ and a_0 as synonyms and always denote the quantities 'corrected' for the anomalous gluon contribution by a tilde. Normally one would expect the term, $\alpha_s \Delta g$, to vanish in the limit $Q^2 \to \infty$. However, to first order perturbation theory the product, $\alpha_s(Q^2)\Delta g(Q^2)$, is Q^2 independent implying that Δg grows like α_s^{-1}. This can be seen from the leading-order evolution equations for the first moments,

$$\frac{\mathrm{d}}{\mathrm{d}\ln Q^2}\begin{pmatrix} \Delta\Sigma \\ \Delta g \end{pmatrix} = \frac{\alpha_s}{2\pi}\begin{pmatrix} 0 & 0 \\ 2 & \frac{1}{2}\beta_0 \end{pmatrix}\begin{pmatrix} \Delta\Sigma \\ \Delta g \end{pmatrix}, \tag{2.124}$$

together with the renormalisation group equation 2.101 (p. 19) Therefore, in this case the usually small ambiguity in the separation of singlet quark and gluon contributions becomes large.

Chapter 3

The SMC experiment

In the NA47 experiment we measure the cross-section asymmetries for scattering of polarised muons from polarised proton and deuteron targets. The main elements of experimental setup are the polarised muon beam, the polarised target, and the scattered muon forward spectrometer. Magnetic spectrometers and tracking devices upstream and downstream of the polarised target determine the momenta of the incoming and scattered muon and the scattering angle. At the end of the apparatus the scattered muon is identified by its ability to penetrate a hadron absorber. Downstream of the scattering experiment the polarisation of the muon beam is measured in a dedicated apparatus. The polarisation of the muon beam cannot be inverted efficiently unlike that of an electron beam, which can be flipped from pulse to pulse. Therefore, the double cell structure of the polarised target is essential to the experimental method. The two cells contain the same target material polarised in opposite directions.

The geometric acceptance of the spectrometer is about 0.28 leading to a nominal luminosity of $\mathcal{L} = 4 \times 10^{31}\mathrm{cm}^{-2}\mathrm{s}^{-1}$ or 400 pb^{-1} for a standard year of data taking. The effective luminosity is lower by the square of the beam and target polarisations and of the fraction of unpolarised nucleons resulting in $\mathcal{L}_{\mathrm{eff}} = 3 \times 10^{29}\mathrm{cm}^{-2}\mathrm{s}^{-1}$.

3.1 The muon beam

A schematic layout of the CERN muon beam line [82, 83] is shown in Fig. 3.1. The muon beam is produced by a primary 450 GeV proton beam from the Super Proton Synchrotron (SPS), which operates with a period of 14.4 s and an extraction time (spill time) of about 2 s. The proton beam with an intensity of typically 5×10^{12}/spill impinges on a 500 mm long and 3 mm thick beryllium plate. Secondary pions and kaons with a momentum band of about 5 % are selected by the first bending magnet and are then transported through a 500 m long structure of focusing and defocusing quadruples along with the lower energy decay muons. At the end of the hadron section the beam is focused onto a 9.9 m long hadron absorber made of beryllium and located 700 m downstream of the production target. At this point the beam contains a muon fraction of about 6 % for the standard pion energy of 208 GeV. Upstream of the absorber the hadron contamination of the beam is less than 10^{-6}. The absorber is located inside the bending magnet, which selects a muon momentum band of about 3 %. In the subsequent 300 m long muon section the beam is cleaned and focused onto the experiment. The original beam line as used for

Figure 3.1: Layout of the CERN muon beam line.

the EMC, BCDMS, and NMC experiments was modified for the SMC experiments to optimise the muon flux and polarisation and to provide an almost dispersion free beam with a sufficiently small beam spot throughout the about 100 m long experimental setup. At the position of the polarised target the beam spot has an root-mean-square width of about 1.6 cm^2.

The muons from the parity violating pion decay $\pi \to \mu\nu$ are naturally longitudinally polarised [84]. The polarisation depends on the decay angle in the pion rest frame with respect to its direction of flight in the laboratory frame. Positive forward (backward) muons are polarised antiparallel (parallel) to their momentum in the laboratory frame. Highest polarisation is obtained for a muon to pion energy ratio close to unity. As a compromise of muon flux and polarisation an operating point of $E_\mu/E_\pi = 0.91$ was chosen at which a polarisation of -0.8 for positive muons was obtained. With the beam line setting used during data taking the resulting intensity of positive muons is 4.5×10^7/spill corresponding to about 10^{-5} muons per incident proton. The maximum muon intensity at 190 GeV is actually limited by the chambers of the spectrometer and/or the sharing of protons between different experiments rather than by the tolerable proton intensity for the production target of about 10^{13}/spill. The SPS can deliver more than 2.5×10^{13} protons/spill to the experiments.

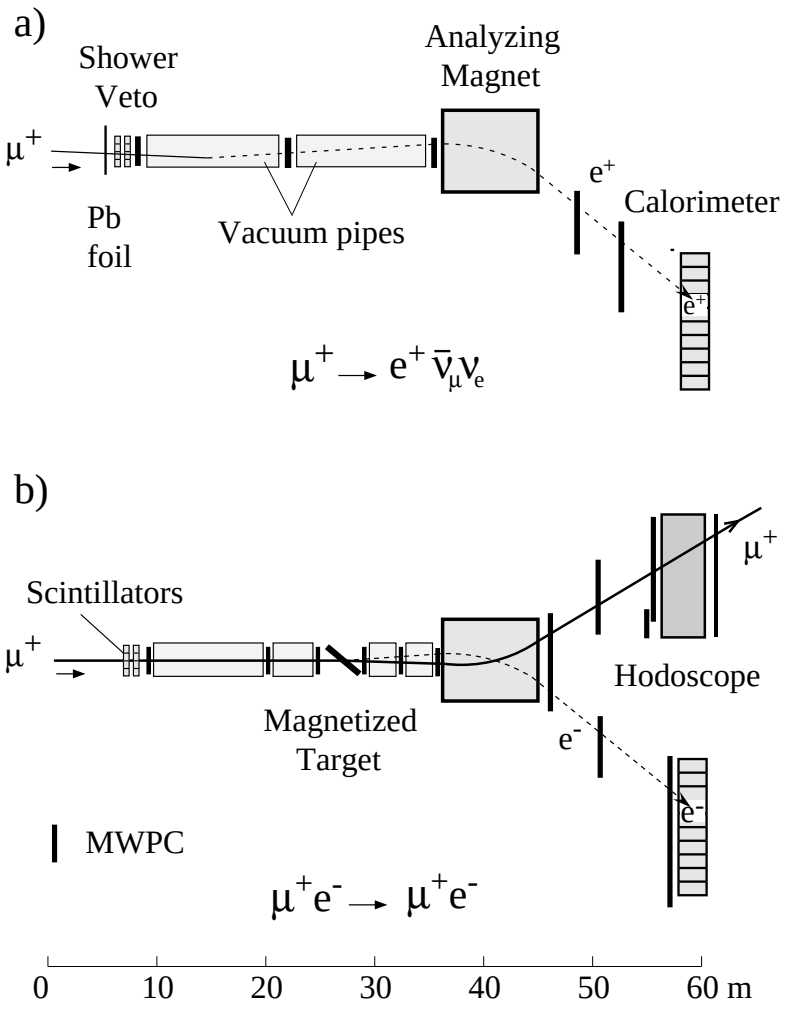

Figure 3.2: Setup of the beam polarimeter: a) for the muon decay experiments and b) for the muon-electron scattering experiments.

3.2 The beam-polarisation measurement

The polarisation of the incoming muon beam, P_μ, is measured with a dedicated spectrometer installed downstream of the main spectrometer and operated simultaneously with it. Two independent methods are used. The first method exploits the dependence of the energy of the decay positron on the polarisation of the parent muon. In the second method the muon polarisation is obtained from the cross-section asymmetry for scattering polarised muons from polarised electrons in a magnetised iron foil. The experimental setups used for the two methods are similar and the analysing magnet and most detectors are in common (Fig. 3.2).

In the muon rest frame the positron from the decay $\mu^+ \to e^+ + \nu_e + \bar{\nu}_\mu$ is preferentially emitted in the direction of the muon spin and its energy distribution was calculated by Michel [85]. For decays in flight the Lorentz boost translates the angular dependence in the rest frame into an energy dependence in the laboratory frame, which is given by [86,87]

$$\frac{dN}{dy} = N_0 \left\{ \frac{5}{3} - 3y^2 + \frac{4}{3}y^3 - P_\mu \left[\frac{1}{3} - 3y^2 + \frac{8}{3}y^3 \right] \right\}, \tag{3.1}$$

where $y = E_e/E_\mu$ is the positron-to-muon energy ratio and N_0 is the number of muon decays. The positron energy spectrum is shown for three different muon polarisations in Fig. 3.3. Our determination of the muon polarisation is based on a measurement of the y slope in the region $y \approx 0.4$, where the sensitivity is largest. A detailed description of the method is given in Ref. [88] and the Ph. D. theses [89–91]. The experimental setup defines a 30 m long muon decay region in which a fraction of 2.5×10^{-5} of the 190 GeV muons decay. It starts downstream of an 8 mm thick lead radiator followed by the shower veto detector, a highly segmented scintillator hodoscope with a horizontal and a vertical plane. Hits in both planes are required in the trigger and the pulse height information is used off line to discriminate positrons produced upstream. In the decay region the muon and the decay positron are tracked by 1 mm pitch multi-wire proportional chambers. In the decay the positron is emitted under angles smaller than 2 mrad and a determination of the decay vertex is not attempted. The decay region ends with the 6 m long analysing magnet, providing a bending power of up to 8.5 Tm. Downstream the positron is tracked by multi-wire proportional chambers with 2 mm pitch and finally its energy is measured in a lead-glass array. An energy deposition larger than 15 GeV is required in the trigger. The momentum measurement of the positron and that of the incident muon, which is in common with the main experiment (Sect. 3.4), were intercalibrated in dedicated runs to reduce the systematic uncertainty in the determination of y. In the off-line reconstruction single tracks are required upstream and downstream of the magnet intersecting in its centre. The latter requirement eliminates muon decays occurring inside the magnet. Positrons are identified by comparing the momentum obtained from the tracking to the energy measured in the lead-glass calorimeter.

Before the muon polarisation can be derived from the positron energy spectrum using Eq. 3.1 the measured raw spectrum must be corrected for the apparatus' acceptance and higher order QED processes. These corrections were determined using a Monte Carlo simulation involving a detailed description of the apparatus and radiative corrections to the muon decay [87]. In terms of the polarisation the radiative corrections amount to 0.07, decreasing the value of $|P_\mu|$. The muon polarisation was then fitted to the corrected spectrum in the range $0.34 \leq y \leq 0.6$ for the 100 GeV data and $0.29 \leq y \leq 0.48$ [89] for 190 GeV data. In these regions the apparatus' acceptance varies by less than 5 %. The largest contributions to the systematic error come from the spectrometer description and from the uncertainty in the radiative corrections.

The results for the polarisation of the 100 GeV [20,88] and 190 GeV muon beams [19,21] are

$$\begin{aligned} P_\mu^{100\ \mathrm{GeV}} &= -0.82 \ \pm 0.06 \ \ (\mathrm{total}) \\ P_\mu^{190\ \mathrm{GeV}} &= -0.807 \pm 0.021\,(\mathrm{stat.}) \pm 0.029\,(\mathrm{syst.}). \end{aligned}$$

The analysis of the data from the polarised muon-electron scattering experiments is still in progress. With the longitudinal polarisations of the muon P_μ ($\to$) and the electron

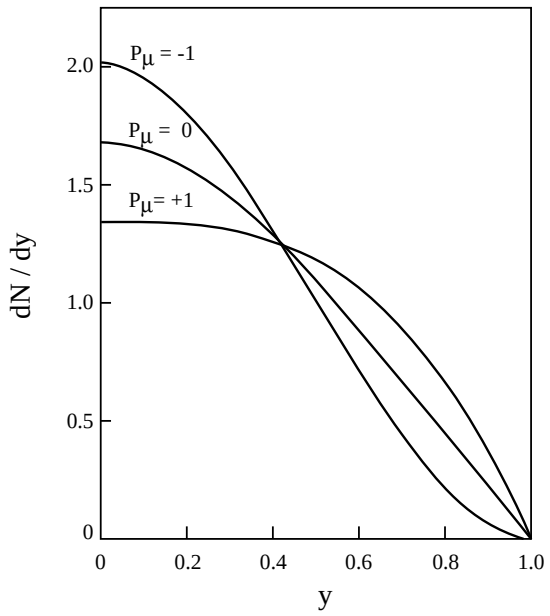

Figure 3.3: Theoretical positron energy spectrum $\mathrm{d}N/\mathrm{d}y$ as function of the positron-to-muon energy ratio y for three different longitudinal polarisations of the muon.

P_e ($\Rightarrow$) the counting rate asymmetry reads

$$A_{\mu\mathrm{e}}^{\mathrm{exp}}(y) = \frac{N^{\rightleftarrows} - N^{\rightrightarrows}}{N^{\rightleftarrows} + N^{\rightrightarrows}} = P_\mu P_\mathrm{e} A_{\mu\mathrm{e}}(y). \tag{3.2}$$

A polarisation measurement is obtained for each bin in $y = E'_\mathrm{e}/E_\mu$, where E'_e is the outgoing electron energy and E_μ is the incident muon energy. The cross-section asymmetry, $A_{\mu\mathrm{e}}$, is given by [92]

$$A_{\mu\mathrm{e}}(y) = y\frac{1 - y/Y + y/2}{1 - y/Y + y^2/2}, \tag{3.3}$$

where $Y = (1 + m_\mu^2/2m_\mathrm{e}E_\mu)^{-1} \approx 1$ is the maximum kinematic limit for y. The apparatus is largely the same as for the muon decay measurements. The main new element is the polarised electron target, located upstream of the analysing magnet in the former decay region. Additional beam chambers track particles upstream and downstream of the target. The analysing magnet is operated with reversed field and the e^- is detected in the lead-glass calorimeter. The scattered muon is bend to the opposite direction, where it is tracked in a second spectrometer arm and finally identified by a hodoscope located upstream of a 2 m thick iron absorber. The polarised electron target is a 2.7 mm thick foil made of a ferromagnetic alloy in a saturated field of 2.3 T. The field along the foil is generated by a conventional magnet system [93] and reversed in every pause between the beam spills. The foil is put under an angle of $\pm 25°$ with respect to the beam to keep the magnet yokes out of the beam region. Runs with opposite angles are combined to cancel the effect of the transverse field component. The average polarisation of the electrons in the foil was obtained from the field using a measurement of the magneto-mechanical ratio for a

similar alloy [94]. The component of the polarisation along the beam direction is found to be $|P_e| = 0.0756 \pm 0.008$. The relative normalisation of the beam flux for the two polarisation directions in the target foil is determined using a random trigger technique. A possibly different acceptance for the unpolarised K-shell electrons due to their higher momentum [95] was investigated and the effect was found to be negligible. The largest contributions to the systematic error come from the uncertainty in the flux normalisation, false asymmetries, and the uncertainties in the target polarisation and the subtraction of background arising from muons creating electron-positron pairs. The preliminary result for the polarisation of the 190 GeV muon beam from muon-electron scattering is

$$P_\mu^{190\ \mathrm{GeV}} = -0.78 \pm 0.03\,(\mathrm{stat.}) \pm 0.02\,(\mathrm{syst.}).$$

The cross-section asymmetries were obtained with a preliminary average of $P_\mu^{190\ \mathrm{GeV}} = 0.79 \pm 0.03$ and the value from the muon decay experiment for the 100 GeV data.

The muon polarisation can also be estimated using a Monte Carlo simulation of the beam transport [96]. The uncertainty in such a calculation arises from the uncertainties in the parent pion and in particular the parent kaon distribution, and in the beam phase over which is integrated. The calculations [83] are in good agreement with the measurements and the quoted uncertainty is 0.05.

3.3 The polarised target

High luminosities with present day muon beams can only be achieved using thick solid state targets. Due to the smallness of the nuclear magneton the proton and deuteron polarisations generated by the Zeeman splitting of the magnetic sublevels in a magnetic field, B, are small, even for strong fields at low temperatures, T. The (vector) polarisations are given by the Curie law, which for spin-$\frac{1}{2}$ and spin-1 particles reads

$$P_{\frac{1}{2}} = \frac{N_{\frac{1}{2}} - N_{-\frac{1}{2}}}{N_{\frac{1}{2}} + N_{-\frac{1}{2}}} = \tanh\left(\frac{\hbar\omega}{2kT}\right) \tag{3.4}$$

and

$$P_1 = \frac{N_1 - N_{-1}}{N_{-1} + N_0 + N_1} = \frac{4\tanh\left(\frac{\hbar\omega}{2kT}\right)}{3 + \tanh^2\left(\frac{\hbar\omega}{2kT}\right)}, \tag{3.5}$$

with $\omega = \mu B/\hbar$ being the Larmor frequency, μ the magnetic moment of the particle, k the Boltzmann constant, and N_m is the population of the magnetic sublevel m. For a typical field of $B = 2.5$ T and a thermal equilibrium temperature of $T = 0.5$ K the polarisations amount to 0.0011, 0.0051, and 0.998 for the deuteron, the proton, and the electron, respectively. The technique of dynamic nuclear polarisation [97] applied in our target systems transfers part of the under these conditions almost complete electron polarisation to the nucleons using microwave irradiation.

The principle of dynamic nuclear polarisation can be illustrated in the simple model of an electron-proton pair in a strong magnetic field, B. In Fig. 3.4 the spin directions of the electron ($\uparrow$) and the proton ($\Uparrow$) in the four possible states are shown. The energy splitting is given by the Larmor frequencies of the electron, $\omega_e/2\pi = 70$ GHz, and the proton, $\omega_p/2\pi = 106$ MHz, for $B = 2.5$ T. At temperature of 0.5 K basically only the two

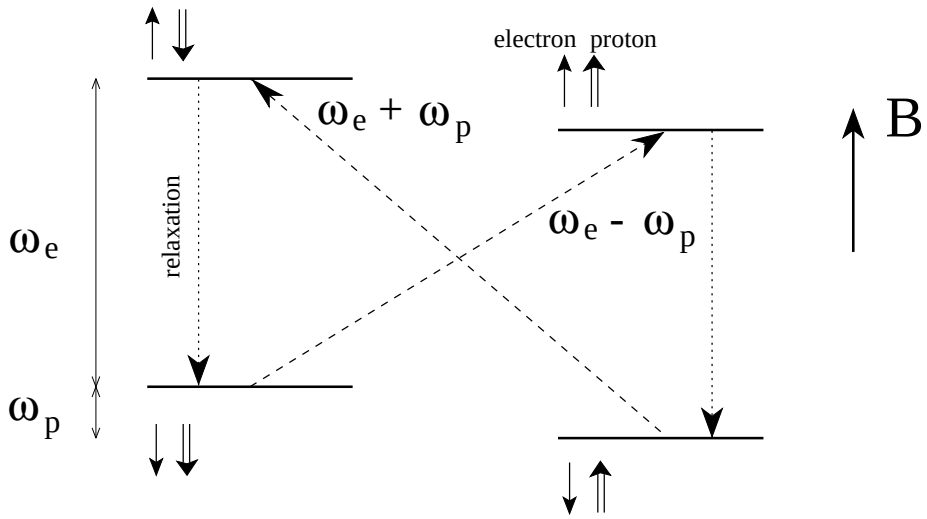

Figure 3.4: Energy levels of an electron-proton pair in a strong magnetic field, B. The arrows indicate the direction of the proton $\Uparrow$ and electron $\uparrow$ spins.

low lying states are populated where the electron's magnetic moment is aligned with the field. The transitions $|\downarrow\Uparrow\rangle \rightarrow |\uparrow\Downarrow\rangle$ and $|\downarrow\Downarrow\rangle \rightarrow |\uparrow\Uparrow\rangle$ shown in Fig. 3.4 can be induced by microwaves with a frequency of $\omega_e + \omega_p$ and of $\omega_e - \omega_p$, respectively. They are followed by immediate relaxation of the electron spin within milliseconds while the relaxation of the proton spin is about 10^6 times slower. This leads to a build-up of a negative (positive) proton polarisation for $\omega_e + \omega_p$ ($\omega_e - \omega_p$). The forbidden double spin-flip transitions can only occur at a considerable rate because of a mixing of the pure states due to the spin-spin interaction (the solid effect). In real materials paramagnetic centres function as 'free' electrons. Protons not close to such a centre are polarised by the mechanism of spin diffusion, which arises from spin-spin interactions between protons.

In 1991/92 the NA47 experiments started out with a deuteron target using the upgraded polarised target system originally designed and constructed by the EMC [17, 98]. An additional dipole coil wound on the microwave cavity enabled us to reverse the target spin orientations by the rotation of the magnetic field vector as described below. However, the dipole field of 0.2 T was not strong enough to hold the polarisation in transverse orientation over a longer period. In parallel a new polarised target system with larger target cells, a more powerful dipole magnet, and a more homogeneous magnetic field was designed and constructed. The new target (Fig. 3.5) was put into operation for the proton experiments in May 1993. This complex target system comprises the target materials located in the target cells, the ^{3}He/^{4}He dilution refrigerator, the microwave system, the superconducting magnet system, and the NMR system for the polarisation measurement. These components are shortly discussed below. Many details of the construction, operation, and performance are given in the Ph. D. theses [99–102].

Materials for which dynamic nuclear polarisation is known to work well include alcohols and ammonia. Both of them contain large fractions of unpolarisable nucleons bound in the carbon, oxygen, and nitrogen nuclei. The paramagnetic centres are in the case of butanol added in form of a chemical dopant, whereas in ammonia they must be generated

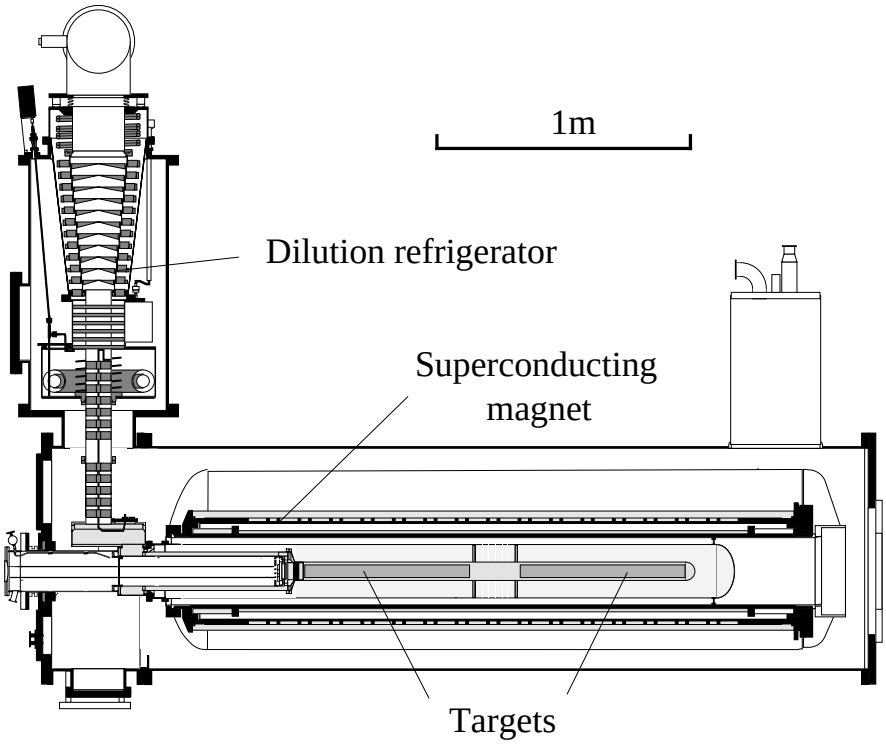

Figure 3.5: Schematic drawing of the SMC polarised target. The muon beam enters from the left side.

by irradiation with particle beams at low temperatures. While NH_3 can be irradiated in a liquid nitrogen cryostat at an external accelerator, the deuterated material, ND_3, must be irradiated *in situ* at liquid helium temperatures. At the SLAC electron beam ND_3 was used successfully [25], but the energy deposited by the muon beam is not sufficient to create enough of these centres. Therefore, ND_3 was not an option for the SMC experiments. In order to have the same chemical material for both, the proton and the deuteron targets and because of its in general simpler handling, butanol, C_4H_9OH, and deuterated butanol were chosen as target materials initially. The error on the cross-section asymmetry is for the same amount of raw data inversely proportional to the fraction of polarisable nucleons in the target material and their polarisation. This fraction is about 1.3 times larger for ammonia than for butanol, roughly 3/17 versus 10/74. Therefore, for our final 1996 proton run an ammonia target was selected, which was produced by and irradiated at the University of Bonn.

The target material is contained in two 650 mm long cylindric cells with a diameter of 50 mm. For the 1993 proton run 600 mm long cells were used. The material in the upstream and the downstream cell has opposite polarisation. In beam direction the two cells are separated by 200 mm. Thus, events can be attributed to a particular target cell using the reconstructed interaction point. The target cells form the innermost part of the target system. The next layers are formed by the mixing chamber, followed by the microwave cavity, and finally by the magnet coils and their cryostat.

The principle of the $^3He/^4He$ dilution refrigerator is based on the fact that at temper-

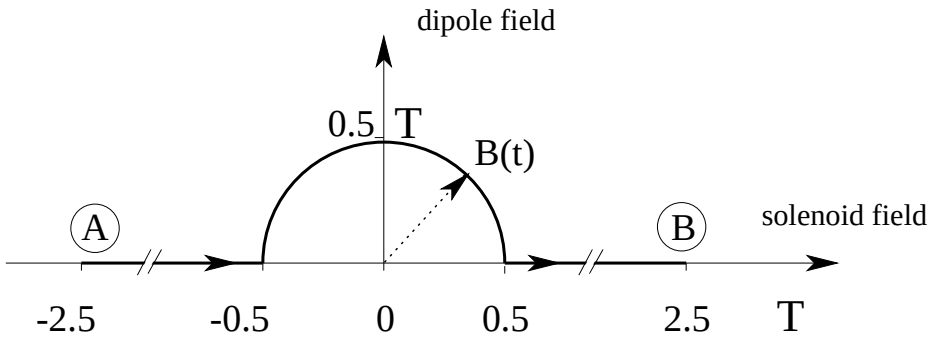

Figure 3.6: Superposition of the solenoid and dipole magnetic fields, $B(t)$, during a reversal of the target spins by a field rotation, starting e.g. at point A and ending at point B.

atures below 0.87 K a mixture of ^{3}He and ^{4}He separates into a ^{3}He rich phase and a ^{4}He rich phase, usually called the dilute phase. The lighter ^{3}He rich phase swims on top of the dilute phase. Pumping on the dilute phase reduces the ^{3}He concentration in it due to the higher vapour pressure of ^{3}He. Cooling occurs by the transition of the more energetic ^{3}He atoms from the ^{3}He rich phase to the dilute phase. The principle is similar to that of an evaporation refrigerator where the part of the vapour phase is taken by the dilute phase. However, the decisive difference is that the ^{3}He concentration in the dilute phase does not vanish at zero temperature, but approaches a value of 6.5 %. Thus, a dilution refrigerator works down to very low temperatures, while a ^{4}He evaporation refrigerator is limited to about 1 K due to the decreasing vapour pressure. In the SMC dilution refrigerator [103] the ^{3}He rich phase and the dilute phase coexist in the mixing chamber, which contains the target cells. The pumping on the dilute phase occurs in the still, which is heated to about 1 K and is connected to the mixing chamber via a heat exchanger. The helium vapour is then compressed by eight roots blower pumps, precooled using an external ^{4}He supply, and finally fed back via the heat exchanger into the upper ^{3}He rich phase in the mixing chamber. The cooling power is determined by the rate at which the phase transition of the ^{3}He occurs, i.e. the pumping speed. With the pumping rate of 13500 m^3/h a cooling power of about 1 W is obtained at 400 mK, which is a typical temperature in the polarising mode with microwave irradiation. When the microwave power is switched off, the target can be operated in "frozen spin" mode at 30–50 mK.

Two independent microwave sources of the extended-interaction-oscillator type provide the different microwave frequencies needed to generate opposite polarisations in the two target cells. One of them is connected to the upstream part and the other to the downstream part of the 1700 mm long and 210 mm wide microwave cavity. The two parts of the cavity are separated by microwave stoppers providing an attenuation of 20–30 dB. The inner part of the microwave stopper is located in the gap between the target cells inside the mixing chamber and was constructed in a way that a free flow of the helium coolant is not hindered. During the process of polarisation the polarisation increase is monitored continuously and the microwave frequencies are adjusted to obtain fastest polarisation growth. Typical polarisation build-up times are a few hours, but to obtain the maximum value takes several days. During the 1992 deuteron run we found accidentally

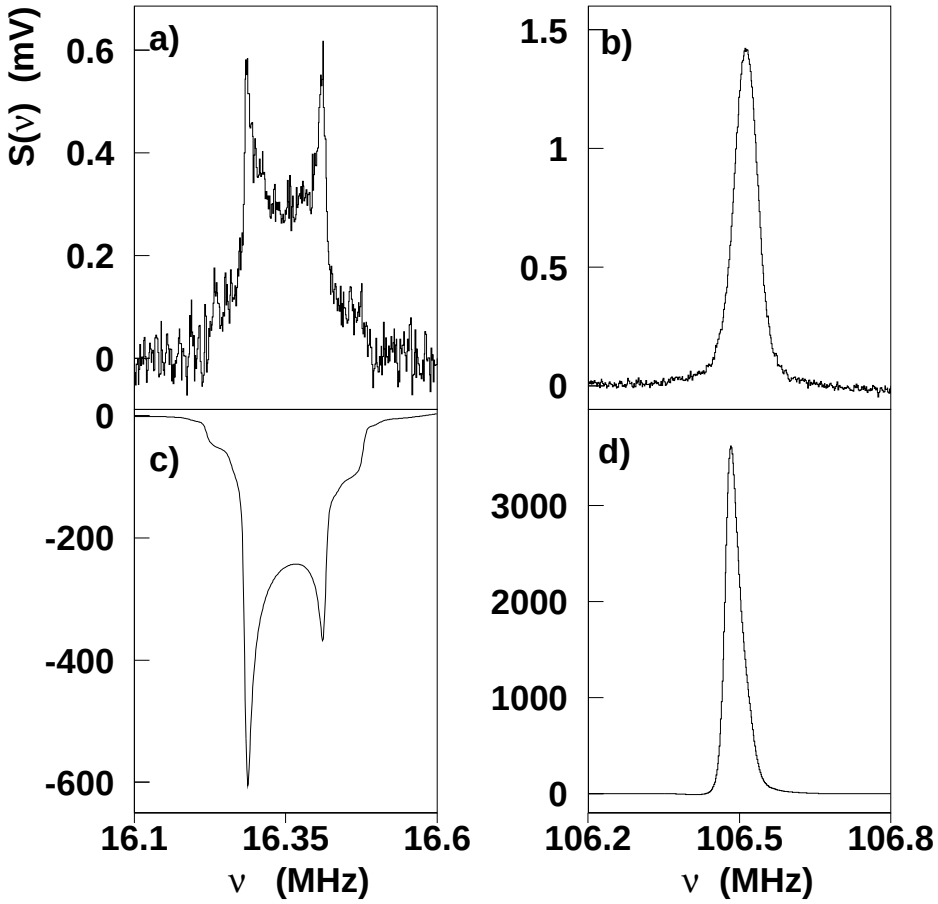

Figure 3.7: NMR signal S as function of the oscillator frequency $\nu = \omega/2\pi$ for the deuteron (left) and the proton (right). The calibration signals in the upper row are taken with the natural polarisation at 1 K and the signals from the highly polarised nuclei in the bottom row were taken at $P_{\mathrm{d}} = -0.48$ and $P_{\mathrm{p}} = 0.77$. For the proton an ammonia signal is shown.

that a modulation of the microwave frequency with an amplitude of 30 MHz and a frequency in the order of 1 kHz has a dramatic effect on the polarisation of deuterons in butanol, increasing the final value from 0.2 to above 0.4 [104, 105]. Only a small increase of 0.05 in the already high polarisation of the proton material was observed.

The superconducting magnet system [106] comprises the main solenoid, 16 correction coils, and a saddle-type dipole coil. The solenoid together with the correction coils provides a longitudinal field of 2.5 T with a homogeneity of $\Delta B/B = \pm 3.5 \times 10^{-5}$ over the target volume of 1500 mm length and 50 mm diameter. To invert the spin directions in the target material the solenoid field is first ramped down to 0.5 T and then varied together with the dipole field in a way that the resulting field vector rotates slowly from the initial orientation, e.g. antiparallel to the beam, to the final parallel orientation (Fig. 3.6). The procedure is performed in frozen spin mode at about 50 mK were the spin-lattice relaxation time exceeds 1000 h for the maximum dipole field of 0.5 T. For the measurement of the structure function g_2 the rotation can be interrupted at the intermediate state, where the

target is transversely polarised. For the computer controlled reversal procedure [107] the beam has to be interrupted for only about 10 min.

The polarisation is measured by an 10-channel continuous wave NMR system [104,108]. Five NMR coils connected to series Q-meter circuits [109] were placed in each of the target cells. The coils were embedded in the target material except for the 1994 deuteron run, where they were mounted on the outer surface of the target cells. The oscillator frequency is swept over a full range of 400–600 Hz around the proton's (deuteron's) Larmor frequency, $\omega_{\rm p}/2\pi = 106$ MHz ($\omega_{\rm d}/2\pi = 16$ MHz). The signal is a superposition of the parabola-shaped Q-curve given by the characteristics of the circuit and the NMR signal. The Q-curve is measured in dedicated runs, where the Larmor frequency is shifted out of the resonance of the circuit by increasing the solenoid field by 5 %. This is usually done when ramping up the solenoid at the end of a field rotation. After subtraction of the Q-curve the area under the signal is proportional to the wanted polarisation. The area is calibrated about three times per year by dedicated measurements of the small natural polarisation in thermal equilibrium, where the polarisation is well known from the Curie law, Eq. 3.5. A stable temperature is guaranteed by performing the calibration at $T = 1$ K with ^{4}He rather than in the dilution mode. In Fig. 3.7 the calibration signals and the signals from the polarised material are shown for both, the proton and the deuteron. The measurement of the deuteron signal is particularly difficult because of the small polarisation of 0.0005 and the broadening of the signal due to the interaction of the deuteron's quadrupol moment with the electric field gradient in the C–D and O–D bonds.

The radial homogeneity of the deuteron polarisation was investigated using small coils placed in the inner and outer target regions at the same longitudinal position. No significant radial dependence was found and the uncertainty is included in the errors. The final accuracy of the target polarisation measurements is $\Delta P/P = 0.03$ for the proton and 0.054 for the deuteron.

The spin directions in the target cells were reversed by rotation of the magnetic field three or five times per day. The polarisation was also reversed by microwaves every few weeks, to cancel possible systematic effects connected to the direction of the solenoid field. Within the statistical precision, such effects were never observed. The average polarisations are 0.86 for the proton and 0.48 for the deuteron (in 1994) with maximum polarisations of 0.94 and 0.61, respectively.

3.4 The spectrometer and event reconstruction

The most upstream part of the spectrometer is the beam momentum station (BMS) at the end of the beam line tunnel close to the experimental area. The momentum of the incident muon is measured using two telescopes of scintillator hodoscopes located upstream and downstream of the last vertical bending magnet as indicated in Fig. 3.1. The hits in the four planes are correlated by their time information. For the standard muon energy of 190 GeV the precision of the momentum measurement is $\Delta p/p = 5 \times 10^{-3}$.

The general layout of the NA47 spectrometer is shown in Figs. 3.8 and 3.9 and the detector properties summarised in Table 3.1. It was originally designed by the EMC [110] and then used by the NMC. Upstream of the polarised target the beam is tracked by two scintillator hodoscopes stations (BHA and BHB) with a lever arm of 10 m. The in total 16 planes in 4 orientations are made of 20 scintillator strips each covering an area of 80×80 mm^2. Planes of the same orientation are staggered yielding an effective

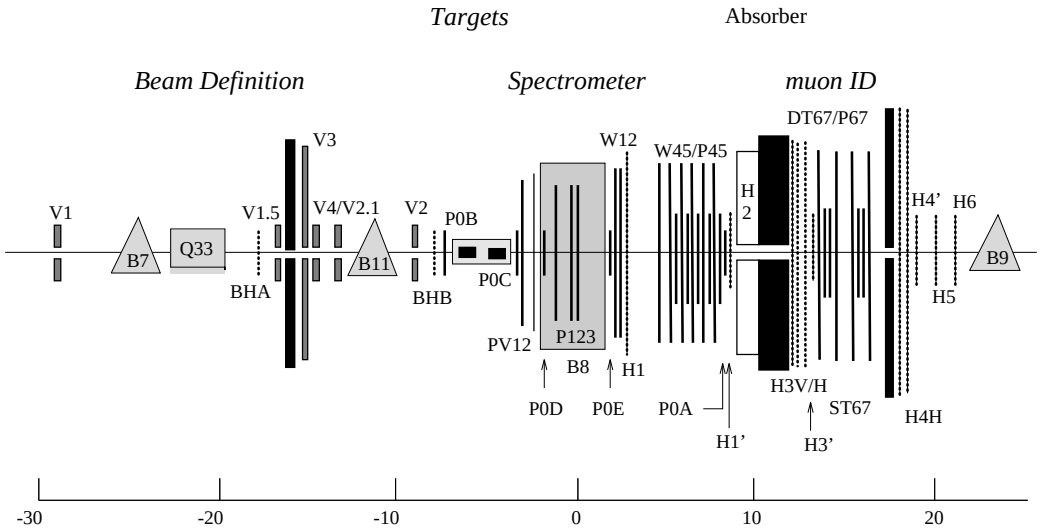

Figure 3.8: Schematic view of the SMC spectrometer.

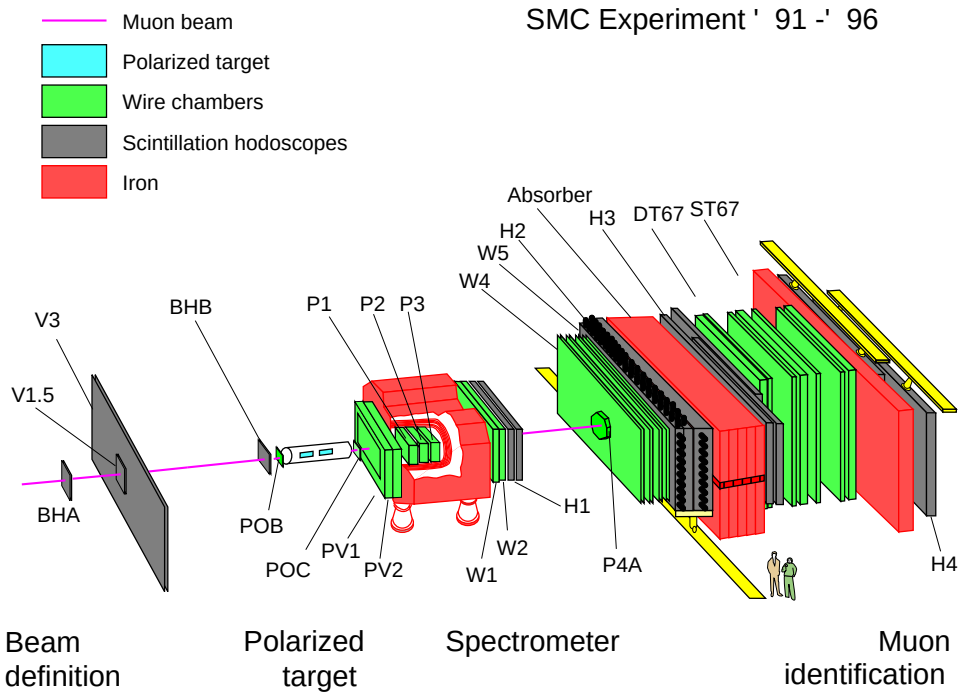

Figure 3.9: Artist's view of the SMC spectrometer.

Table 3.1: Detectors of the main spectrometer.

Hodo-scope	Modules ×Planes	Pitch (cm)	Size (cm)	Wire-chamber	Modules ×Planes	Pitch (cm)	Size (cm)	Dead zone(cm)
BHA-B	2×8	0.4	8×8	P0A-E	5×8	0.1	⊘ 14	—
V123	5×1	—	various	PV1	1×4	0.2	150×94	—
H1	2	7.0	250×130	PV2	1×6	0.2	154×100	⊘ 8
H2 cal	4	28.0	560×280	P1ab23	4×3	0.2	180×80	⊘ 13
H3	2	15.0	750×340	W12	2×8	2.0	220×120	⊘ 12
H4	1	15.0	996×435	W45	6×4	4.0	530×260	⊘ 13–25
H1',3',4'	1	1.4	50×50	P45	5×2	0.2	⊘ 90	⊘ 12
S1,2,4	1	—	various	ST67	4×8	1.0	410×410	⊘ 16
				P67	4×2	0.2	⊘ 90	⊘ 12
				DT67	3×4	5.2	500×420	83×83

resolution of $2/\sqrt{12}$ mm. The spatial resolution is improved by a multi-wire proportional chamber, P0B, of the so-called P0-type with eight staggered planes of 1 mm pitch in four orientations installed close to the second hodoscope station (BHB) just upstream of the polarised target. From 1995 onwards the resolution was further improved by micro-strip gas chamber telescopes located upstream and downstream of the polarised target [111].

The event reconstruction starts with the trajectory of the beam muon, which is determined with a precision of about 0.1 mrad. No tracking is performed in the about 70 m long region between the beam momentum station and the first beam hodoscope (BHA). The beam track is correlated to the momentum measurement by timing. To hold the target spins in transverse orientation the dipole field of the polarised target is turned on during the g_2 measurements performed at 100 GeV. To compensate the bending power of 1.05 Tm an additional dipole magnet, B11, upstream of the target deflects the beam in a way that it is brought back to its nominal position by the target's dipole field.

Downstream of the polarised target the scattered muon spectrometer determines the muon's trajectory and momentum, using more than 100 planes of tracking devices upstream and downstream of a conventional large-aperture forward spectrometer magnet, the FSM. We start the description of this part of the spectrometer at the downstream end, where the reconstruction procedure for the scattered muon begins, and proceed from there to the target. A two metre thick hadron absorber made of iron filters out the muon, which is then tracked downstream by 16 planes of plastic streamer tubes of 1 cm cell size equipped with a 32-plane strip read-out [112–115]. Because of the high particle flux the streamer tubes cannot be operated in the high voltage plateau. This causes a strong dependence of the chamber efficiencies on the temperature and pressure of the chamber gas. Therefore a feedback loop was developed [112,114] stabilising the streamer charge and thus the chamber efficiency by adjusting the high voltage. The streamer charge is measured on the sense wires of a small dedicated chamber connected to the same gas system and placed in the beam halo. Close to the beam multi-wire proportional chambers, P67, back up the detection system. The outer region is also covered by drift tube detectors, DT67. There is no need of a high spatial resolution in this region because of the multiple scattering in the absorber. Once the scattered muon is found its track is extrapolated backward through the absorber and the 2 m thick calorimeter, H2, consisting of an electromagnetic and a hadronic section. The information from the chambers downstream of the absorber

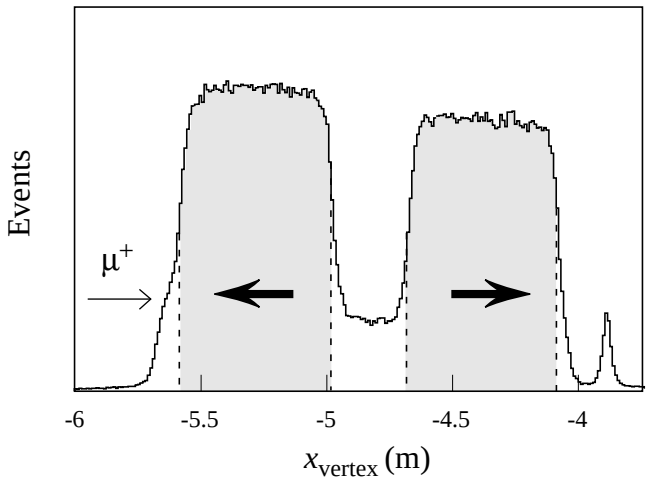

Figure 3.10: Reconstructed interaction vertices along the beam direction. The vertices between the two target cells arise from the ^{3}He/^{4}He coolant.

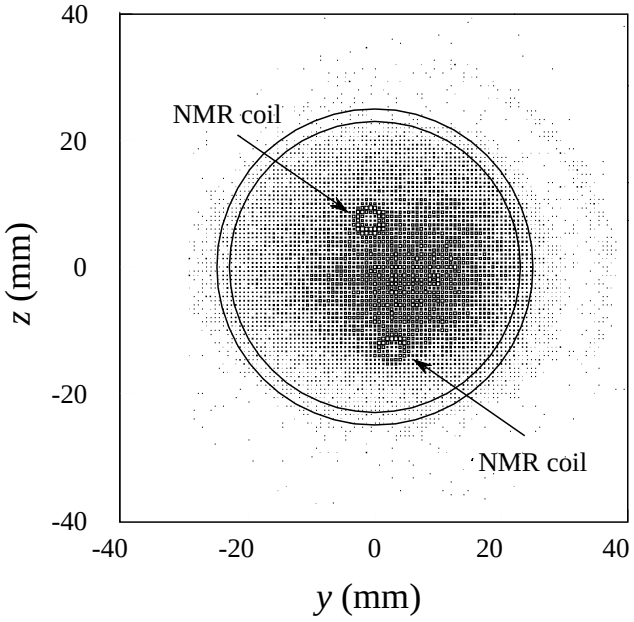

Figure 3.11: Reconstructed interaction vertices perpendicular to the beam direction. Also visible is a cross section through a one-loop NMR coil made from a thin hollow tube.

is discarded because of its limited precision once an upstream continuation of the track is found.

The next step is to search for tracks in the field free region between the spectrometer magnet and the calorimeter within in a certain road width around the extrapolated muon track. The large drift chambers, W12, with 16 planes at the upstream end and W45 with 24 planes at the downstream end of this region, are deadened in the beam region and are backed up by the multi-wire proportional chambers, P0E with 8 planes and P45 with

10 planes. It is also searched for tracks not having a continuation behind the absorber, belonging to electrons or hadrons, which can be distinguished by the ratio of energy deposited in the electromagnetic part of the calorimeter to the total deposited energy. The hadron tracks are used in the analysis of semi-inclusive data, see Sect. 4.2.3.

Next towards the target is the spectrometer magnet with an aperture of 2×1 m^2, which was operated with bending powers of 2.3 Tm and 4.4 Tm for the two beam energies of 100 GeV and 190 GeV, respectively. For the pattern recognition the detection of the particle trajectories inside the 4 m long spectrometer magnet is mandatory because of the high particle multiplicities of the events and the length of the magnet. Initially three multi-wire proportional chambers, P1, P2, and P3, with three planes each were located inside the magnet, but it turned out that the redundancy of this system was marginal and caused the largest contributions to the false asymmetries due to efficiency variations. Therefore a fourth chamber and a feedback system similar to the one discussed for the streamer tubes were installed in 1993 [116]. The gain of the gas amplification is monitored in a dedicated small chamber in which a ^{55}Fe source is incorporated. The 5.9 keV photons are absorbed by the K-shell electrons of argon and the emitted photo-electrons provide a constant number of electron-ion pairs. The reconstruction in the field volume is the most complicated part and the addition of the fourth chamber required major modifications in the complex pattern recognition algorithm [112]. The reconstruction starts with the non-dispersive vertical projection, where the tracks are straight lines. In the dispersive plane the tracks downstream of the magnet are connected by arcs to the various hits in the magnet chambers demanding that the resulting upstream track points to the target. If enough hits are found on the arc the particle's momentum is determined in a spline fit [117] using a detailed map of the magnetic field. When several possible continuations are found, the one with the best chi-square value of the fit is kept.

The scattering angle is mainly determined by the chambers between the polarised target and the spectrometer magnet. Apart from the microstrip gas chambers in use since 1995, in this region only multi-wire proportional chambers are used. Large 2 mm pitch chambers, PV1 and PV2 with together 10 planes, cover the upstream magnet aperture, beam chambers of the P0-type, P0C and P0D with 8 planes each, cover the beam region. The final trajectory is refitted using the information from all track segments between the polarised target and the hadron absorber. In this fit the momentum of the scattered muon and its direction are determined with an average precision of $\Delta p'_\mu/p'_\mu = 1$ % and of 0.4 mrad, respectively.

The final step is the vertex finding in which the scattered muon track and the beam track are propagated into the target field using a Runge–Kutta integration. The average energy loss and the increasing uncertainty of the track parameters due to multiple scattering in the target material are taken into account. Average uncertainties in the reconstruction of the interaction vertex are 0.3 mm transverse to the beam and 30 mm in beam direction, the latter depending strongly on the scattering angle. The reconstructed interaction vertices are shown in Figs. 3.10 and 3.11. The interaction point defines the target cell and thus the polarisation of the target nucleon.

The trigger logics is shown in Fig. 3.12. It is based on the recognition of the scattered muon and does not include the beam muon. Due to the high flux of halo muons compared to the interaction rate a sophisticated veto system is indispensable to avoid that halo muons are confused with scattered muons. Altogether five veto scintillator walls, located between the beam momentum station and the polarised target, cover areas ranging from 6×4 m^2

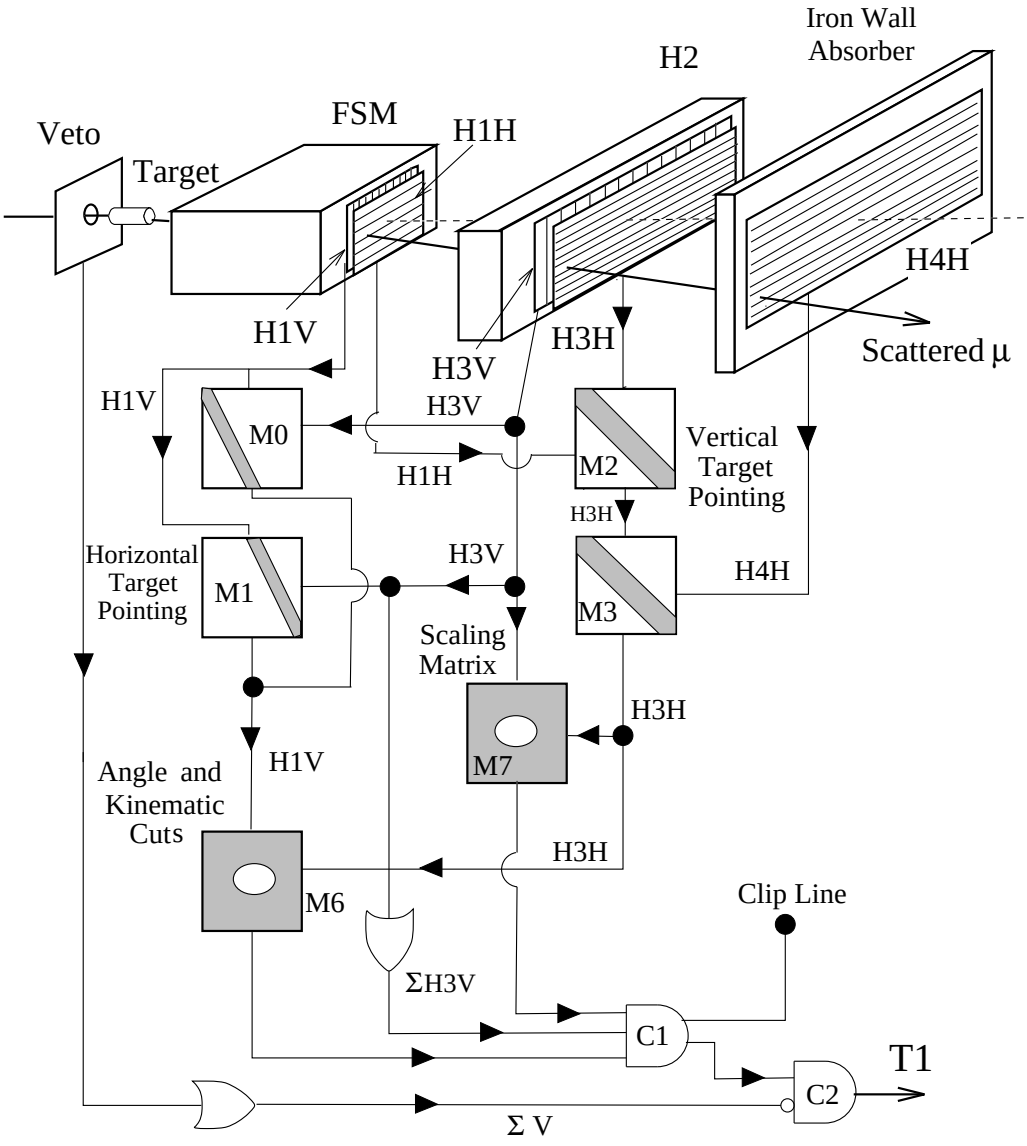

Figure 3.12: Logics of the main physics trigger.

Table 3.2: Data taking of the SMC experiment.

Year	Beam energy (GeV)	Experiment	Target material		Target polarisation	Events after cuts (10^6)
1991	100	setup	deuteron	butanol	0.20	—
1992	100	$A_{\parallel}$	deuteron	butanol	0.22–0.38	3.5
1993	190	$A_{\parallel}$	proton	butanol	0.86	4.5
	100	$A_{\perp}$	proton	butanol	0.80	0.9
1994	100	$A_{\parallel}$	deuteron	butanol	0.49	6.4
1995	100	$A_{\parallel}$	deuteron	butanol	0.50	8.5
	190	$A_{\perp}$	deuteron	butanol	0.44	2.5
1996	190	$A_{\parallel}$	proton	ammonia	0.89	

to 25×25 cm^2. The one closest to the target has the smallest beam hole with a diameter of about 7 cm. The trigger uses coincidences between five planes of scintillator hodoscopes located upstream of the spectrometer magnet (H1), downstream of the hadron absorber (H3) and downstream of a second 40 cm thick absorber at the very end of the spectrometer (H4). In the first two locations two planes with vertical and horizontal strips of 10–15 cm width are installed, while the last detector consists of only horizontal strips, sensitive to the non-dispersive coordinate. The coincidences between the strips of different planes are programmable and optimised using Monte Carlo simulations. The patterns provide target pointing in the non-dispersive and to some extend in the dispersive coordinate, a minimum angle cut, and a cut on the fraction of radiative events. The trigger is reasonably clean and about 60 % of the registered events can be fully reconstructed. In addition to the main physics trigger, there are dedicated triggers for small scattering angles and the small x region [118], as well as a calorimetric trigger and triggers for calibration purposes and online monitoring.

3.5 Data taking

The NA47 experiment was set up in 1991 with a deuteron target and the modified polarised target system of the EMC. Data taking started in 1992 and in 1993 the SMC polarised target was put into operation with a proton target. Table 3.2 summarises the operation of the NA47 experiment from 1991–1996. The experiment was running during the full SPS proton operation period, typically 120 days per year. The combined availibitity of spectrometer and target was above 90 %. In Fig. 3.13 the integerated beam flux (accumulated H5) and the accumulated data runs are shown together with the polarisation in the two target cells and the beam intensity (H5) as a function of time for the entire 1993 operation.

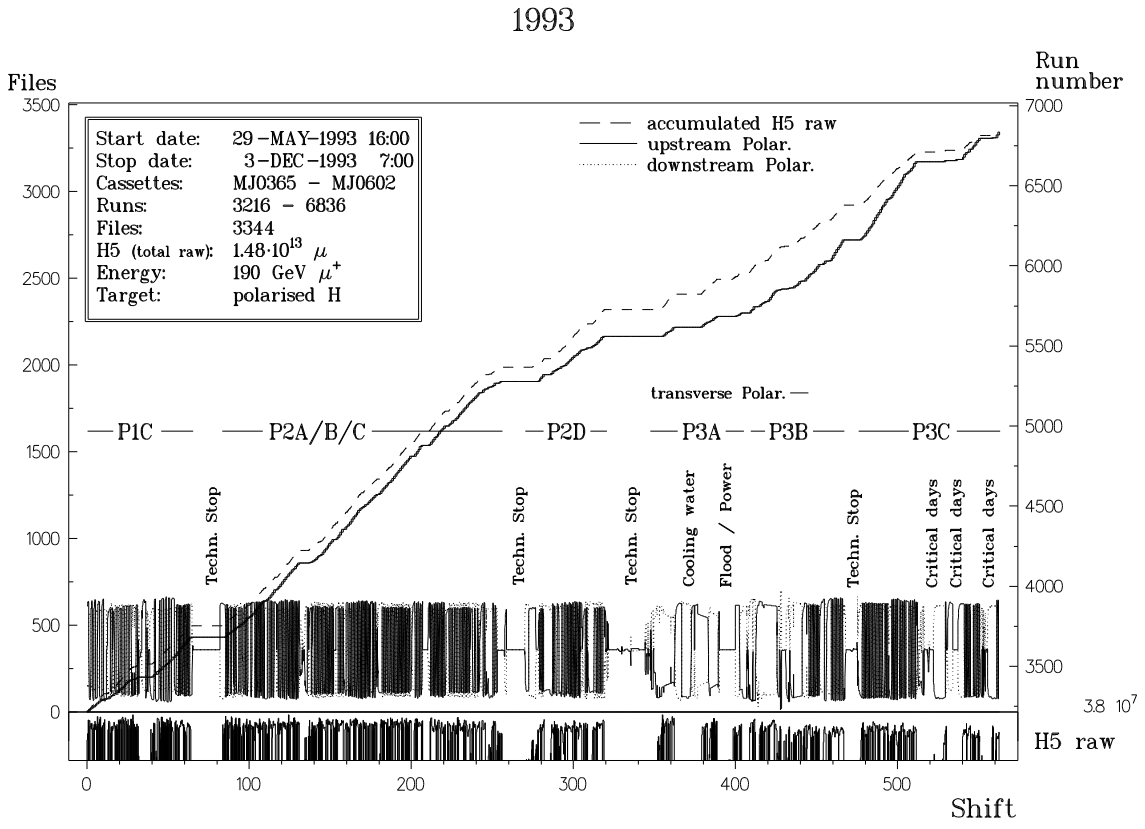

Figure 3.13: Integrated muon flux, accumulated data runs, target polarisation, and beam intensity as a function of time (1 shift = 8 h) for the entire 1993 data taking.

Chapter 4

Analysis of the SMC data

In this chapter we discuss the technical details of the analysis. At the end the main SMC results are given. However, the comparison with data from other experiments and the discussion of the physics implications are deferred to chapter 5, where these topics are discussed in a broader context.

4.1 Evaluation of the asymmetries

The evaluation of the cross-section asymmetries from the event numbers takes full advantage of the double-cell target setup. In the evaluation of the longitudinal asymmetry, A_1, the asymmetry A_2 is assumed to vanish, which for the SMC kinematics is a good approximation. The asymmetries are determined in bins of x averaging over the Q^2 range of the data in the x bin. We assume that the ratio g_1/F_1 scales rather than A_1 and therefore average the quantity $\mathcal{A}_1$ defined by

$$\mathcal{A}_1 := \frac{A_{\parallel}}{\mathcal{D}} \approx \frac{A_1}{1+\gamma^2} \approx \frac{g_1}{F_1}, \tag{4.1}$$

with $\mathcal{D} = D(1+\gamma^2)$ and $\gamma^2 = Q^2/\nu^2$. For the SMC kinematics the factor $1+\gamma^2$ deviates at most by 1.5 % from unity at large x and thus $\mathcal{D} \simeq D$ and $\mathcal{A}_1 \simeq A_1$. The asymmetries are also analysed in (x, Q^2) bins to study Q^2 dependences.

In the following sections the asymmetries for the proton and the deuteron are discussed together. If different, formulæ and examples refer to the proton case unless otherwise stated.

4.1.1 Event yields

The number of events, N, from a target cell is given by

$$N = a\left\{\left(\Phi^{\rightarrow} n_{\mathrm{p}}^{\Rightarrow} + \Phi^{\leftarrow} n_{\mathrm{p}}^{\Leftarrow}\right)\sigma^{\overrightarrow{\Rightarrow}} + \left(\Phi^{\rightarrow} n_{\mathrm{p}}^{\Leftarrow} + \Phi^{\leftarrow} n_{\mathrm{p}}^{\Rightarrow}\right)\sigma^{\overrightarrow{\Leftarrow}} + \Phi\sum_A n_A\sigma_A\right\}, \tag{4.2}$$

with the acceptance, a, the integrated muon flux, $\Phi = \Phi^{\rightarrow} + \Phi^{\leftarrow}$, the number of polarisable protons per unit area, $n_{\mathrm{p}} = n_{\mathrm{p}}^{\Rightarrow} + n_{\mathrm{p}}^{\Leftarrow}$, and the differential cross sections integrated over the x and Q^2 interval, σ. The sum runs over all nuclei, A, in which the unpolarisable

nucleons are bound, and n_A and σ_A are the corresponding number of nucleons and cross sections. With the beam and target polarisations and the cross-section asymmetry

$$P_\mu = \frac{\Phi^{\rightarrow} - \Phi^{\leftarrow}}{\Phi^{\rightarrow} + \Phi^{\leftarrow}}, \qquad P_t = \frac{n_{\mathrm{p}}^{\Rightarrow} - n_{\mathrm{p}}^{\Leftarrow}}{n_{\mathrm{p}}^{\Rightarrow} + n_{\mathrm{p}}^{\Leftarrow}}, \qquad A_{\parallel} = \frac{\sigma^{\rightleftarrows} - \sigma^{\rightrightarrows}}{\sigma^{\rightleftarrows} + \sigma^{\rightrightarrows}}, \tag{4.3}$$

we can cast Eq. 4.2 in the form

$$N = a\Phi\hat{n}\hat{\sigma}\left\{1 - P_\mu P_t f A_{\parallel}\right\}. \tag{4.4}$$

For positive polarisations the spins point along the beam direction. The average cross section for the unpolarised target material is given by $\hat{\sigma} = (n_{\mathrm{p}}\bar{\sigma} + \sum_A n_A\sigma_A)/\hat{n}$, with the total number of nucleons per unit area, $\hat{n} = n_{\mathrm{p}} + \sum_A n_A$ and the spin-averaged proton cross section, $\bar{\sigma} = \frac{1}{2}(\sigma^{\rightleftarrows} + \sigma^{\rightrightarrows})$. The dilution factor, f, accounts for the unpolarisable nucleons and is given by

$$f = \frac{n_{\mathrm{p}}\bar{\sigma}}{n_{\mathrm{p}}\bar{\sigma} + \sum_A n_A\sigma_A}. \tag{4.5}$$

Equation 4.4, which is the starting point for the evaluation of the cross-section asymmetry $A_{\parallel}$, also holds for the deuteron with the polarisation defined in Eq. 3.5 and assuming that the structure function b_1^{d} vanishes (Eq. 2.52).

4.1.2 Asymmetry evaluation

Several methods to determine the asymmetry $A_{\parallel}$ from Eq. 4.4 were investigated [119,120]. The questions addressed are the stability with respect to possible false asymmetries arising from time-varying acceptances, the treatment of the time variation of the polarisations, and the different analysing power of events in the same x bin due to the variation of the (modified) depolarisation factor, $\mathcal{D}$, and the dilution factor, f, with Q^2. The latter varies due to the strong sensitivity of the radiative corrections on $y = Q^2/(2xME)$. The splitting into too small (x, Q^2) bins causes biases owing to small event numbers in a single bin. The method finally adopted [121] weights each event with its analysing power, $f\mathcal{D}$. The asymmetries obtained from two consecutive data sets with opposite target polarisations are averaged to cancel the different acceptances for the two target cells. The method is derived as the weighted average of the asymmetries obtained in hypothetical Q^2 bins for fixed x in the limit of infinitesimally small bin sizes. It can also be obtained from a maximum likelihood principle [111, 122]. Possible biases introduced by the method were studied using Monte Carlo simulations [120] with the actual size and kinematics of our data sets. Within the accuracy of these studies no bias was found. In a refined re-analysis presently being carried out [123] the weighting is extended to include the variation of the beam polarisation with the incident muon energy on an event-by-event basis. Such a dependence in the order as expected for a fixed parent-pion energy was found in a recent still preliminary analysis of the beam polarisation [91].

In the counting rate asymmetry constructed from the event numbers originating in the upstream and downstream target cells,

$$A_N = \frac{N_{\mathrm{u}} - N_{\mathrm{d}}}{N_{\mathrm{u}} + N_{\mathrm{d}}}, \tag{4.6}$$

the average cross section, $\hat{\sigma}$, and the integrated muon flux Φ, cancel. This asymmetry ranges from 0.004 at small x to 0.02 at large x. From Eq. 4.4 we find

$$A_N = \frac{t_\mathrm{u} - t_\mathrm{d} - P_\mu f A_{||} (t_\mathrm{u} P_\mathrm{u} - t_\mathrm{d} P_\mathrm{d})}{t_\mathrm{u} + t_\mathrm{d} - P_\mu f A_{||} (t_\mathrm{u} P_\mathrm{u} + t_\mathrm{d} P_\mathrm{d})}, \tag{4.7}$$

with $t = a\hat{n}$. Each of the factors P_μ, f, and $A_{||}$ is smaller than one and in our setup $P_\mathrm{u} \simeq -P_\mathrm{d}$ and $t_\mathrm{u} \simeq t_\mathrm{d}$. Therefore the last term in the denominator is in the order of 10^{-3} of the first term $t_\mathrm{u}+t_\mathrm{d}$ and will be neglected in the following. Now we consider the mean of two counting rate asymmetries, e.g. A_N^i measured with inward pointing polarisations for the two target cells, ($\boxed{\Rightarrow}\,\boxed{\Leftarrow}$), and A_N^o with outward pointing polarisations, ($\boxed{\Leftarrow}\,\boxed{\Rightarrow}$). In their mean, the ratio $(t_\mathrm{u} - t_\mathrm{d})/(t_\mathrm{u} + t_\mathrm{d})$ cancels to the extent that $t_\mathrm{u,d}^\mathrm{i} = t_\mathrm{u,d}^\mathrm{o}$ and we obtain

$$\mathcal{A}_1 = -\frac{1}{2 P_\mu P_t f \mathcal{D}} \left(A_N^\mathrm{i} - A_N^\mathrm{o} \right) - \mathcal{A}_\mathrm{false} \tag{4.8}$$

with the "false" asymmetry due to acceptance variations

$$\mathcal{A}_\mathrm{false} = -\frac{1}{2 P_t P_\mu f \mathcal{D}} \left\{ \left(\frac{t_\mathrm{u} - t_\mathrm{d}}{t_\mathrm{u} + t_\mathrm{d}} \right)^\mathrm{i} - \left(\frac{t_\mathrm{u} - t_\mathrm{d}}{t_\mathrm{u} + t_\mathrm{d}} \right)^\mathrm{o} \right\}. \tag{4.9}$$

The average target polarisation ($P_\mathrm{u}^\mathrm{i} \simeq -P_\mathrm{u}^\mathrm{o}$, etc.) is given by

$$P_t = \frac{1}{2} \left\{ \left(\frac{t_\mathrm{u} P_\mathrm{u} - t_\mathrm{d} P_\mathrm{d}}{t_\mathrm{u} + t_\mathrm{d}} \right)^\mathrm{i} - \left(\frac{t_\mathrm{u} P_\mathrm{u} - t_\mathrm{d} P_\mathrm{d}}{t_\mathrm{u} + t_\mathrm{d}} \right)^\mathrm{o} \right\}. \tag{4.10}$$

To take into account the variation of Q^2 and thus of f and $\mathcal{D}$ within a particular x bin, the procedure can be generalised to the weighted average of the $A_N/f\mathcal{D}$ values for infinitesimally small Q^2 bins. The variation of $A_N/f\mathcal{D}$ with Q^2 within an x bin is small. For small asymmetries the number of events from the two target cells is similar and the statistical error of A_N becomes $(N_\mathrm{u} + N_\mathrm{d})^{-1/2}$. It is convenient to introduce the weights, $w = (f\mathcal{D})^2$, and the subscripts, u and d, which run over the events from the upstream and the downstream target cell, respectively. With these definitions the weighted average of $A_N/f\mathcal{D}$ takes the form

$$\left\langle \frac{A_N}{f\mathcal{D}} \right\rangle = \frac{\sum w_u^{1/2} - \sum w_d^{1/2}}{\sum w_u + \sum w_d}. \tag{4.11}$$

The asymmetry $\mathcal{A}_1$ is then obtained by replacing $A_N/f\mathcal{D}$ in Eq. 4.8 by $\langle A_N/f\mathcal{D} \rangle$

$$\mathcal{A}_1 = -\frac{1}{2 P_\mu P_t} \left\{ \left(\frac{\sum w_u^{1/2} - \sum w_d^{1/2}}{\sum w_u + \sum w_d} \right)^\mathrm{i} - \left(\frac{\sum w_u^{1/2} - \sum w_d^{1/2}}{\sum w_u + \sum w_d} \right)^\mathrm{o} \right\} - \mathcal{A}_\mathrm{false}. \tag{4.12}$$

An analogous replacement has to be made in the "false" asymmetry, Eq. 4.9 for the ratio $(t_\mathrm{u} - t_\mathrm{d})/(t_\mathrm{u} + t_\mathrm{d})$. The average target polarisation remains unchanged. Note that in order to cancel the different acceptances for the two target cells in Eq. 4.9 only quantities which do not change from one target polarisation to the next may be included in the weight w. Therefore w can be defined to also include P_μ. However, including the target polarisation generates an artificial "false" asymmetry even if the acceptances and target thickness for the two cells are equal.

For transverse up or downward pointing target polarisation the event yields are given by a formula similar to Eq. 4.4

$$N(\varphi) = a\Phi\hat{n}\hat{\sigma}\left\{1 - P_\mu|P_t|f\cos\varphi A_\perp\right\}. \tag{4.13}$$

involving the perpendicular asymmetry, $A_\perp$, (Eq. 2.38), and the azimuth angle, φ, between the scattering and the polarisation plane. The definition of φ accounts already for the polarisation direction and therefore only the absolute value $|P_t|$ appears in Eq. 4.13. The analysing power is proportional to $\cos\varphi$ and hence the weight becomes $w = (fd\cos\varphi)^2$. The rôle of the events from the two target cells is now played by events in the top (t) and the bottom (b) part of the detector and the counting rate asymmetry $A_N(\varphi) = (N(\varphi) - N(\pi-\varphi))/(N(\varphi) + N(\pi-\varphi))$ can be determined from each target cell separately. As for the longitudinal case the different acceptances, here for the top and bottom parts, cancel in the average of two opposite polarisations (up, down)

$$\frac{A_\perp}{d} = -\frac{1}{2P_\mu|P_t|}\left\{\left(\frac{\sum_t w_t^{1/2} - \sum_b w_b^{1/2}}{\sum_t w_t + \sum_b w_b}\right)^{\text{up}} - \left(\frac{\sum_t w_t^{1/2} - \sum_b w_b^{1/2}}{\sum_t w_t + \sum_b w_b}\right)^{\text{down}}\right\} - A^\perp_{\text{false}}, \tag{4.14}$$

where the combinations (up, t) and (down, b) include events with $-\pi/2 \le \varphi < \pi/2$, while the combinations (up, b) and (down, t) include the events with $-\pi/2 \le \pi - \varphi < \pi/2$.

The average of a kinematic variable, ξ, over all events i in an x bin is calculated using the appropriate weights, $\langle\xi\rangle = \sum_i w_i\xi_i / \sum_i w_i$.

4.1.3 Time-dependent acceptance variations

As discussed in the previous section the different acceptances for the two target cells and those for muons scattered into the upper and lower part of the spectrometer cancel in the evaluation of the parallel and perpendicular asymmetries, respectively. This assumes that the acceptance ratios, t_u/t_d, in Eq. 4.9 are the same for the two measurements combined. Note that it is not required that the acceptances themselves are stable. Because of the smallness of the counting rate asymmetries the stability of this ratio was a major concern, which triggered several upgrades in the spectrometer, discussed in Sect. 3.4. In the grouping of data sets care is taken that large efficiency changes and other changes in the apparatus and the beam did not occur.

The study of the remaining false asymmetries is based on data and starts from a detailed description of the time variations of the chamber plane efficiencies. The average plane efficiencies of some detectors along the spectrometer are shown in Fig. 4.1 as a function of time. The false asymmetry for an asymmetry obtained from two data sets, A and B, with target polarisations $P^\text{A}_\text{u,d}$ and $P^\text{B}_\text{u,d}$ is estimated by the following method. The data of one set, A, are analysed twice, once assuming the correct polarisation P^A (analysis A_A) and once assuming the polarisation after reversal, P_B, (analysis A_B). Obviously the resulting asymmetry must vanish. Now the measured changes of all plane efficiencies from measurement A to measurement B are imposed in the following way. If an efficiency decreased, hits are dropped randomly in analysis A_B, while for increasing efficiency hits are dropped in analysis A_A. An event is discarded, when after dropping of the hits the event would not have been found by the reconstruction algorithm anymore. This procedure and the whole method was crosschecked using a Monte Carlo simulation [112].

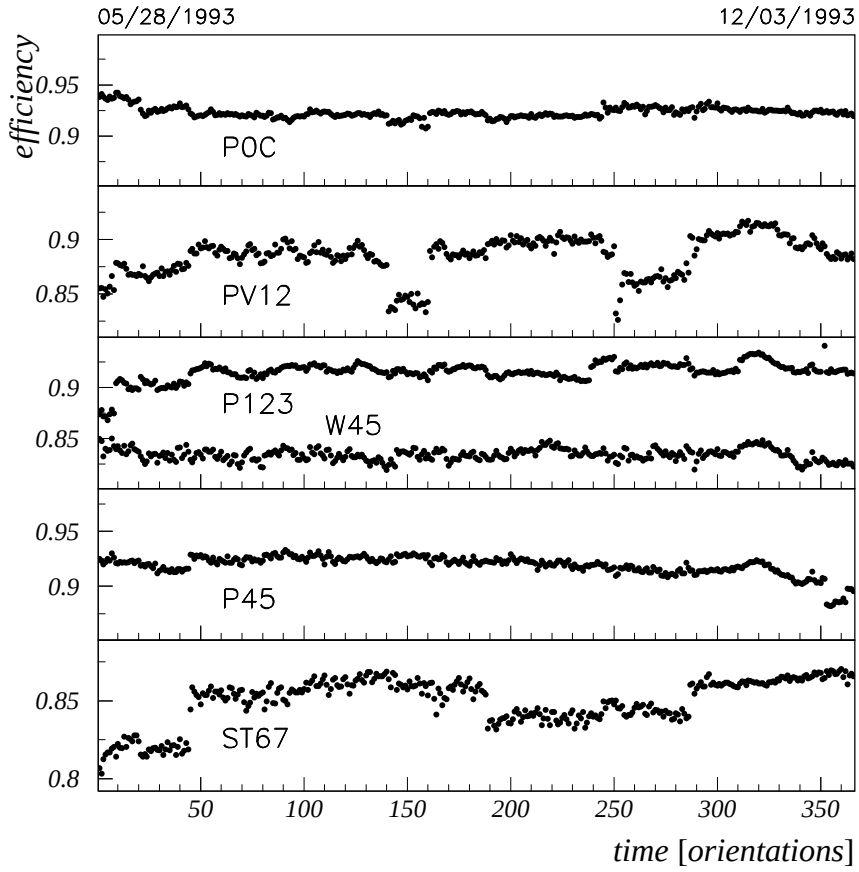

Figure 4.1: Plane efficiencies for several detectors as a function of time. Between two entries the target polarisations were inverted; from Ref. [116].

For the $\mathcal{A}_1$ measurement the false asymmetries, $\mathcal{A}_{\text{false}}$, are found to be smaller than 0.003 for both, the proton [116] and the deuteron [102]. For $A_\perp/d$ the effect of the by $\cos\varphi$ reduced analysing power is compensated by a partial cancellation of the false asymmetries in the averaged asymmetry obtained from the upstream and the downstream target cell [112]. This leads to a similar false asymmetries as in the case of $\mathcal{A}_1$.

4.1.4 The dilution due to unpolarisable nucleons

The dilution factor, f, which accounts for the unpolarisable nucleons, is defined in terms of the total differential cross sections for the different target nuclei by Eq. 4.5. Apart from the target material there are the NMR coils and the ^{3}He/^{4}He coolant in the target volume. In addition vertex smearing can cause contributions from the support structure of the target cells and the microwave stoppers. Since the materials are not distributed homogeneously over the target volume, their contribution is weighted with the distribution of interaction vertices in the plane perpendicular to the beam.

The ratios of the total differential cross sections of the proton and different nuclei to that of the deuteron, $\sigma^{\text{p}}/\sigma^{\text{d}}$ and $\sigma^A/\sigma^{\text{d}}$, were measured in several experiments studying

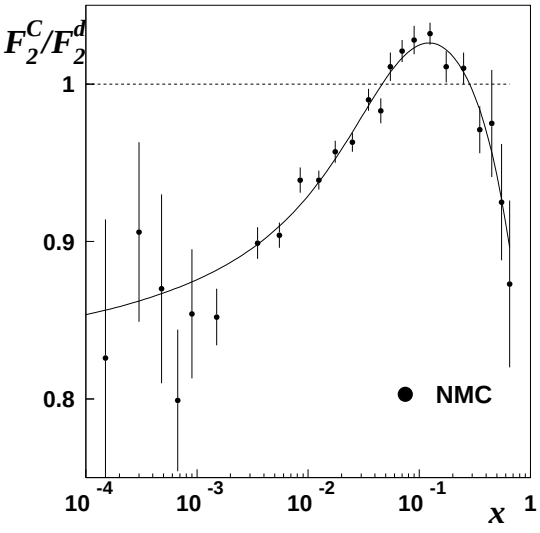

Figure 4.2: Carbon-to-deuteron structure function ratio, $F_2^{\mathrm{C}}/F_2^{\mathrm{d}}$, as a function of x.

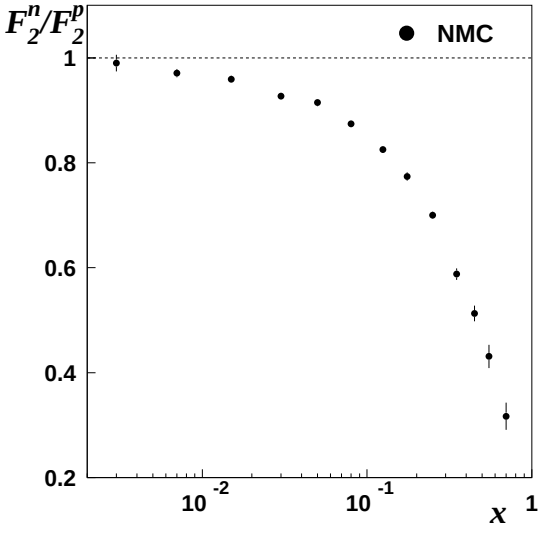

Figure 4.3: Neutron-to-proton structure function ratio, $F_2^{\mathrm{n}}/F_2^{\mathrm{p}}$, as a function of x.

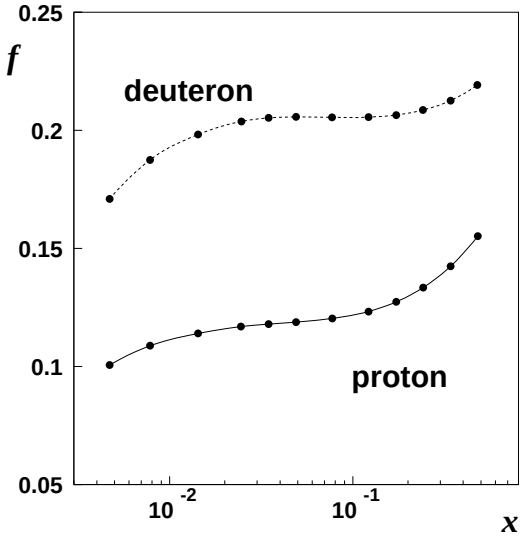

Figure 4.4: Average dilution factor, f, for the proton and deuteron target as function of x.

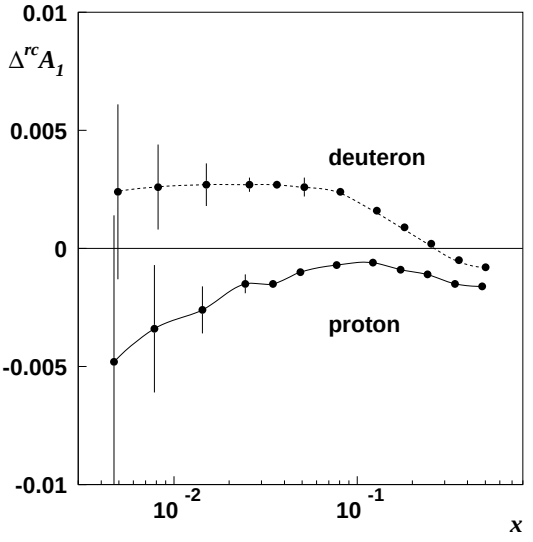

Figure 4.5: Additive radiative corrections, $\Delta^{\mathrm{rc}}\mathcal{A}_1$, for the proton and deuteron asymmetries as a function of x.

the classical EMC effect [8]. The most precise results are those from the NMC, which were obtained at about the same kinematics, and actually with the same spectrometer and beam. They are published in the form of structure function ratios, $F_2^{\rm n}/F_2^{\rm p}$ [124] and $F_2^A/F_2^{\rm d}$ for A = He, ^{6}Li, C, and Ca [125, 126]. As an example the carbon-to-deuteron structure function ratio is shown in Fig. 4.2. A significant, although small, Q^2 dependence was only observed for the ratio $F_2^{\rm n}/F_2^{\rm p}$ for which a parametrisation in x and Q^2 is available. For the other nuclei present in the target volume, ^{3}He, O, F, Na, Cr, Ni, and Cu, an A-dependent parametrisation of the structure function ratios is used based on the data from the NMC and the SLAC experiment E-139 [127].

The cross-section ratios can be recovered by using exactly the inverse procedure which led from the cross section ratios to the structure function ratios in the first place. The radiative corrections are recalculated using the same computer code, TERAD [128], and the same inputs as in Ref. [125]. Also taken out are corrections made for the difference of the proton and neutron structure functions in non-isoscalar targets

$$\frac{\sigma_{1\gamma}^A}{\sigma_{1\gamma}^{\rm d}} = \frac{F_2^A}{F_2^{\rm d}} \left(\frac{2Z}{A} + \frac{A-2Z}{A} \frac{F_2^{\rm n}}{F_2^{\rm d}} \right), \tag{4.15}$$

where the Born cross sections, $\sigma_{1\gamma}$, are defined per nucleon. The resulting average dilution factors for the proton and the deuteron are shown in Fig. 4.4. The drop at small x is due to the large number of radiative events in the high-Z nuclei and the rise at large x for the proton is due to the ratio $F_2^{\rm n}/F_2^{\rm p}$ (Fig. 4.3) which drops from about unity at $x = 0$, where the sea quarks dominate, to about 0.3 at $x = 0.8$.

4.1.5 Radiative corrections

Structure functions are defined for the one-photon-exchange process. Contributions to the cross section from higher-order electromagnetic processes must be subtracted from the experimental results. For the spin asymmetries radiative corrections come in at two places, namely for the spin-averaged cross sections in the dilution factor and for the spin-dependent cross sections in the asymmetry itself.

For the spin-averaged part the computer code TERAD is used, based on the method of Akhundov, Bardin, and Shumeiko [128]. It calculates electromagnetic corrections up to order α^4 and corrections due to the electroweak γZ interference of order αG_F and higher order electroweak processes. Corrections to the exchanged boson, to the lepton current, and to the hadron current are considered. The latter are small and are calculated in the framework of the quark parton model. The radiative corrections are largest for small x and large $y = \nu/E$, where they are dominated by the corrections to the lepton current. The emission of a photon from the incident or scattered lepton changes the kinematics at the scattering vertex. Hence an apparently deep-inelastic event can be due to elastic scattering from a nucleus, to quasi-elastic scattering from a bound nucleon, or to deep-inelastic scattering from a quark for a different kinematics. To the cross section at a point (x_0, y_0) tails from the whole kinematic region $x \geq x_0$ and $y \leq y_0$ contribute. For the same x and y the corrections are largely independent of the energy of the incident lepton.

The radiative corrections to the asymmetries are calculated with the computer code POLRAD [129], which treats the first order spin-dependent electromagnetic corrections exactly. Multiple soft-photon emission in the elastic and inelastic tails is accounted for by an exponentiation procedure. Corrections to the hadron current are not applied. Due

to the smallness of the correction there is no need to include higher-order processes. The calculation of spin-averaged and spin-dependent corrections is based on the same method. A characteristic feature is that the divergences appearing in the corrections for the inelastic tail for vanishing photon energy and those in the vertex correction are treated analytically leading to a finite result for their sum. This avoids a dependence on a cut-off parameter for the minimum photon energy. The full differential cross section, σ, can be split in a part proportional to the Born cross section, $\sigma_{1\gamma}$, and an additive part, σ_{t},

$$\sigma = a\sigma_{1\gamma} + \sigma_{\mathrm{t}}. \tag{4.16}$$

The first term accounts for the factorising part of the vertex and inelastic tail corrections and the second term for the remaining contribution from the inelastic tail and the quasi-elastic and elastic tails. The factor a is independent of the orientations of the lepton and nucleon spins. For the asymmetry, $A = \Delta\sigma/\bar{\sigma}$, we define an additive radiative correction by, $\Delta^{\mathrm{rc}}A = A - A_{(1\gamma)}$. Using Eq. 4.16 for both, $\Delta\sigma$ and $\bar{\sigma}$, we find

$$\Delta^{\mathrm{rc}}A = \frac{\bar{\sigma}_{\mathrm{t}}}{\bar{\sigma}}\left(\frac{\Delta\sigma_{\mathrm{t}}}{\bar{\sigma}_{\mathrm{t}}} - A_{(1\gamma)}\right). \tag{4.17}$$

The factorising part cancels in the correction for the asymmetry and the correction from the tails vanishs if the tail asymmetry, $\Delta\sigma_{\mathrm{t}}/\bar{\sigma}_{\mathrm{t}}$, is identical to that of the one-photon events. To compute the tails of the inelatic cross section the structure functions g_1 and g_2 are needed as input in addition to the spin-averaged structure functions F_2 and R. For the correction to $\mathcal{A}_1$ a parametrisation of the available g_1 data was used and the contribution of g_2 was neglected. The correction $\Delta^{\mathrm{rc}}\mathcal{A}_1$ is shown for the proton and the deuteron in Fig. 4.5 and does not exceed 0.005 in the full x range, when the standard cut $y < 0.9$ is applied. For $A_\perp$ it was assumed that $g_2 = g_2^{\mathrm{ww}}$ as defined in Eq. 2.117. The corrections found are much smaller than the statistical error of $A_\perp$ and were neglected.

Radiative events do not contribute to the statistical accuracy of the one-gamma asymmetry. In the first x bin with $\langle x\rangle = 0.005$ the contribution from the tails accounts for 90 % of the total spin-averaged correction. The correction amounts to $\sigma_{\mathrm{t}}/\sigma_{1\gamma} = 0.17$ for the inelastic tail and to 0.27 (0.14) for the elastic tail for the proton (deuteron, including the quasi-elastic tail). In the calculation of the statistical error the radiative events are treated as background, which carries no information on the asymmetry. This is correct for the elastic tails, but the asymmetry of the tail from the inelastic cross section at a point (x, y) is correlated with that of the one-gamma cross section at a point close in x and y. Therefore this procedure might lead to a slight overestimate of the statistical error.

4.2 Results

The results presented here are preliminary and represent the status of the analysis as shown at the *"Rencontres de Moriond"* meeting in Les Arcs, France, in March 1996 [130]. In addition to the proton data taken in 1993 [19, 20] and the deuteron data taken in 1992/94 [18, 21] the 1995 deuteron data are included in the analysis. With respect to the published results data from an additional small-x trigger were added for the proton and the stability cuts for the proton and 1992 deuteron data were tightened. The calculation of the statistical error was modified to account for the background from the elastic radiative tails. The previous method led to an underestimate of the statistical error in the first x

Table 4.1: Kinematic cuts applied in the analysis.

Kinematic variable	Data taken at muon energies of 100 GeV	190 GeV
p_μ	≥ 15 GeV	≥ 19 GeV
ν	≥ 10 GeV	≥ 15 GeV
ϑ	≥ 13 mrad	≥ 7 mrad
y	≤ 0.9	≤ 0.9

bin of about 30 % for the proton. The publication of the refined analysis of the proton data [123] and the analysis of all deuteron data [131] is in preparation.

The semi-inclusive results [22] do not yet include the 1995 deuteron data. The radiative corrections are smaller for this class of events because the elastic tail does not contribute. Therefore the statistical error of these data is at most underestimated by 15 % in the first x bin.

Cuts on kinematic variables were applied in the analysis to reduce the background from muons originating from hadron decays (p_μ), kinematical smearing (ν), vertex smearing (ϑ), and the size of radiative corrections (y). In addition to the cuts summarised in Table 4.1 a cut of $Q^2 \geq 1$ GeV^2 was applied unless stated otherwise.

The comparison with other experiments and a discussion of the physics implications is deferred to Chapter 5.

4.2.1 Virtual-photon asymmetries

The results for the proton and the deuteron asymmetries are shown in Fig. 4.6 and are summarised in Table 4.2. The data cover for $Q^2 > 1$ GeV^2 the range $0.003 \leq x \leq 0.7$.

The systematic error comprises the uncertainties of the beam and target polarisations, of the dilution factor, of the radiative corrections, and of the cross section ratio R (Eq. 2.36) as well as contributions due to the time variation of the apparatus' acceptance and the neglect of A_2. For the upper limit of A_2 we used our measurements and at high x, where it is more stringent, the limit $\sqrt{R}$ (Eq. 2.41). At small x the uncertainty of the radiative corrections dominates the systematic error. The uncertainties arising from the beam and target polarisations and the dilution factor are proportional to the asymmetry and dominate at large x. They are more important for the larger proton asymmetry than for the smaller deuteron asymmetry.

The proton data were also analysed for $Q^2 < 1$ GeV^2. With the lowered cut one gains three additional bins in the range $0.0008 \leq x < 0.003$ with average Q^2 of 0.29, 0.45, and 0.70 GeV^2. Some low-Q^2 data also enter the bins in the range $0.003 \leq x < 0.01$. Special care went into the study of vertex smearing corrections and the contamination by events from muon-electron scattering [118], which appears at $x = 0.00054$. The contamination in the first bin $0.0008 \leq x < 0.0012$ was estimated to (5 ± 1) %. The resulting asymmetries in the three additional small-x bins are compatible with zero and are shown in Fig. 4.7. These low-Q^2 data are not used in the further analysis of the structure functions and their moments.

The A_2 data are obtained using Eq. 2.45 (p. 10) from the measured transverse asym-

Table 4.2: The asymmetry A_1 and its statistical and systematic errors for the proton and the deuteron.

		Proton				Deuteron			
x range	$\langle x \rangle$	$\langle Q^2 \rangle$	A_1			$\langle Q^2 \rangle$	A_1		
0.003–0.006	0.005	1.3	0.068	(39)	(8)	1.3	0.001	(20)	(4)
0.006–0.010	0.008	2.1	0.050	(35)	(5)	2.1	−0.010	(18)	(4)
0.010–0.020	0.014	3.6	0.056	(30)	(5)	3.5	−0.025	(15)	(4)
0.020–0.030	0.025	5.9	0.057	(41)	(4)	5.7	0.000	(20)	(3)
0.030–0.040	0.035	8.0	0.043	(50)	(3)	7.7	−0.013	(25)	(3)
0.040–0.060	0.049	10.7	0.105	(43)	(7)	10.4	0.061	(21)	(5)
0.060–0.100	0.077	15.4	0.176	(42)	(12)	14.8	0.020	(21)	(3)
0.100–0.150	0.122	21.9	0.275	(55)	(17)	21.1	0.074	(29)	(6)
0.150–0.200	0.172	28.3	0.265	(77)	(17)	27.3	0.178	(41)	(13)
0.200–0.300	0.241	36.0	0.242	(79)	(16)	34.7	0.229	(43)	(16)
0.300–0.400	0.342	45.9	0.490	(130)	(35)	44.3	0.186	(75)	(14)
0.400–0.700	0.481	57.2	0.532	(171)	(46)	54.9	0.343	(103)	(26)

Table 4.3: The structure function $g_1(x, Q^2)$ and its statistical and systematic errors for the proton and the deuteron. For the $\langle Q^2 \rangle$ values see Table 4.2.

		Proton			Deuteron		
x range	$\langle x \rangle$	$g_1(x, Q^2)$			$g_1(x, Q^2)$		
0.003–0.006	0.005	1.637	(937)	(189)	0.027	(476)	(107)
0.006–0.010	0.008	0.827	(584)	(93)	−0.162	(292)	(62)
0.010–0.020	0.014	0.583	(310)	(47)	−0.256	(151)	(38)
0.020–0.030	0.025	0.384	(273)	(27)	−0.001	(131)	(18)
0.030–0.040	0.035	0.213	(249)	(15)	−0.061	(119)	(14)
0.040–0.060	0.049	0.384	(156)	(22)	0.213	(74)	(16)
0.060–0.100	0.077	0.410	(98)	(22)	0.043	(46)	(6)
0.100–0.150	0.122	0.393	(79)	(21)	0.096	(37)	(7)
0.150–0.200	0.172	0.251	(74)	(14)	0.147	(34)	(9)
0.200–0.300	0.241	0.143	(47)	(8)	0.114	(22)	(7)
0.300–0.400	0.341	0.152	(40)	(9)	0.046	(18)	(3)
0.400–0.700	0.478	0.061	(20)	(4)	0.031	(9)	(2)

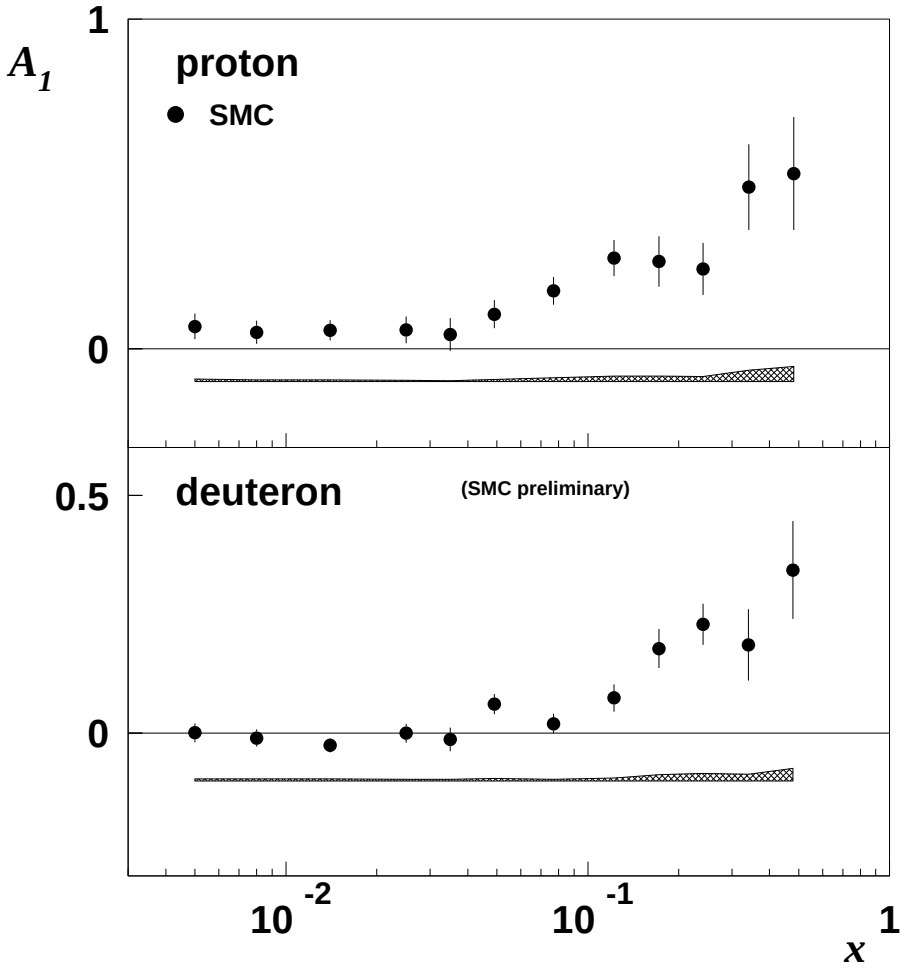

Figure 4.6: The virtual-photon asymmetry A_1 for the proton (top) and the deuteron (bottom) as a function of x.

metries, $A_\perp$, and a parametrisation of the available $A_{\|}/D$ data. For the averaging over Q^2 in a given x bin we assumed that $\sqrt{Q^2}A_2$ scales instead of A_2. Such behaviour follows from Eq. 2.42 and scaling of g_1 and g_2. The total systematic error of $A_2(x)$ is much smaller than the statistical one. The proton [20] and deuteron data [132] were taken at 100 GeV and 190 GeV incident muon energy, respectively. The results are shown and discussed in Sect. 5.3.1.

4.2.2 Structure functions and first moments

From the asymmetries, A_1, the structure function, g_1, is determined using Eq. 2.49 and again neglecting a possible contribution from A_2. For the spin-averaged structure functions $F_2(x, Q^2)$ and $R(x, Q^2)$ we use the parametrisations by the NMC [133] and by SLAC [134], respectively. The uncertainty of R cancels in g_1 if the same parametrisation of R is used as in the extraction of F_2 from the measured unpolarised cross sections and if the kinematics

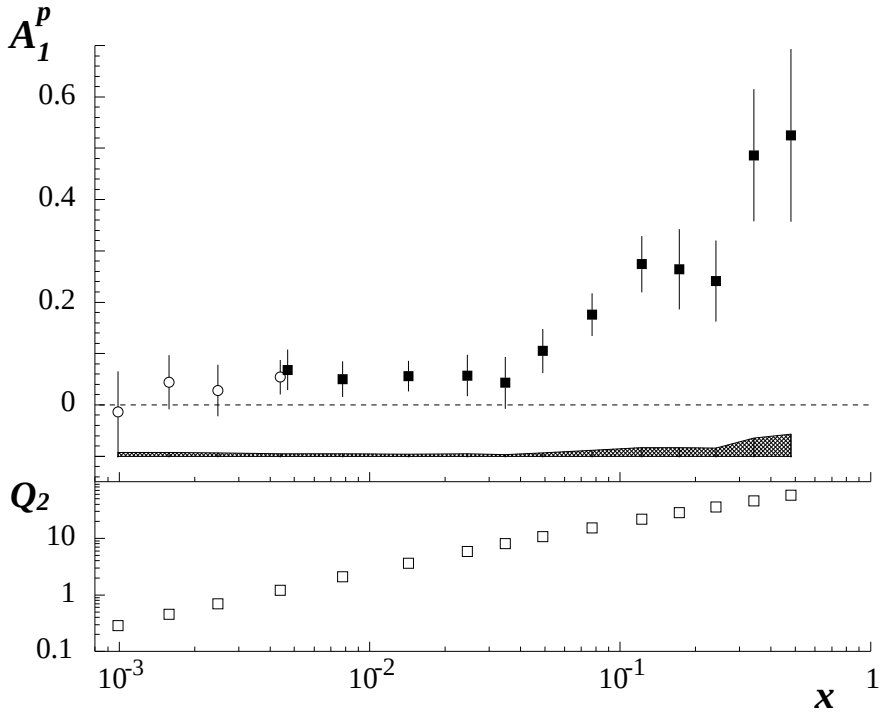

Figure 4.7: The virtual-photon asymmetry A_1 of the proton as a function of x. The points shown as open circles include data in the range $0.2 < Q^2 < 1$ GeV^2.

is the same. This is largely the case since F_2 was measured by the NMC with the same spectrometer and muon beam and the same parametrisation of R was used. The results for g_1 of the proton and the deuteron are shown in Fig. 4.8 and listed in Table 4.3. Also shown are the neutron data obtained by combining our the proton and neutron results.

For the evaluation of the first moments we choose $Q_0^2 = 10$ GeV^2 which represents a typical value for the data sets. Experimentally no Q^2 dependence of the asymmetry data is found (Sect. 5.2.2). From the theoretical considerations discussed in Sect. 2.9 we choose to assume scaling of g_1/F_1 rather than of A_1. For the measured region $0.003 \leq x \leq 0.7$ we obtain the integrals

$$\begin{aligned} \int_{0.003}^{0.7} g_1(x, Q_0^2) &= 0.130 \pm 0.014 \pm 0.009 \qquad \text{(proton)} \\ \int_{0.003}^{0.7} g_1(x, Q_0^2) &= 0.038 \pm 0.007 \pm 0.004 \qquad \text{(deuteron).} \end{aligned}$$

The extrapolation to $x = 0$ is performed using the average of the first two small-x data points. Such a form is motivated by Regge theory. This yields for the range $0 \leq x < 0.003$ a contribution of 0.004 ± 0.002 for the proton and of 0 ± 0.001 for the deuteron. The extrapolations to $x = 1$ make use of the limit $|A_1| \leq 1$. Finally we obtain the first moments at $Q_0^2 = 10$ GeV^2 assuming scaling of g_1/F_1

$$\int_0^1 g_1(x, Q_0^2) = 0.137 \pm 0.014 \pm 0.010 \qquad \text{(proton)}$$

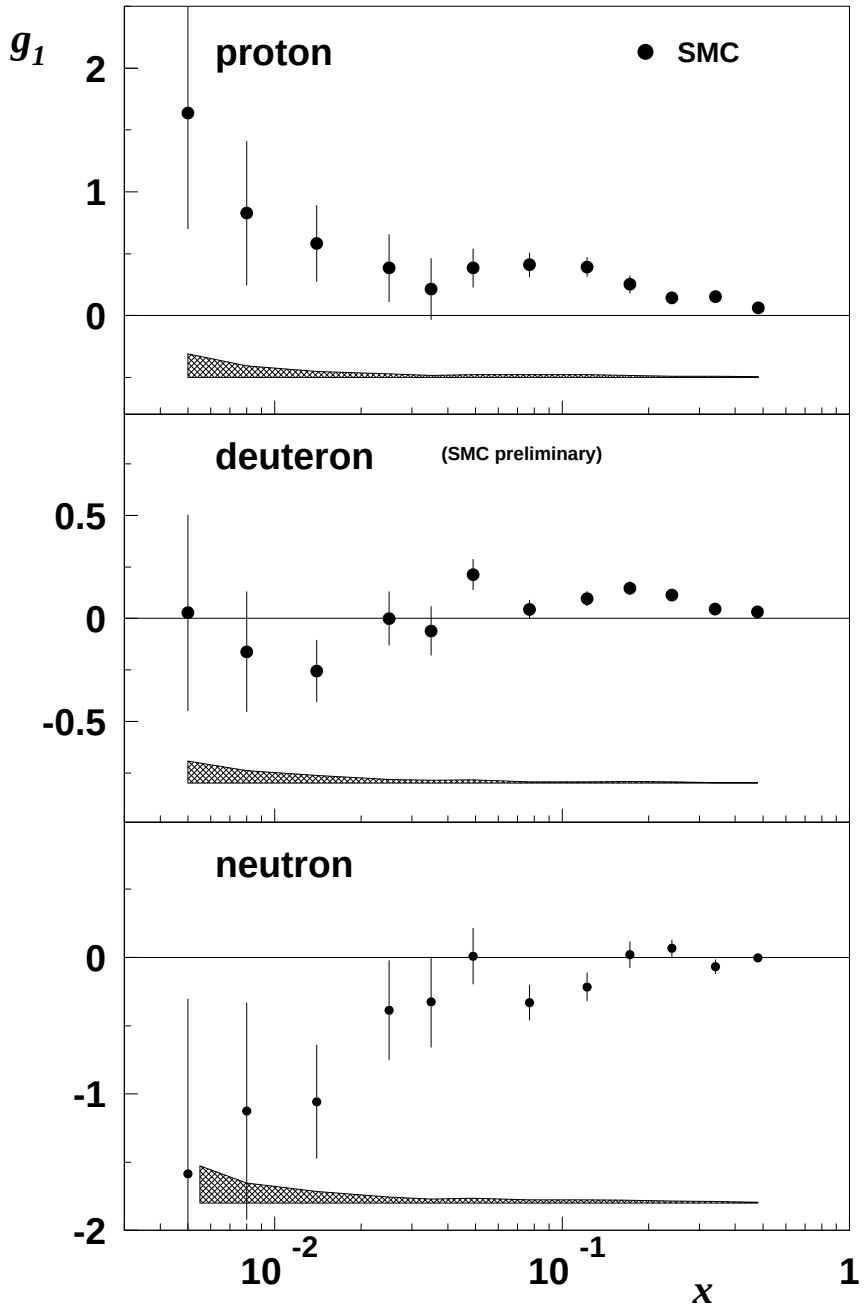

Figure 4.8: The structure function $g_1(x, Q^2)$ for the proton (top) and the deuteron (middle) and the neutron (bottom) as a function of x. The neutron data are derived from proton and deuteron data.

Table 4.4: Contributions to the error of Γ_1.

Source	Contribution	
	proton	deuteron
Extrapolation at low x	0.0038	0.0009
Beam polarisation	0.0037	0.0015
Target polarisation	0.0035	0.0013
Dilution factor	0.0032	0.0006
Uncertainty of F_2	0.0029	0.0012
Acceptance variation	0.0020	0.0014
Momentum measurement	0.0014	0.0014
Radiative corrections	0.0013	0.0008
Kinematic resolution	0.0010	0.0010
Extrapolation at high x	0.0008	0.0009
Proton background	–	0.0006
Neglect of A_2	0.0004	0.0005
Total systematic error	0.0100	0.0050
Statistical error	0.0140	0.0070

$$\int_0^1 g_1(x, Q_0^2) \quad = \quad 0.038 \pm 0.007 \pm 0.005 \qquad \text{(deuteron)}.$$

The contribution of the different sources to the systematic errors of the first moments is detailed in Table 4.4. Both, the proton and the deuteron results violate the Ellis–Jaffe sum rule, which predicts 0.170 ± 0.005 and 0.071 ± 0.04, respectively.

From these results we find for the Bjorken sum rule

$$\Gamma_1^{\mathrm{p}} - \Gamma_1^{\mathrm{n}} = 0.191 \pm 0.036 \qquad (Q^2 = 10 \text{ GeV}^2),$$

which is in excellent agreement with the theoretical prediction of 0.0187 ± 0.003. For the spin content and the strange-sea polarisation we find from the combined proton and deuteron data

$$\Delta\Sigma_{\mathrm{inv}} = 0.25 \pm 0.06 \qquad \Delta s = 0.11 \pm 0.02,$$

confirming the EMC result that the quark spins contribute little to the nucleon's spin in the quark parton model.

4.2.3 Semi-inclusive data

The fragmentation of the struck quark into hadrons, in which it is contained as valence quark is favoured. Thus positive pions tag up quarks and down antiquarks. Using in addition proton and deuteron targets a complete up-down spin-flavour decomposition of the nucleon structure is in principle possible. This information is exploited in the semi-inclusive analysis of the 1992/94 deuteron data and the 1993 proton data [22]. To discriminate between electrons and hadrons the information from the H2 calorimeter [110] is used. Its electromagnetic part corresponds to 20 radiation lengths and entirely contains electromagnetic showers. The total thickness of the electromagnetic and hadronic sections of the calorimeter amounts to 5.5 nuclear interaction lengths. Electrons are rejected by a cut on the ratio of the energy deposited in the electromagnetic part to the total deposited

energy. An identification of pions, kaons, and protons is not attempted. In addition to the standard kinematic cuts listed in Table 4.1 an energy fraction of $z \geq 0.2$ is required in the analysis. This leaves us with 1.4×10^6 and 1.6×10^6 charged hadrons for the two deuteron data sets and with 1.2×10^6 for the proton data set. The evaluation of the asymmetries for positive and negative hadrons, $A_1^{\pm}$, proceeds in principle like in the inclusive case, however separately for events with positive and negative hadrons. The effect of secondary interactions in the thick target on the asymmetries was studied and found to be negligible. The results are shown and discussed in Sect. 5.7. It is found that the polarisation of the up valence quarks is positive and that of the down valence quarks is negative. The light-quark sea is not strongly polarised.

Chapter 5

Present status of spin structure functions

From the SMC and E-143 experiments a clear picture has emerged. The Ellis–Jaffe sum rules are violated for both, the proton and the deuteron and the Bjorken sum rule is satisfied. The fraction of the nucleon's spin carried by the quark spins thus remains small. In this chapter we review the experimental data as well as some of the recent theoretical developments. In particular lattice gauge theory has become a very useful tool in the understanding of the nucleon's spin structure. Progress has also been made concerning g_2 and higher-twist contributions.

5.1 Other recent spin-structure-function experiments

Apart from the SMC experiments, which are described in detail in Chapter 3 and are summarised in Table 3.2 (p. 40), the SLAC experiments provided new data on g_1 and g_2. Recently, preliminary data on the neutron structure function, g_1^n, were reported from the HERMES experiment at DESY which started data taking in 1995.

The three experiments are complementary in several respects. In particular in the incident lepton energy, E, and thus in the x range covered for $Q^2 > 1$ GeV^2 and in the average Q^2 of the data:

experiment		beam	E/GeV	Q^2/GeV^2	x range
EMC p	CERN	μ	200	10.7	$0.01 \leq x \leq 0.7$
SMC	CERN	μ	190	10	$0.003 \leq x \leq 0.7$
SLAC		e	29	3	$0.03 \leq x \leq 0.8$
HERMES	DESY	e	27	3	$0.03 \leq x \leq 0.8$

The main domains of the experiments are:

- The SMC experiment is unique in covering high Q^2 and small x. The small-x region is decisive for the extrapolation of $g_1(x)$ to $x = 0$ in the evaluation of the Bjorken and Ellis–Jaffe sums and for determining the polarised gluon distribution function, Δg, in the QCD analyses of the g_1 data. The statistical precision of the SMC data is moderate, while the systematic error is similar to that of the SLAC data. The statistical error of the first moments is presently slightly larger than

the systematic error, which dominates for the SLAC data. In the SMC experiment produced hadrons are also detected.

- The SLAC experiments are unique concerning their high luminosity. They provide data with a high statistical precision at a lower value of Q^2 for $x \geq 0.03$. The E-154 and E-155 experiments will extend the x range to $x \geq 0.01$ and increase average value of Q^2 to about 5 GeV^2. In addition to the experiments with proton and deuteron targets, experiments performed with a ^{3}He target provide an alternative and in principle more direct determination of the neutron structure function, g_1^n.

- The HERMES experiment is unique in the combination of particle identification and high luminosity. The internal gas target makes it possible to use pure proton and deuteron targets without a dilution due to other nuclei in the target material. The experiment cannot extend the kinematic range covered by the present SLAC experiments, but will provide high precision semi-inclusive data.

The kinematic domains covered by the SMC and E-143 experiments are shown in Fig. 5.1. The kinematic range of the HERMES experiment is similar to that of the E-143 experiment but also covers the gap caused by the two spectrometer arms. This gap is also covered by E-143 data taken at lower incident electron energies.

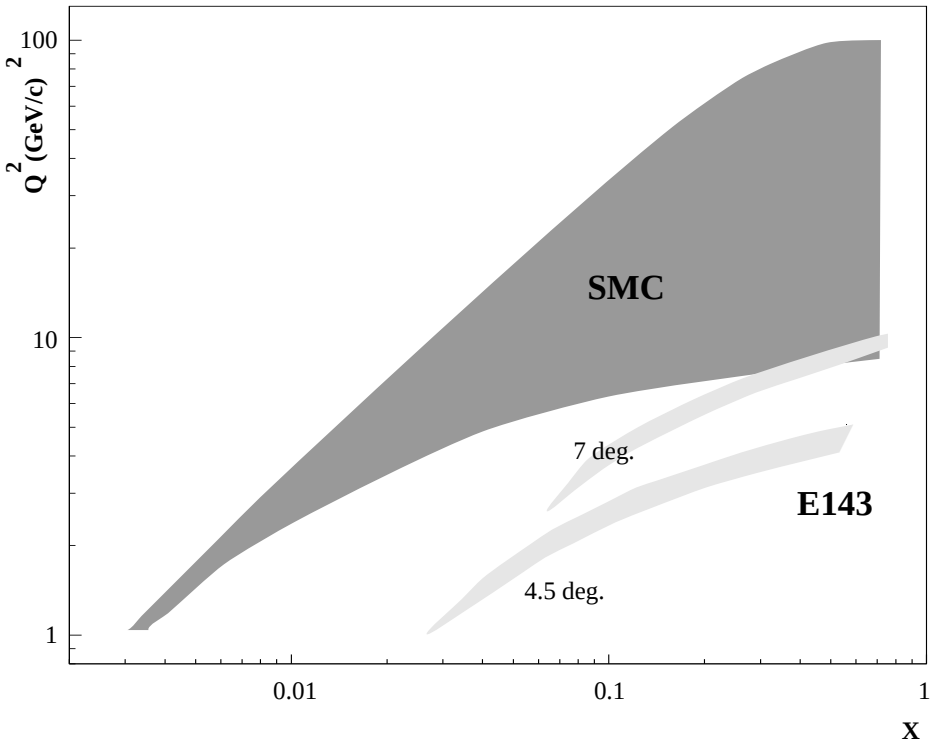

Figure 5.1: Kinematic domains covered by the SMC and E-143 experiments.

Table 5.1: Recent and future SLAC and HERMES experiments.

Year	Experiment	Beam		Target	
		Energy GeV	Polarisation %	Material	Polarisation %
1992	E-142 [23]	25.5	39	^{3}He	30–40
1993	E-143 [24]	29.1	84	$^{15}NH_3$	65–80
	[25]			$^{15}ND_3$	25
1995	E-154	48.3	82	^{3}He	38
1997	E-155	48.3	≈ 80	$^{15}NH_3$	≈ 75
				^{6}LiD	≈ 30
1995	HERMES [135]	27	≈ 50	^{3}He	≈ 50
1996–	HERMES	27	≈ 50	H, D	≈ 90

5.1.1 The SLAC experiments

The recent and future SLAC experiments on polarised structure functions are summarised in Table 5.1. Between the 1992 and 1993 experiments the polarised electron source was largely improved. While in 1992 photo-emission from a AlGaAs photocathode provided an average beam polarisation of 39 %, in 1993 polarisations in excess of 80 % were reached with strained-lattice GaAs photocathodes. The beam operated with a pulse width of 2 μs (1 μs for E-142) and a repetition rate of 120 Hz. The longitudinal beam polarisation was varied randomly on a pulse-by-pulse basis and measured by Møller scattering from thin ferromagnetic foils. In the E-142 experiment a single arm polarimeter was used, yielding a precision of $\Delta P/P = 0.04$. For the E-143 experiment an additional double arm polarimeter was installed, which measured the beam polarisation with a precision of $\Delta P/P = 0.025$. Incident electron energies of 19.4, 22.7, and 25.5 GeV (9.7, 16.2, 29.1 GeV) were used in the E-142 (E-143) experiments.

The ^{3}He target gas in the E-142 experiment was contained in a 30 cm long glass cell with 0.1 mm thick entrance and exit windows sitting in a 30 G holding field. The target [136] was operated at 8.6 bar and 0 °C temperature resulting in a density of 2.3×10^{20} atoms/cm^3. The helium gas was polarised in a separate chamber by spin-exchange collisions with rubidium vapour at 65 °C, which was optically pumped by a 20 W CW laser system. The polarisation was measured in the scattering chamber by an NMR system with a precision of $\Delta P/P = 0.07$ and ranged from 30 % to 40 %. Beam intensities of (0.5–2.0) $\times 10^{11}$ electrons were used with this target.

The ^{15}N-ammonia targets of the E-143 experiment make use the same principle as applied in the SMC target (Sect. 3.3). The 3 cm long, 2.5 diameter solid-state targets were polarised by microwave irradiation using the mechanism of dynamic nuclear polarisation in a 4.8 T magnetic field. The targets were cooled to 1 K by a ^{4}He evaporation refrigerator. Proton polarisations of 65–80 % were reached within 10–20 min, which then decayed slowly to about 50 % over 8–12 h due to radiation damage. The average deuteron polarisation was 25 % with a maximum of greater than 40 %. After having taken data with both targets, which are stacked on top of each other, they were annealed at 80 K and repolarised. To minimise the radiation damage the electron beam was rastered over the target cross

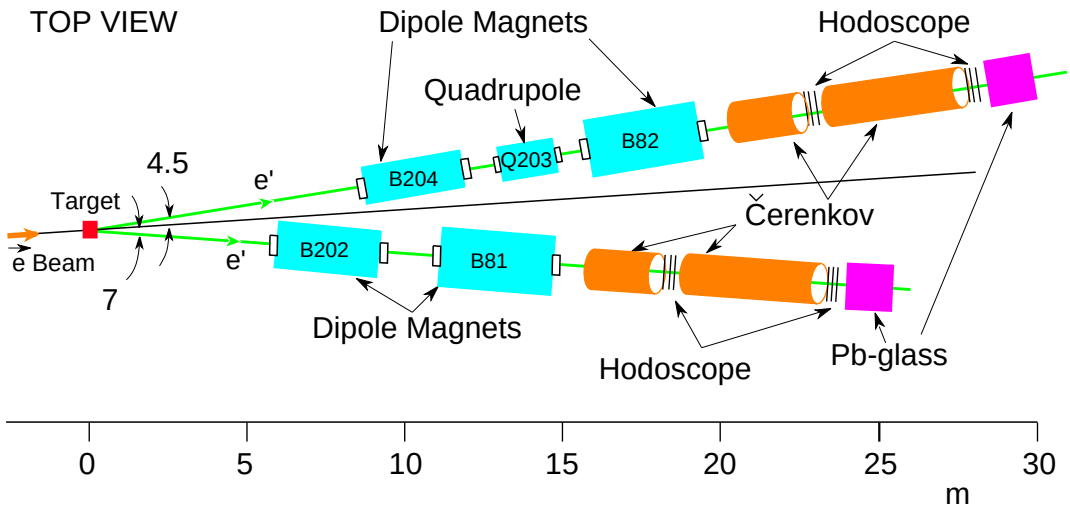

Figure 5.2: Layout of the spectrometers used in the SLAC experiments E-142 and E-143.

section of 4.9 cm^2. The polarisation was measured using NMR coils embedded in the target material and applying a similar technique as in the SMC target. The accuracy of the measurements were $\Delta P/P = 0.025$ and 0.04 for the proton and deuteron targets, respectively. The data have to be corrected for the nitrogen polarisation. The isotope ^{15}N was chosen because of its spin $\frac{1}{2}$ which yields a narrow proton-like NMR signal. The signal from the spin-1 ^{14}N nucleus is very broad and difficult to measure. For the solid targets beam intensities of (2–4) $\times 10^9$ electrons per pulse were used.

The momentum of the scattered electron was analysed in the range 6–25 GeV/c using two independent magnetic spectrometers [137] positioned under angles of 4.5° and 7.0° with respect to the incident beam (Fig. 5.2). The solid angles covered were 0.097 msr and 0.435 msr, respectively. To reject pions the detector system of each spectrometer comprised two gas Cherenkov counters operated at pion thresholds of 9 GeV/c and 13 GeV/c. Hodoscopes between and after the Cherenkov counters tracked the scattered electron. Its energy was measured in a lead-glass array at the end of the setup. The momentum resolution was better than 2.5 % in the full range of acceptance. For the E-154 and E-155 experiments the spectrometers are placed at 2.75° and 4.5°, respectively.

An additional 10° spectrometer will be installed for the E-155 experiment scheduled for 1997. In this experiment also a new target material, ^{6}LiD, will be employed. The spin-1 ^{6}Li nucleus can be understood as composed of an alpha particle and a deuteron (or proton and neutron) [138] resulting in a very advantageous dilution factor of 0.5, see also Sect. 6.1.

5.1.2 The HERMES experiment at DESY

The HERMES experiment [28] at DESY uses an internal gas target in the 27 GeV electron ring of HERA. The main advantage of this technique is that the asymmetry is not diluted by additional unpolarised materials as in the case of solid targets. A comprehensive description of the design and performance can be found in Ref. [139]. The experiment can

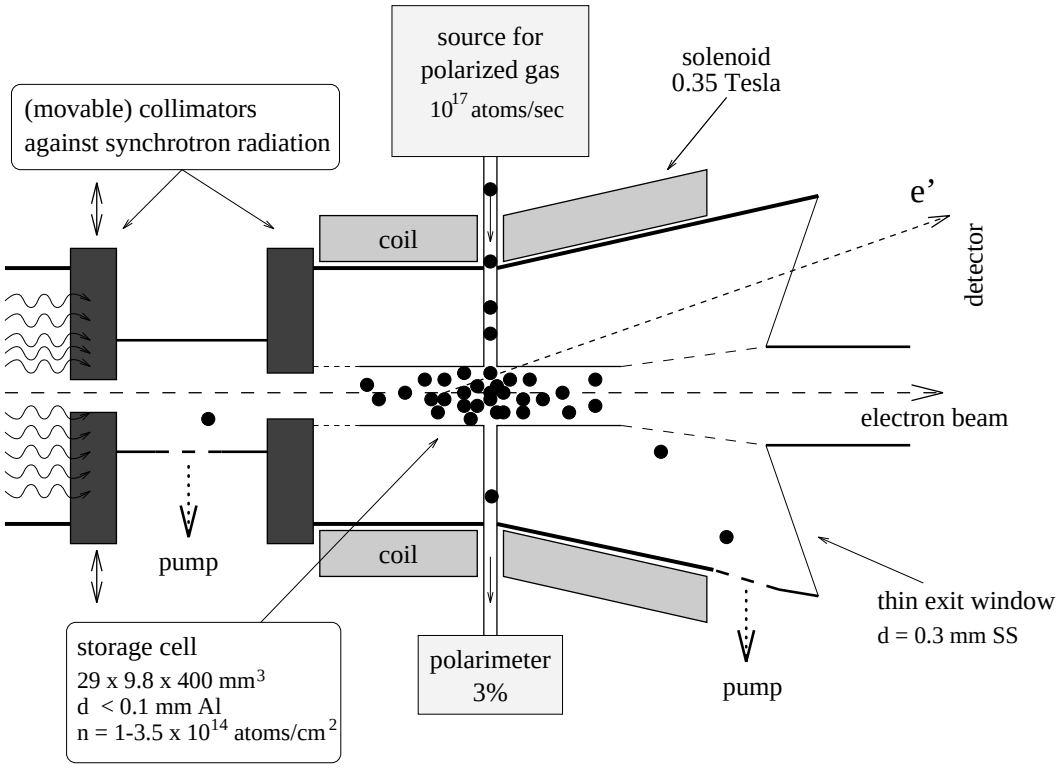

Figure 5.3: Layout of the HERMES internal gas target.

run simultaneously with the H1 and ZEUS experiments. Results from the first run in 1995 with unpolarised protons and deuterons and polarised ^{3}He were presented in the DIS'96 conference in Rome [135]. For 1996 experiments with polarised protons and deuterons are scheduled and further measurements are planned for the following years.

Electrons in storage rings slowly acquire a transverse polarisation due to an asymmetry in the spin-flip amplitudes for synchrotron radiation as predicted by Sokolov and Ternov [140]. Spin rotators were installed before and after the HERMES detector to obtain longitudinal electron polarisation. With spin matching and fine tuning against depolarising resonances maximum longitudinal polarisations of about 60 % were achieved in May 1994 [141]. The polarisation rise time is about 20 minutes. The transverse beam polarisation is measured by Compton back scattering of circularly polarised laser light from the electron beam with a precision of presently $\Delta P/P = 0.1$.

The polarised target gas is contained in a 40 cm long windowless open storage cell as shown in Fig. 5.3. It is fed with up to 10^{17} atoms/s from a polarised gas source. The gas density in the cell ranges from 10^{14} atoms/cm^2 for hydrogen and deuterium at 100 K to 3.5×10^{14} atoms/cm^2 for ^{3}He at 20 K. The gas is pumped away on both ends of the storage cell. Magnetic fields of 0.35 T and 0.15 T hold the longitudinal and transverse polarisations, respectively. For the ^{3}He a holding field in the order of 1 mT is sufficient. The polarised hydrogen and deuterium is delivered by an atomic beam source [142] with typical polarisations of 90 %. The polarisation can be changed within milliseconds by a change of the radio frequency. It is measured in a Breit–Rabi apparatus

on gas samples extracted from the target cell. The anticipated precision is $\Delta P/P = 0.03$. The ^{3}He is provided by a laser driven polarised source [143], which presently reaches 50 % polarisation. It takes about 20 s after changing the polarisation of the laser light before equilibrium is reached in the pumping cell, where the polarisation is measured using the polarisation of the light emitted by the ^{3}He atoms. The polarisation in the storage cell can be measured with moderate precision by the so-called target optical monitor, which analyses the polarisation of the light emitted by the ^{3}He atoms in the storage cell.

The scattered electron (or positron) is analysed in an open forward spectrometer, which accepts scattering angles greater than 40 mrad. The spectrometer magnet provides a bending power of 1.3 Tm. Micro-strip gas chambers close to the target and drift chambers upstream and downstream of the spectrometer magnet determine the interaction point, the scattering angle, and the momentum of the scattered electron. Inside the magnet proportional chambers are installed to improve the pattern recognition. Particle identification is performed by combining the information from a transition-radiation detector, a threshold Cherenkov counter, a preshower counter, and a lead-glass calorimeter. Pion-kaon separation is possible below 15.8 GeV/c.

5.2 Cross-section asymmetry data

5.2.1 The longitudinal asymmetry A_1

In Figure 5.4 all available proton, deuteron, and neutron data for the virtual-photon asymmetry, A_1, with $Q^2 > 1$ GeV^2 are shown. For the proton they comprise those from the pioneering YALE–SLAC experiments E-80 and E-130 [11,12], from the CERN muon experiments of the EMC [9,17] and the SMC [19], and from the SLAC experiment E-143 [24]. For the E-143 proton data g_1/F_1 is shown as published instead of A_1, see Eq. 2.46. For the kinematics of the SLAC experiments the two quantities differ considerably only at large x, while for the SMC data their difference never exceeds 1.4 %. For the deuteron presently only data from the SMC [21] and E-143 [25] experiments and for the neutron only those from the E-142 experiment [23] are available. For the deuteron and for the neutron A_1 is shown. The SMC data contain the preliminary 1995 data set as shown in Moriond [130]. The previously observed trend of the deuteron asymmetry to be negative [21] is less pronounced when the new data set is included.

In the evaluation of A_1 from the measured cross-section asymmetry, $A_{\parallel} = D(A_1 + \eta A_2)$, (Eq. 2.45) the contribution from A_2 was neglected in the EMC and SMC analyses, while in the E-142 and E-143 analyses the A_2 data measured in these experiments were used. The contribution of A_2 is suppressed by the kinematical factor η which is small in the kinematic region of EMC and SMC experiments. In addition the measurements of A_2 itself are compatible with zero for $x < 0.2$, see Sect. 5.3.1. The neglect of A_2 is accounted for in the systematic uncertainties of the SMC and EMC data.

The agreement of the data sets is excellent, although the average Q^2 of the SMC and EMC data in a given x bin is about seven times larger than that of the E-143 data in the same bin. Above $x > 0.03$, which is the lower x limit of the E-143 data, no significant Q^2 dependence of A_1 is seen. For smaller x, where only the SMC data exist, no appreciable range in Q^2 is covered. A considerable Q^2 dependence of A_1 in this region cannot be excluded, see Sect. 5.2.2.

The present discussion focuses on the behaviour of the asymmetries and of the structure

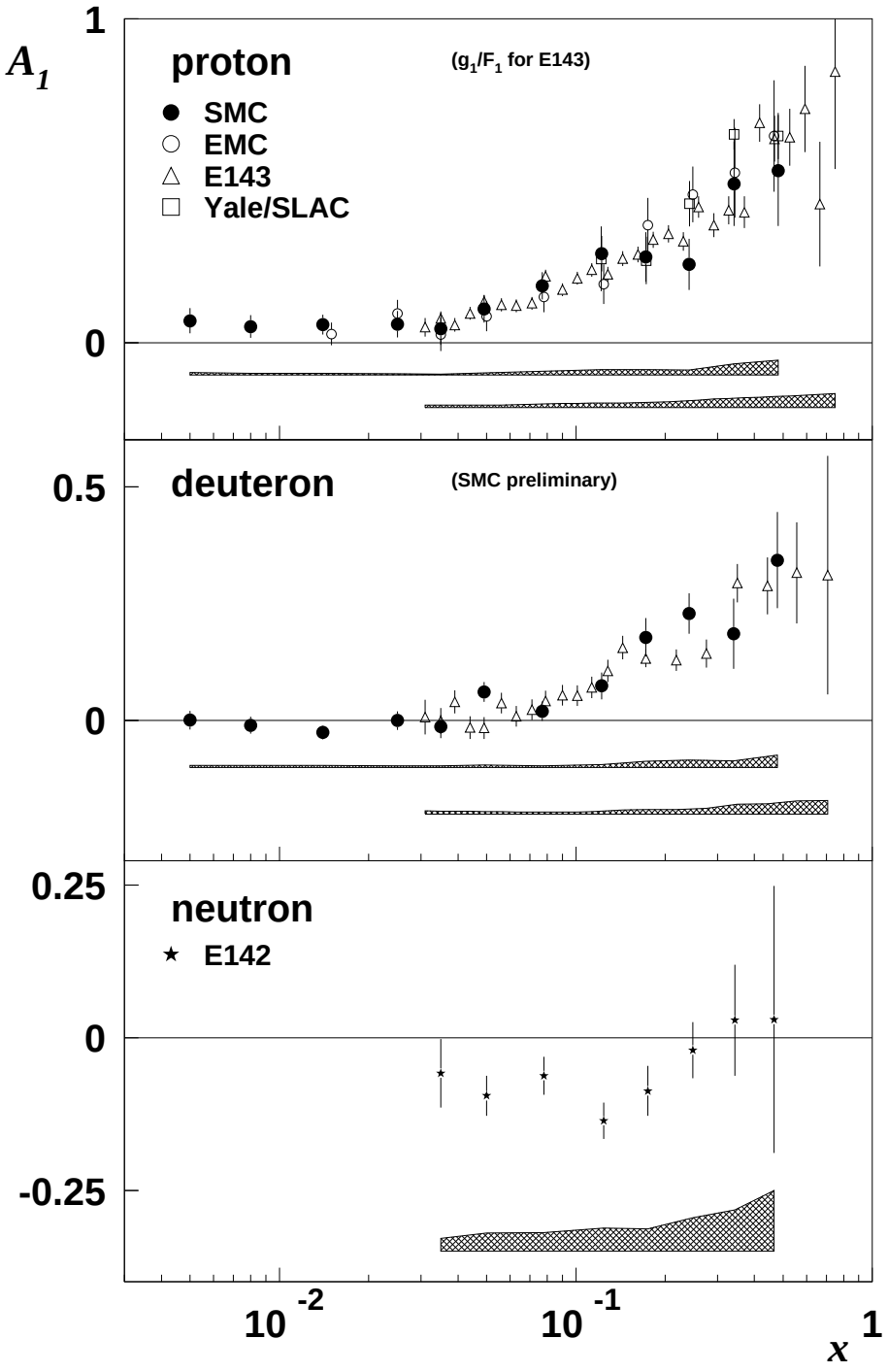

Figure 5.4: Virtual-photon asymmetry, A_1, for the proton (top), the deuteron (middle), and the neutron (bottom) as a function of x. For the E-143 proton data g_1/F_1 is shown instead of A_1. The shaded bands indicate the systematic errors of the SMC, E-143, and E-142 data, respectively.

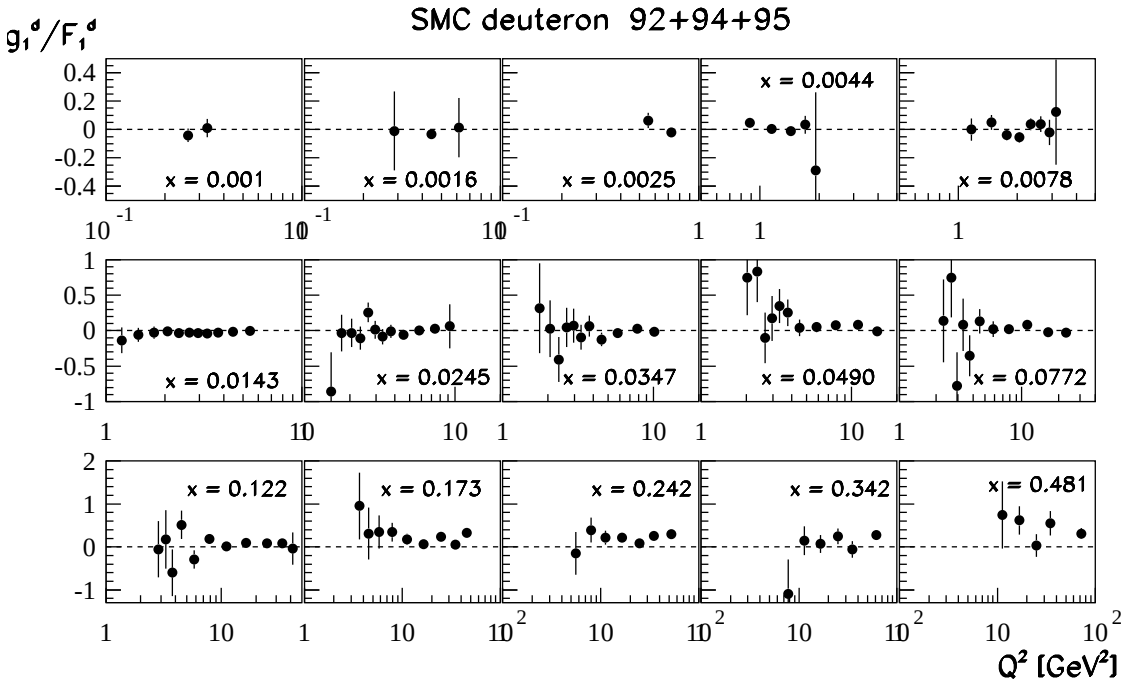

Figure 5.5: The structure function ratio $g_1/F_1 \simeq A_1$ for the deuteron as a function of Q^2 separate for each x bin. The data are preliminary.

functions for $x < 0.1$. However, it should be kept in mind that in the large-x region, the predictions from valence quark models [144, 145] describe the data well as stressed in Ref. [52]. For both, the proton and the neutron and thus for the deuteron the asymmetry is predicted to approach unity for $x \to 1$, a trend which clearly is visible in the proton data. Taking into account that the u-quark distribution function dominates at large x, as known from the structure function ratio F_2^n/F_2^p [124], this implies that those up quarks, which carry a large fraction of the proton's longitudinal momentum, are highly polarised in direction of the proton spin [31]. For the deuteron and even more so for the neutron it is not obvious from the data that the asymmetry approaches unity for $x \to 1$. However, the valence quark models predict a zero crossing of the neutron asymmetry only around $x \simeq 0.35$ followed by a fast rise to unity [52]. For the deuteron this results in an asymmetry of about 0.4 at $x = 0.5$ which is in good agreement with the present data. A measurement of the neutron or deuteron asymmetry at large $x \geq 0.8$ is needed to test these predictions. The additional 10° spectrometer of the SLAC experiment E-155 could possibly provide such data.

5.2.2 The Q^2 dependence of A_1

In Figure 5.5 the ratio g_1/F_1 for the deuteron as measured by the SMC is shown as a function of Q^2 for several fixed values of x [130]. The first three bins contain exclusively data with $Q^2 < 1$ GeV^2. Within the experimental precision no Q^2 dependence is seen. At small x, where a considerable Q^2 slope is expected from perturbative QCD, the asymmetries are small and in the order of the experimental uncertainties. Therefore, even for the bin with the most precise data, $x = 0.0143$, a large relative variation of the asymmetry with

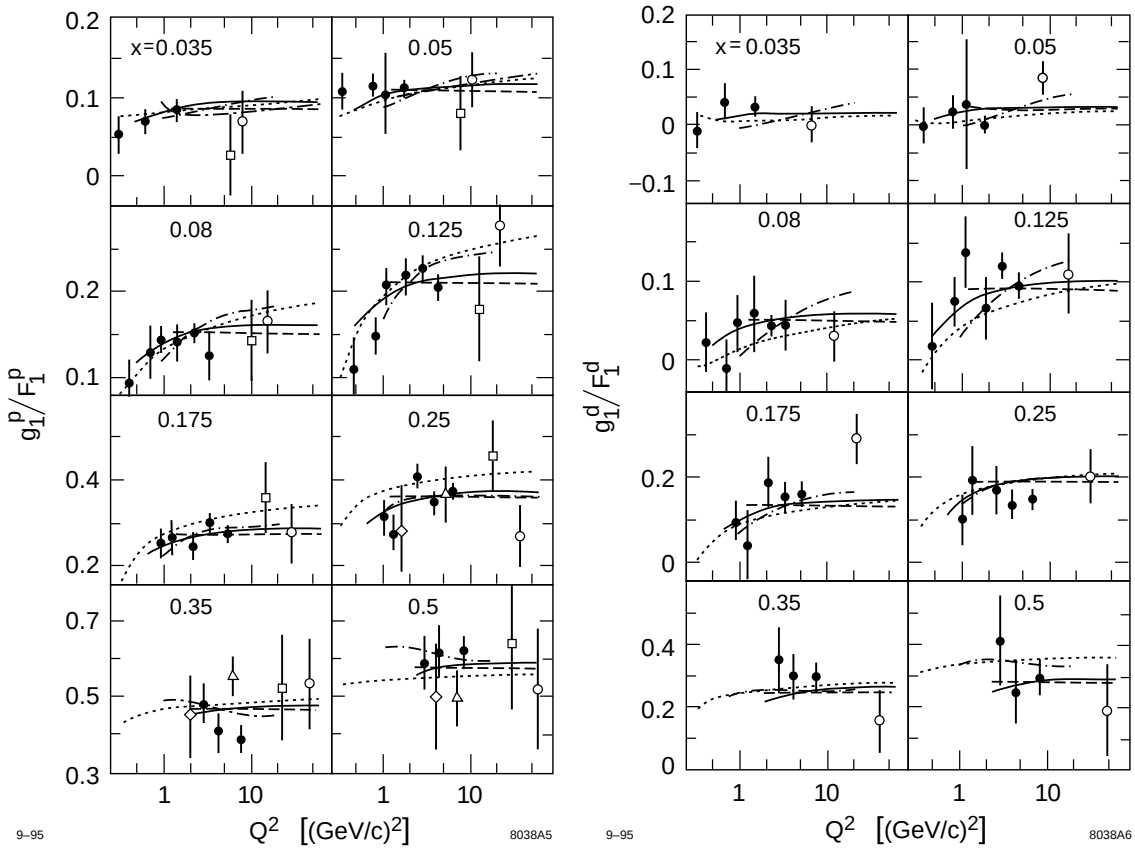

Figure 5.6: The structure function ratio g_1/F_1 for the proton (left) and the deuteron (right) a function of Q^2 for several x bins. Only statistical errors are shown. The data are from E-143 (full circles), E-130 (triangles), E-80 (diamonds), the EMC (squares), and the SMC (open circles). The NLO QCD fits form Refs. [146] and [55] are shown as dotted and dot-dashed lines, respectively. The solid and dashed lines represent a phenomenological fit and a constant, respectively.

Q^2 cannot be excluded from the data. At higher x, where only a weak Q^2 dependence of A_1 is expected, the data limit somewhat the size of the Q^2 dependence, particularly for the larger proton asymmetry not shown here. However, the precision is insufficient to detect slopes of the size predicted by QCD. This can be seen in Fig. 5.6, which is taken from a combined analysis of all proton and deuteron data [26] recently published by the E-143 collaboration. In this analysis additional data from E-143 runs with 9.7 GeV and 16.2 GeV incident-electron energy and data with $0.3 \leq Q^2 < 1$ GeV^2 were also included. From the SMC data only one point per x bin was used at the average Q^2 of the bin.

Together with the data, two next-to-leading order QCD fits are shown. Both, the fit by Glück, Reya, Stratmann, and Vogelsang [146] (standard scenario) and that by Ball, Forte, and Ridolfi [55] indicate a rise of the ratio g_1/F_1 for the proton and the deuteron in the region $0.03 < x < 0.3$. The radiatively generated parton distribution functions of Ref. [146] are valid down to $Q_0^2 = 0.34$ GeV^2 and show a decrease of g_1/F_1 below

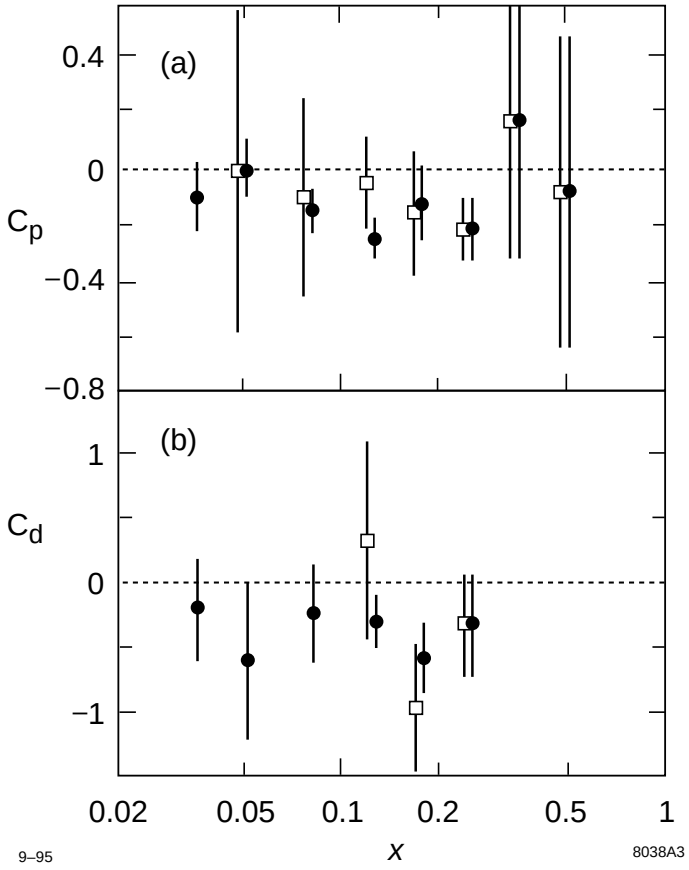

Figure 5.7: The parameters C_i as a function of x for the proton (a) and the deuteron (b). The fits were performed for two Q^2 ranges, $Q^2 > 0.3$ GeV^2 (full circles) and for $Q^2 > 1$ GeV^2 (open squares).

$Q^2 = 1$ GeV^2 in agreement with the data. The data in this region were not used in the analysis. The fit of Ref. [55] is valid only for $Q^2 > 1$ GeV^2. For more details of these QCD analyses see Sect. 5.6. The E-143 collaboration also performed several phenomenological fits to the $g_1/F_1 =: \mathcal{A}_1$ data using the functional forms

$$\begin{aligned} \mathcal{A}_1(x_i, Q^2) &= b_i, & Q^2 > 1.0 \text{ GeV}^2 \qquad \text{and} \\ \mathcal{A}_1(x_i, Q^2) &= a_i \left(1 + \frac{C_i}{Q^2}\right), & Q^2 > 0.3 \text{ GeV}^2. \end{aligned}$$

These fits are also shown in Fig. 5.6. It is obvious that the data are well described by the fitted constants, b_i. The parameters C_i resulting from the Q^2-dependent fit are shown in Fig. 5.7 as a function of x. While for the range $Q^2 > 0.3$ GeV^2 they show a negative trend, those obtained for $Q^2 > 1$ GeV^2 are clearly compatible with zero.

In summary, the data with $Q^2 > 1$ GeV^2 are compatible with no Q^2 dependence and the small Q^2 slopes predicted by next-to-leading QCD fits in the range $x > 0.03$ cannot be detected with the present experimental precision. For $Q^2 < 1$ GeV^2 the data indicate a positive Q^2 slope in some x bins.

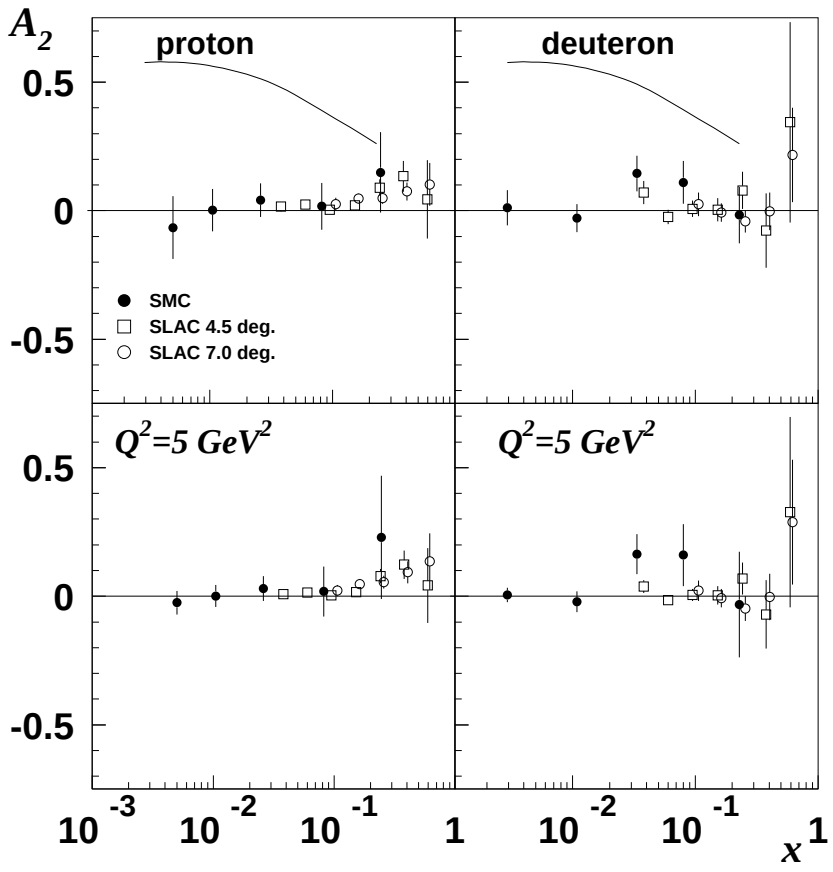

Figure 5.8: The virtual-photon asymmetry A_2 (upper row) and $\sqrt{Q^2/5\ \mathrm{GeV}^2}A_2$ (lower row) as a function of x for the proton (left) and the deuteron (right). The SMC data for the deuteron are preliminary.

5.3 The structure functions g_1 and g_2

5.3.1 The asymmetry A_2 and the structure function g_2

The interest in the virtual-photon asymmetry A_2 from an experimentalist's point of view is twofold. On one hand, A_2 contributes to the measured parallel asymmetry, $A_{\parallel}$. Therefore, in principle a determination of A_1 requires the measurement of both asymmetries, $A_{\parallel}$ and $A_{\perp}$. For convenience we repeat Eqs. 2.45 and 2.42 (p. 10),

$$A_{\parallel} = D(A_1 + \eta A_2), \qquad A_{\perp} = d(A_2 - \xi A_1), \qquad A_2 = \gamma \frac{g_1 + g_2}{F_1}. \tag{5.1}$$

Using the bound $|A_2| \leq \sqrt{R}$ as uncertainty for A_2 in the determination of A_1 leads to substantial contributions to the systematic error. On the other hand, there is a great physics interest in determining the nontrivial twist-3 part, $\bar{g}_2$, of the structure function g_2,

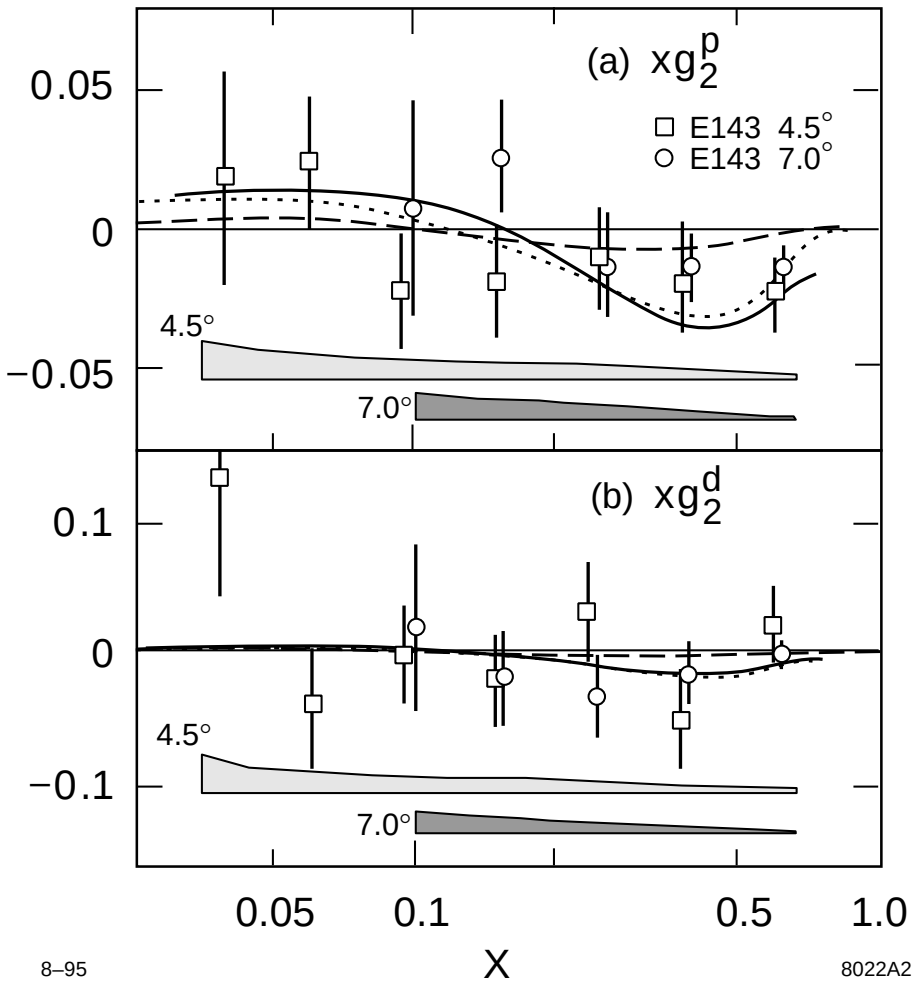

Figure 5.9: The structure function g_2 as a function of x for the proton (top) and the deuteron (bottom). Also shown are g_2^{ww} (solid line) and bag-model calculations from Refs. [147] (dotted) and [148, 149] (dashed).

which involves quark-gluon correlations and appears here in leading order

$$g_2(x, Q^2) = g_2^{\mathrm{ww}}(x, Q^2) + \bar{g}_2(x, Q^2). \tag{5.2}$$

The Wandzura–Wilczek term [71], g_2^{ww}, is of twist-2 and can be calculated from g_1 (Eq. 2.118, p. 22).

The SMC measurements of A_2 for the proton [20] and the deuteron [132] were mainly motivated by the goal to reduce the uncertainty in A_1. A determination of the structure functions g_2 and $\bar{g}_2$ was not attempted. The structure functions g_2^{p} and g_2^{d} were determined by the E-143 collaboration from their measurements of A_2 for $x > 0.03$ [27]. To compare the two measurements performed at different Q^2 one can either assume that $A_2(x, Q^2)$ or that $\sqrt{Q^2}A_2(x, Q^2)$ is independent of Q^2. The latter choice is motivated by Eq. 5.1 with $\gamma \propto \sqrt{Q^2}$ and assuming scaling for g_1 and g_2. The comparison of the data is shown in

Fig. 5.8 for both choices. The systematic uncertainties are small and only the statistical errors are shown. The data do not saturate the bound $\sqrt{R}$ and are compatible with zero with the possible exception of the proton data for $x > 0.2$.

Figure 5.9 shows the nucleon's second spin dependent structure function, xg_2, as determined in the SLAC experiment E-143. Also shown are the Wandzura–Wilczek contribution, $g_2^{\rm ww}$, calculated from g_1 and two bag-model calculations of g_2 for $Q^2 = 5$ GeV^2 by Stratmann [147] and by Song and McCarthy [148,149]. The proton data show a trend to be negative for $x > 0.2$ in agreement with the expectation from $g_2^{\rm ww}$. The deuteron data are compatible with both, $g_2^{\rm ww}$ and zero. Within the present precision the data are also compatible with the two bag-model predictions. Large twist-3 contributions can be excluded. Therefore, it will be unfortunately very difficult to assess $\bar{g}_2$ experimentally.

To test the Burkhardt–Cottingham sum rule [67], $\int_0^1 g_2(x)\,\mathrm{d}x = 0$, (Eq. 2.115, p. 21), the integrals were calculated for the range $0.03 \le x \le 1$ and $Q^2 = 5$ GeV^2

$$\begin{aligned} \int_{0.03}^{1} g_2(x)\,\mathrm{d}x &= -0.013 \pm 0.028 \qquad \text{(proton)} \\ \int_{0.03}^{1} g_2(x)\,\mathrm{d}x &= -0.033 \pm 0.082 \qquad \text{(deuteron).} \end{aligned}$$

The results are compatible with zero. The results for the higher moments of g_2 will be discussed in the context of higher-twist contributions to the first moment of g_1 in Sect. 5.9.

5.3.2 Evaluation of g_1 from the asymmetries

Some confusion was generated by the different ways the SMC data and some of the SLAC data were analysed. For clarity we shortly discuss the two approaches. The structure function g_1 is obtained from the asymmetry A_1 or from $\mathcal{A}_1 = g_1/F_1$ using Eq. 2.46 (p. 11)

$$g_1(x,Q^2) = \frac{F_1}{1+\gamma^2}\left\{A_1(x,Q^2) + \gamma A_2(x,Q^2)\right\}.$$

In the SMC analysis A_2 was neglected in both, the evaluation of A_1 from $A_{\|}$ and in that of g_1 from A_1. For the SLAC data, where the contribution of A_2 is much larger, A_2 is already entirely accounted for in the evaluation of $\mathcal{A}_1$ from $A_{\|}$ and thus does not appear in the evaluation of g_1 from $\mathcal{A}_1$ anymore. Of course the two methods are equivalent for vanishing A_2 as far as g_1 is concerned, however two different formulæ must be used to derive g_1 from the intermediate results, A_1 and $\mathcal{A}_1$, respectively

$$g_1(x,Q^2) \simeq \frac{F_2(x,Q^2)}{2x\,(1+R(x,Q^2))} \quad \begin{cases} A_1(x,Q^2) & \text{(SMC)} \\ (1+\gamma^2)\,\mathcal{A}_1(x,Q^2) & \text{(SLAC } g_1/F_1\text{).} \end{cases} \tag{5.3}$$

In all experimental analyses the parametrisations of $F_2(x,Q^2)$ by the NMC [133] and of $R(x,Q^2)$ by SLAC [134] were used. The kinematics of the SMC data agrees largely with that of the NMC data, which were actually taken with the same spectrometer. Since the NMC also used the SLAC parametrisation of $R(x,Q^2)$ in their evaluation of $F_2(x,Q^2)$ from the deep-inelastic cross sections the uncertainty due to R effectively cancels in $g_1(x,Q^2)$.

In Figure 5.10 all available g_1 data for the proton, the deuteron, and the neutron are shown. The SMC data were obtained with F_2 and R evaluated at the average Q^2 of the data in the considered x bin, ranging from 1.3 GeV^2 at small x to 50 GeV^2 at large

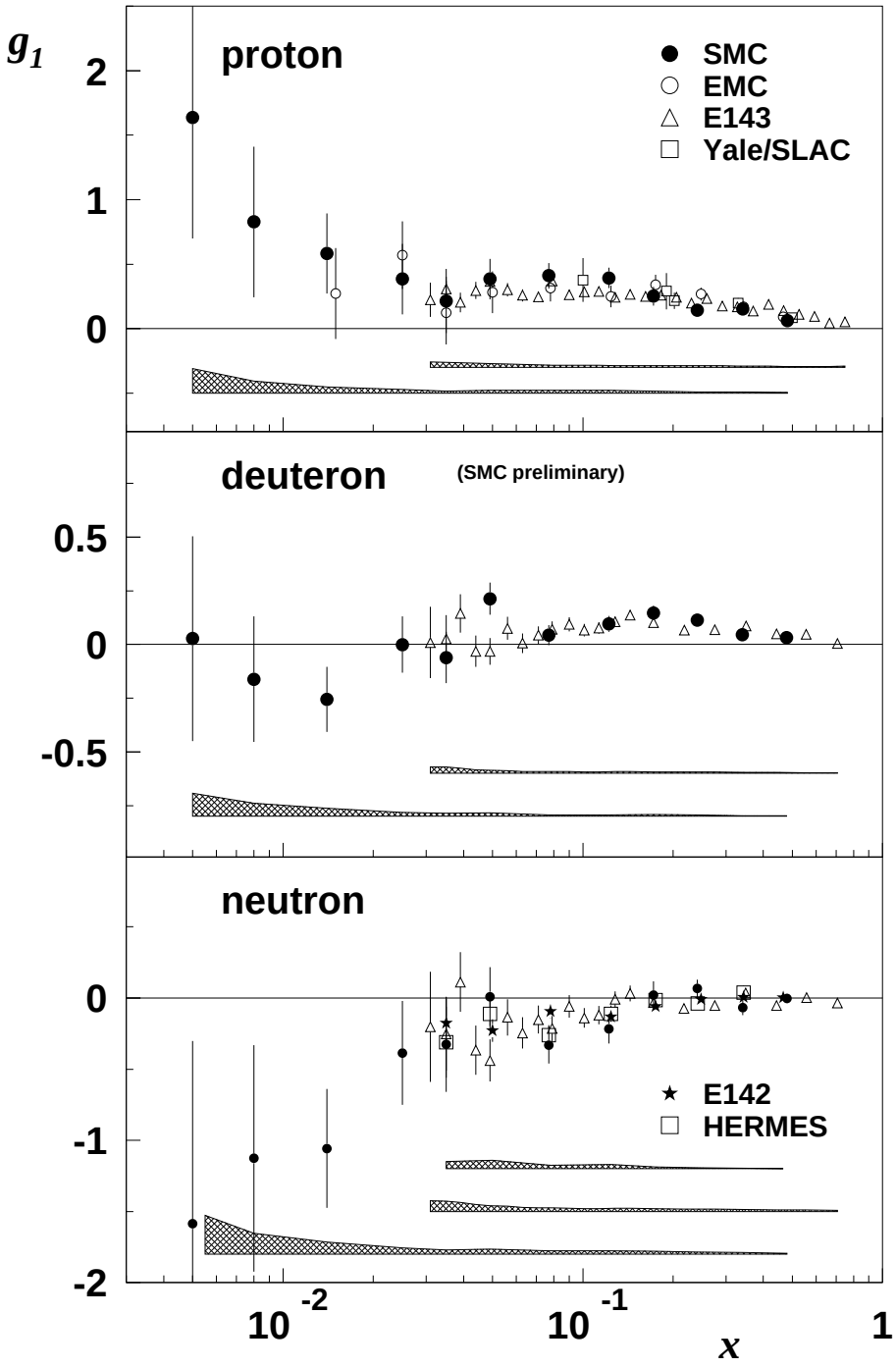

Figure 5.10: The structure function $g_1(x, Q^2)$ as a function of x for the proton, the deuteron, and the neutron. For the neutron also data obtained from proton and deuteron measurements of the SMC and E-143 are shown. The systematic uncertainties of the SMC, E-142, and E-143 data are shown as shaded bands.

x. The SLAC data are shown as published for a fixed $Q^2 = 3$ GeV^2 (proton, deuteron) and 2 GeV^2 (neutron). Often comparisons are presented with all data "evolved" to a common Q^2 assuming scaling of A_1 or g_1/F_1. Such a procedure introduces additional uncertainties and is not justified at small x, where the Q^2 dependences of F_1 and g_1 are certainly different. In particular the first g_1^{p} data point from the SMC moves up by almost a factor two when "evolved" from 1.3 to 10 GeV^2 assuming scaling of A_1. This may lead to wrong estimates of the small-x behaviour of g_1. The agreement of the data sets assuming scaling for A_1 can better be judged from the asymmetries themselves (Fig. 5.4). We therefore prefer to show the structure-function data as published. For the evaluation of the first moment an evolution to a common Q^2 is inevitable. However, in this case the main contribution comes from a region where scaling of A_1 is not an unreasonable assumption.

Interesting is the small-x behaviour of g_1^{p} and g_1^{n} in Fig. 5.10. While in the unpolarised case the ratio $F_2^{\mathrm{n}}/F_2^{\mathrm{p}}$ approaches unity [124, 150], the ratio $g_1^{\mathrm{n}}/g_1^{\mathrm{p}}$ is close to -1 at $x \simeq 0.005$. In terms of quark distribution functions the difference $g_1^{\mathrm{p}}(x) - g_1^{\mathrm{n}}(x)$ is given by

$$g_1^{\mathrm{p}}(x) - g_1^{\mathrm{n}}(x) = \frac{1}{6}\left\{\Delta u(x) - \Delta d(x)\right\} \tag{5.4}$$

and becomes equal to the difference of the valence quark distribution functions under the assumption of an isospin-symmetric quark sea, $\Delta\bar{u}(x) = \Delta\bar{d}(x)$. Thus the behaviour of the structure functions either indicates that the isospin symmetry in the quark sea is broken or that the valence quarks also dominate at small x as far as polarisation is concerned. The latter scenario is in agreement with the analysis of the semi-inclusive data of the SMC [22] (Sect. 5.7) which yields $\Delta u_{\mathrm{v}}(x) > 0$ and $\Delta d_{\mathrm{v}}(x) < 0$.

5.3.3 Neutron data from proton, deuteron, and ^{3}He experiments

The neutron structure functions were determined from the combination of deuteron and proton data and from ^{3}He data assuming independent scattering from the individual nucleons in the nucleus. While the deuteron represents the sum of a proton and a neutron, ^{3}He is basically a 'pure' neutron target because the spins of the two protons are coupled to zero most of the time. The following points must be discussed in the analysis of data from nuclear targets.

- The average polarisation of the nucleons must be known and taken into account.
- For nuclei with spin ≥ 1 additional structure functions appear.
- The parton distribution functions of bound nucleons differ from those of free nucleons.

In the deuteron both, the proton and neutron spin, point in direction of the deuteron spin for the S state and opposite to it for the D state. The average polarisations of the proton and the neutron in the deuteron are thus equal and given by

$$P_{\mathrm{p}}^{\mathrm{d}} = P_{\mathrm{n}}^{\mathrm{d}} = \left(1 - \frac{3}{2}\omega_{\mathrm{D}}\right), \tag{5.5}$$

where $\omega_{\mathrm{D}} \simeq 0.05 \pm 0.01$ [151] is the probability for the deuteron to be in the D state. The factor 3/2 is due to the Clebsch–Gordan coefficients. For the structure function we obtain

$$g_1^{\mathrm{d}}(x, Q^2) = \frac{1}{2}\left\{g_1^{\mathrm{p}}(x, Q^2) + g_1^{\mathrm{n}}(x, Q^2)\right\}\left(1 - \frac{3}{2}\omega_{\mathrm{D}}\right). \tag{5.6}$$

For ^{3}He many components exist in the wave function. The dominant one is an S wave with the proton spins coupled to zero. Taking all contributions into account one finds [31, 152, 153]

$$P_{\rm n}^{^3{\rm He}} = 0.087 \pm 0.02, \qquad \text{and} \qquad P_{\rm p}^{^3{\rm He}} = -0.025 \pm 0.003 \tag{5.7}$$

yielding

$$g_1^{^3{\rm He}}(x,Q^2) = \frac{1}{3}\left\{(0.87 \pm 0.02) g_1^{\rm n}(x,Q^2) - (0.050 \pm 0.006) g_1^{\rm p}(x,Q^2)\right\}. \tag{5.8}$$

More correctly, the nuclear structure function is a convolution of the nucleon structure function and the nucleon momentum distribution in the nucleus leading to an x-dependent relation between the nucleon and nucleus structure functions. A detailed study of the convolution ansatz starting from a covariant framework is given in Ref. [154]. The authors find for the deuteron, that the simple formula of Eq. 5.6 gives reliable results for $x < 0.6$. This also applies for $g_T = g_1 + g_2$.

The second point in the list above only concerns the deuteron data and is discussed in some detail in Sect. 2.5. Contributions from the b_1 structure function are expected to be small and out of reach for the present experiments. In the analysis of the deuteron data from E-143 and the SMC such contributions were neglected.

The third point is more complicated. From unpolarised scattering we know that the parton distribution functions of bound and free nucleons differ considerably (Fig. 4.2). The parton distribution functions of the bound nucleon are depleted for $x \leq 0.1$ (shadowing) and around $x \simeq 0.6$ (original EMC effect), while a strong enhancement due to Fermi motion is found for $x > 0.8$. The latter effect is not important for the first moments since g_1 is very small in this region. The depletion in the intermediate region is related to the pion cloud in the nucleus and might be smaller in the polarised case because pions are spinless. These nuclear effects increase with the nuclear mass, A, and are small for the deuteron and helium. The structure function ratio $F_2^{\rm n}/F_2^{\rm p}$ as determined from proton and deuteron data never exceeds the value 0.96 [124, 150] (Fig. 4.3). For small x, where the quark sea dominates, one expects that $F_2^{\rm n}/F_2^{\rm p}$ approaches unity. This 4 % difference corresponds to a 2 % shadowing effect in the deuteron. The structure function ratio $F_2^{^4{\rm He}}/F_2^{\rm d}$ was measured by the NMC [125, 155] and at larger x by the SLAC experiment E-139 [127]. At $x = 0.005$ a shadowing effect of about (5 ± 2) % was found [125]. Helium-3 data exist [156], however only outside of the deep-inelastic kinematic region. Nuclear effects were studied in a quark-cluster model, which takes into account six-quark bags in addition to the nucleon [157]. These models usually describe the unpolarised data well, but are also very flexible. Both, the first moments $\Gamma_1^{\rm d}$ and $\Gamma_1^{^3{\rm He}}$ were predicted to receive about the same additive correction in the order of $\delta\Gamma_1 \simeq 0.005$ due to the presence of six-quark bags. However, the paper emphasises the fact that the correction is about the same for both nuclei rather than its absolute size.

If the nuclear effects in the polarised case are of a similar size as those in the unpolarised case, their neglect is justified given the present accuracy of the data, but might become a concern in more precise future experiments. An interesting experiment would be to determine the proton structure function, $g_1^{\rm p}$, using a polarised tritium target and to compared it to that of the free proton.

5.3.4 The small-x behaviour of g_1

From Regge theory it is expected that for moderate fixed Q^2 and for $\nu \to \infty$, i.e. $x \to 0$, the iso-triplet part of g_1 behaves like [158]

$$\frac{1}{12}\left(\Delta u(x) - \Delta d(x)\right) = g_1^{(3)}(x) \propto x^{-\alpha}, \qquad x \to 0. \tag{5.9}$$

The lowest contributing Regge trajectory is that of the a_1 meson. Its intercept is expected to be in the range $-0.5 < \alpha < 0$ [159]. In most analyses of the first moment of g_1 a small-x behaviour according to Eq. 5.9 was assumed for the extrapolation, often with $\alpha = 0$, i.e. $g_1(x) = const$, which gives the largest contribution. The error estimates for the extrapolations usually include the quoted range of α. Although the deuteron is a pure iso-singlet combination, the iso-triplet shape is usually also assumed for the extrapolation of deuteron data. Another reason to apply Regge behaviour with care is that the spin-averaged structure function F_2 rises with decreasing x down to $x = 10^{-4}$, even at Q^2 as small as 1.5 GeV^2 [160]. A behaviour which Regge-inspired models fail to reproduce.

The behaviour of the flavour-singlet part of g_1 was studied by Bass and Landshoff [161]. They find a contribution from the exchange of two non-perturbative gluons which behaves like

$$\frac{1}{9}(\Delta u(x) + \Delta d(x) + \Delta s(x)) = g_1^{(0)}(x) \propto (2\ln\frac{1}{x} - 1), \qquad x \to 0. \tag{5.10}$$

It was suggested that the flavour-singlet part is responsible for the tendency of g_1^{p} to rise at small x, see Fig. 5.10. However, for g_1^{d}, which is almost a pure flavour-singlet combination, such a rise is not observed. This rather suggests that the rise is caused by the iso-triplet part of g_1, which is absent in the pure iso-singlet combination g_1^{d}. The drop in g_1^{n} towards small x expresses the same observation. For the Bjorken sum as a pure iso-triplet combination only the behaviour of $g_1^{(3)}$ is relevant.

Several other approaches were discussed by Close and Roberts [162], the most extreme being

$$g_1(x) \propto \frac{1}{x\ln^2 x}, \qquad x \to 0. \tag{5.11}$$

A behaviour of this form was criticised by Anselmino, Ioffe, and Leader [163] and such a rise is incompatoble with the deuteron data.

From perturbative QCD it is expected that $|g_1|$ rises as $x \to 0$ [164,165]. For a positive gluon polarisation, g_1 will eventually at small x and high Q^2 become negative. The growth is exponential in the variables $\xi = \ln(x_0/x)$ and $\zeta = \ln(t/t_0)$ with $t = \ln(Q^2/\Lambda^2)$ for $\xi\zeta \to \infty$. The exact form of the small-x behaviour depends on the parton distribution functions at the starting scale of the evolution. In all cases the growth is faster than any power of $\ln(1/x)$. For higher Q^2 this rise is likely to mask any intrinsic Regge-like low-Q^2 behaviour. The HERA data for F_2 indeed show the predicted double logarithmic scaling behaviour predicted on the same grounds [166].

The small-x behaviour as obtained from a QCD analysis [55] using the GLAP equations in next-to-leading order is just opposite to the scenario [161] discussed above. The QCD analysis favours a Regge-like behaviour of the flavour-singlet parton distribution for $Q^2 = 1$ GeV^2. The nonsinglet parton distribution is found to grow approximately like $1/\sqrt{x}$, causing a rise of g_1^{p} towards small x. However, at $Q^2 = 10$ GeV^2 the singlet part has evolved to large negative values and dominates the behaviour of g_1^{p}, causing a strong drop towards small x, see also Sect. 5.6. Thus the actual behaviour of g_1^{p} crucially depends

on the delicate interplay of the opposite behaviours of the singlet and nonsinglet part, making small x a very interesting but hard-to-predict region. The deuteron is an almost pure flavour-singlet combination and therefore no rise is expected here towards small x in agreement with the data.

In summary, presently the predictions for the small-x behaviour of g_1 vary widely. A particular difficulty lies in defining the x and Q^2 domain where a certain model is applicable. Therefore, it is mandatory to measure to as low values of x as possible. More precise data at somewhat larger x may also help to narrow the range of the predictions. Recently, also the g_1 behaviour at very small x in the HERA kinematic domain was studied, see Sect. 6.2.

5.4 The first moment of g_1

5.4.1 The first moment of g_1 and the Ellis–Jaffe sum rules

The first moment,

$$\Gamma_1(Q_0^2) = \int_0^1 g_1(x, Q_0^2)\mathrm{d}x, \tag{5.12}$$

must be evaluated at the same fixed Q_0^2 for all x. The Q_0^2 values chosen for the SMC, the E-143, and the E-142 data are 10, 3, and 2 GeV^2, respectively. They represent typical average values for the data sets. The following procedure was used in the experimental analyses up to now. To evolve the g_1 data from Q_m^2, where the measurement was performed, to Q_0^2, scaling of either A_1 or g_1/F_1 is assumed, i.e. $A_1(x, Q_0^2) = A_1(x, Q_\mathrm{m}^2)$. Then $g_1(x, Q_0^2)$ is calculated from Eq. 5.3 using $F_2(x, Q_0^2)$ and $R(x, Q_0^2)$. Then g_1 must be extrapolated into the unmeasured regions. The extrapolation to $x = 1$ is uncritical, because of the smallness of g_1 in this region. The extrapolation to $x = 0$ is performed assuming a Regge-like behaviour, $g_1(x) \propto x^{-\alpha}$ with $-0.5 \leq \alpha \leq 0$. For the SMC data such an extrapolation is only needed for $x < 0.003$ and the quoted uncertainties cover most of the scenarios for the small-x behaviour of g_1 discussed in Sect. 5.3.4. For the SLAC data the unmeasured region is ten times larger. The combination of the high statistics data at $x > 0.03$ with a specific functional form assumed for $g_1(x \to 0)$ can easily lead to an underestimate of the extrapolation errors. This is in particular true since in none of the models the onset of the predicted behaviour in x and Q^2 is well defined. The errors quoted for the extrapolations of the E-142 and E-142 data to $x = 0$ are smaller than the errors of the integrals obtained from the SMC data in the region $0.003 \leq x \leq 0.03$. The difficulty to correctly extrapolate to $x = 0$ is most evident for g_1 of the neutron (Fig. 5.10) [167]. A constant fitted to the E-143 or E-142 data misses all three SMC small-x points by one to two standard deviations. Due to the smallness of Γ_1^n the extrapolation can contribute a considerable fraction of the first moment.

The results for the first moments Γ_1^p, Γ_1^d, and Γ_1^n from the EMC, SMC, SLAC, and HERMES experiments are summarised in Table 5.2 together with the predictions of the Ellis–Jaffe sum rules. The latter were calculated using $g_a = 1.2573 \pm 0.0028$ [51], $F/D = 0.575 \pm 0.016$ [52], and including QCD corrections up to $\mathcal{O}(\alpha_s^3)$. They were evaluated with $n_f = 3$ and $\alpha_s(M_Z^2) = 0.117 \pm 0.005$ [51], corresponding to $\alpha_s(Q^2) = 0.35$, 0.31, and 0.24 for $Q^2 = 2$, 3, and 10 GeV^2, respectively. A comparison of the predictions and the experimental results is shown in Fig. 5.11. All proton and deuteron data show a violation of the Ellis–Jaffe sum rules. The most significant results are obtained for the deuteron,

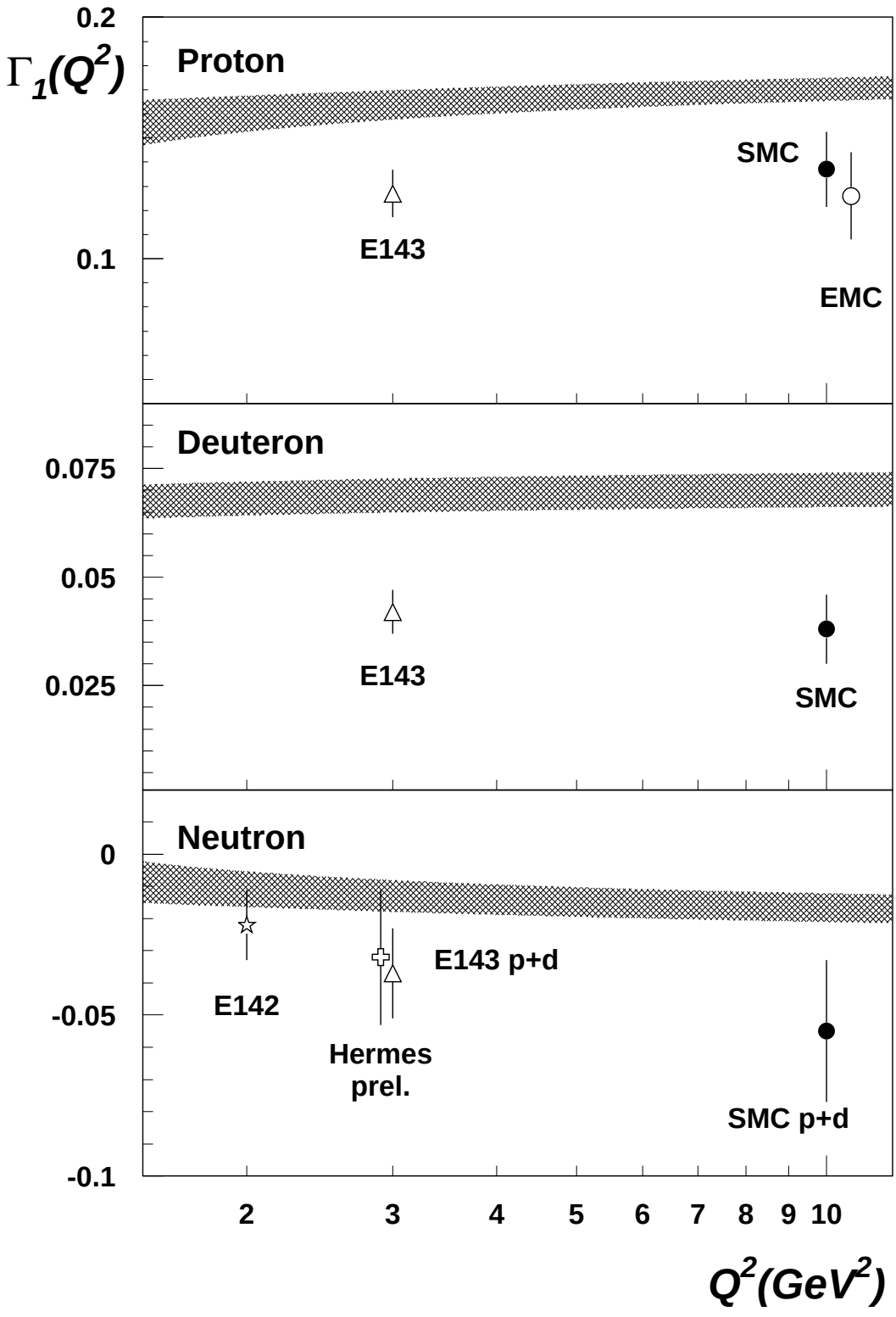

Figure 5.11: Comparison of the experimental results for $\Gamma_1(Q^2)$ and the Ellis–Jaffe sum-rule predictions (shaded bands) as a function of Q^2 for the proton, the deuteron, and the neutron.

Table 5.2: Results for the first moments of the proton, the deuteron, and the neutron.

experiment	Q_0^2	$\Gamma_1(Q^2)$		
	GeV^2	proton	deuteron	neutron
EMC	10.7	0.126 (10) (15)		
SMC	10	0.137 (14) (10)	0.038 (7) (5)	*−0.055 (24)*
SMC[a]	10	0.130	0.037	*−0.050*
E-143[b]	3	0.127 (4) (10)	0.042 (3) (4)	*−0.037 (8) (11)*
E-143[c]	3	0.121 (4) (10)	0.040 (3) (4)	*−0.035 (8) (11)*
E-142	2			−0.022 (11)
E-142[d]	2			−0.032 (6) (9)
E-142[d]/SMC[e]	2			−0.053 (13)
HERMES	3			−0.032 (13) (17)
Ellis–Jaffe	10	0.170 (5)	0.071 (4)	−0.016 (5)
sum rule	3	0.164 (6)	0.070 (4)	−0.013 (5)
	2			−0.011 (5)

The SMC deuteron data and the HERMES neutron data are preliminary. Statistical and systematic errors are given separately where available. The neutron data in *italics* were obtained combining proton and deuteron data. [a)] Using a preliminary NLO pQCD analysis to evolve the data. [b)] Assuming g_1/F_1 scales, as published [24, 25] and [c)] assuming A_1, A_2 scale [168]. [d)] Data from the Ph. D. thesis of Kawall [169]. [e)] Using the SMC 'neutron' data below $x = 0.03$.

where the iso-triplet part cancels in the first moment. The SMC and E-143 deuteron data lie 3.5 and 4.6 standard deviations below the sum-rule prediction. The apparent small difference between the EMC and SMC proton results arises entirely from the region, $0.003 \leq x \leq 0.01$, unmeasured by the EMC. For the overlap region, $0.01 \leq x \leq 1$, the integrals are 0.123 ± 0.018 and 0.120 ± 0.016 for the EMC and the SMC data, respectively.

An error for the evolution of the g_1 data to the common Q_0^2 is not included in any of the data for the first moment. However, the size of a possible effect can be estimated from the entries labled SMC[a] and E-143[c] in Table 5.2. The SMC evaluated the first moments also using the Q^2 evolution as obtained from a next-to-leading order QCD analysis. The parton distribution functions were fitted at a starting scale of $Q^2 = 1$ GeV^2 to all proton and deuteron data using the computer code of Ball, Forte, and Ridolfi [55], see Sect. 5.6. The result is similar to the one obtained in Ref. [55] using only the SMC and E-143 data. Then $g_1^{\rm fit}$ at $Q_{\rm m}^2$ and at $Q_0^2 = 10$ GeV^2 was calculated from the fitted parton distribution functions. The difference was added to the corresponding data point to obtain

$$g_1(x, Q_0^2) = g_1(x, Q_{\rm m}^2) + \left\{ g_1^{\rm fit}(x, Q_0^2) - g_1^{\rm fit}(x, Q_{\rm m}^2) \right\}. \tag{5.13}$$

For the proton the result for Γ_1 is lower by half the statistical error while for the deuteron the effect is negligable. The different behaviour for the proton and the deuteron is due to the nonsinglet quark distribution, which causes the strong variation of g_1 with Q^2 at small x and which is almost absent in the deuteron.

The E-143 data were also analysed assuming scaling behaviour for A_1 and A_2 instead for g_1/F_1 [168]. Again for $\Gamma_1^{\rm p}$ a lower result is obtained. The difference of 1.5 times

the statistical error is still covered by — although not included in — the systematic uncertainty. This clearly demonstrates, that the uncertainty in the Q^2 evolution cannot be ignored. Although the recent QCD analyses of the g_1 data provide a solid ground to perform the evolution, a careful assessment of the uncertainties still has to be performed. This is presently carried out for the SMC data [123].

In the original publication of the E-142 neutron result [23] an experimental value of $\Gamma_1^n = -0.022 \pm 0.011$ was compared to a prediction of the Ellis-Jaffe sum rule of -0.021 ± 0.018. However, when higher order corrections are included, the Ellis–Jaffe sum rule rather yields $\Gamma_1^n = -0.011 \pm 0.005$ at $Q^2 = 2$ GeV^2. In the meanwhile the E-142 data were re-analysed yielding a quite different value of $\Gamma_1^n = -0.032 \pm 0.011$ as reported in the Ph. D. thesis of Kawall [169]. This value is 1.7 standard deviations below the Ellis–Jaffe prediction and in good agreement with the E-143 result as obtained from their proton and deuteron data.

The lower neutron first moment, $\Gamma_1^n = -0.55 \pm 0.024$, obtained from the SMC proton and deuteron data is entirely due to the decrease of g_1^n for $x < 0.03$ outside the region accessible to the SLAC experiments (Fig. 5.10). The integral for the region $0 \leq x < 0.03$ from the first four SMC g_1^n points and an extrapolation to $x = 0$ amounts to -0.027 ± 0.009. The points were measured at $Q^2_m = 1.3$, 2.1, 3.6, and 5.9 GeV^2, respectively, close to $Q_0^2 = 2$ GeV^2 of the E-142 data. In this x region g_1 is expected to vary only slowly with Q^2. Replacing in the updated E-142 result the extrapolation of -0.0065 for $x < 0.03$ by value from the SMC data yields $\Gamma_1^n = -0.053 \pm 0.013$ similar to the SMC result at 10 GeV^2.

Until a re-analysis of the E-142 neutron data is published these data must be considered as preliminary and to some extend as unreliable given the high precision quoted. Therefore, presently only the neutron data obtained from the proton and deuteron data of E-143 and SMC experiments should be used, e.g. in the evaluation of the Bjorken sum rule. Further input for this region will come from the SMC proton experiments in 1996 and the SLAC experiments E-154[1] and E-155 at 48 GeV.

5.4.2 Test of the Bjorken sum rule

The results for the Bjorken sum, $\Gamma_1^p - \Gamma_1^n$, are summarised in Table 5.3 and shown in Fig. 5.12. The predictions were calculated including corrections up to $\mathcal{O}(\alpha_s^3)$. Note that the only two independent determinations of the Bjorken sum are those by the SMC and the E-143 collaboration from their proton and deuteron data using

$$\Gamma_1^p - \Gamma_1^n = 2 \left\{ \Gamma_1^p - \Gamma_1^d \frac{1}{1 - \frac{3}{2}\omega_D} \right\}. \tag{5.14}$$

The E-142 data were included for completeness and the given errors should be taken with care (see Sect. 5.4.1). All results and their various combinations agree with the Bjorken

[1] After this paper was finished we received a preliminary g_1^n result from the E-154 experiment shown by E. Hughes at the *Int. Conf. of High Energy Physics*, Warsaw, Poland, July 25, 1996. For $x > 0.014$ it confirms with an impressive statistical accuracy the decreasing trend of g_1^n towards small x seen in the SMC data. A reliable extrapolation from these data appears to be very difficult. The integral is therefore only given in the measured range $0.014 \leq x \leq 0.7$ and amounts to $-0.037 \pm 0.004 \pm 0.010$ at $Q^2 = 5$ GeV^2. A power-law fit in the region $x < 0.1$ yields $g_1^n = -0.02 x^{-0.8}$ which would contribute -0.043 for the small x extrapolation.

Table 5.3: Results for the Bjorken sum.

experiment	Q_0^2 GeV^2	$(\Gamma_1^p - \Gamma_1^n)(Q_0^2)$ experiment	sum rule
SMC	10	0.191 (36)	0.187 (3)
SMC[a]	10	0.180 (34)	
E-143[b]	3	0.163 (19)	0.177 (6)
E-143[c]	3	0.156 (19)	
E-142 (n) & E-143 (p)	3	0.149 (14)	
E-142[d] (n) & E-143 (p)	3	0.160 (14)	
E-142[d] (n) & E-143 (p) & SMC[e]	3	0.181 (16)	

For the superscripts see Table 5.2 (p. 76).

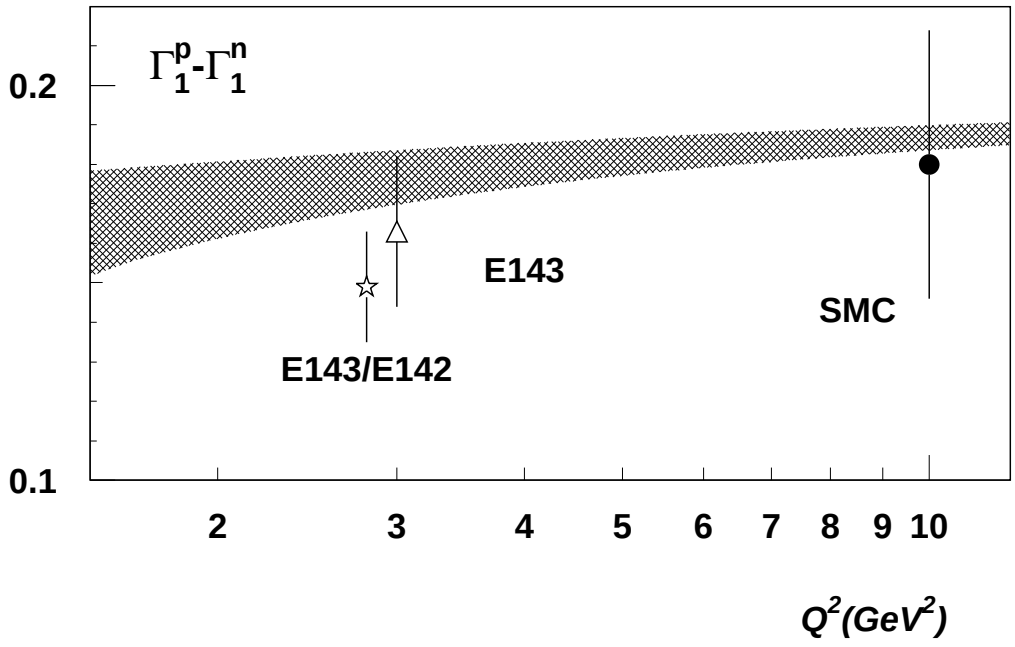

Figure 5.12: Comparison of the experimental results for the Bjorken sum and the sum-rule prediction (shaded band) as a function of Q^2. The data points correspond to the entries labelled SMC, E-143[b], and E142 (n) & E-143 (p) in Table 5.3. For clarity the E-142 & E-143 point is shown at a sightly lower value of Q^2.

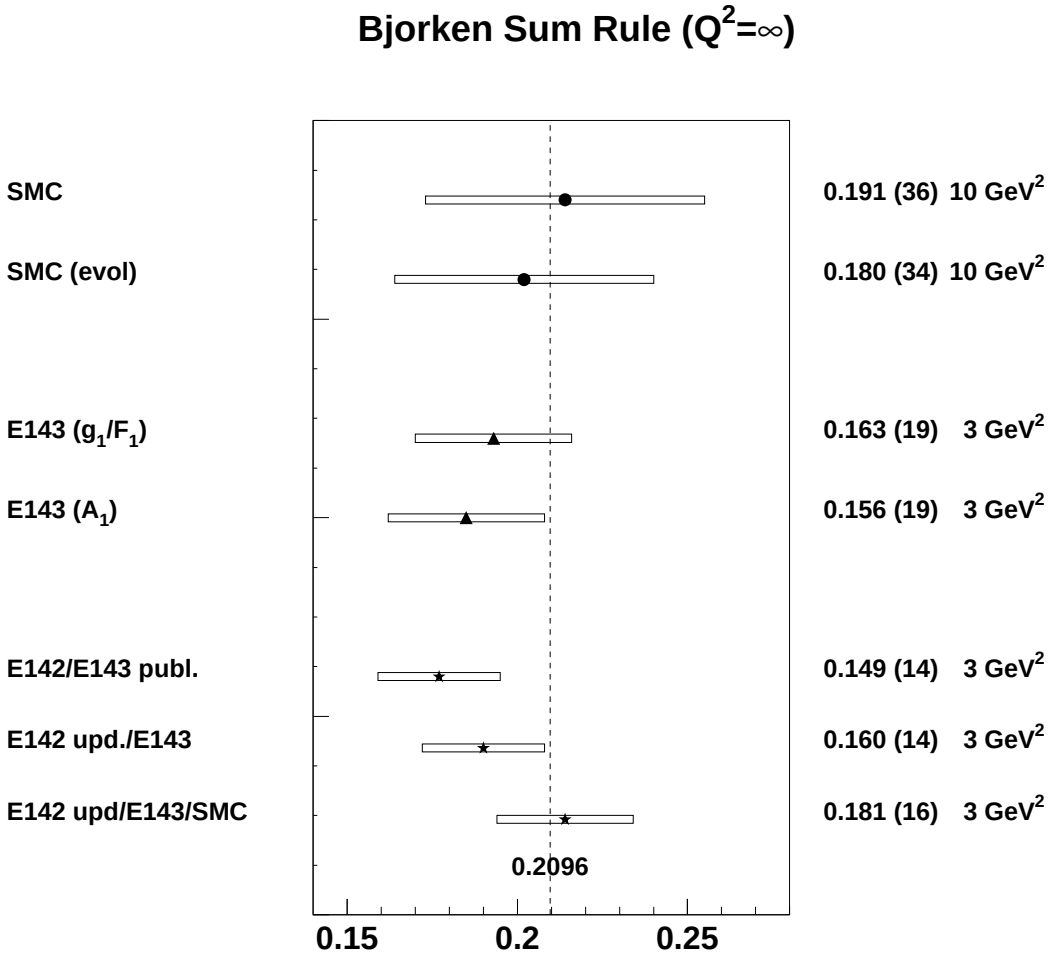

Figure 5.13: Comparison of the experimental results for the Bjorken sum evolved to $Q^2 = \infty$. For the various data point see text and Table 5.3 (p. 76).

sum-rule prediction within about one standard deviation, apart from the combination of the E-142 neutron data with the E-143 proton data which yields a value 1.8 standard deviations below the prediction. To compare the experimental results directly they were converted to the corresponding leading order values, i.e. to the Bjorken sum for $Q^2 = \infty$. The experimental uncertainty and the one due to α_s were added in quadrature for this comparison which is shown in Fig. 5.13.

A combined analysis of all data on the level of the structure functions is presently being carried out by the SMC [123]. This analysis will take into account the correlations between the different data sets and use a next-to-leading QCD analysis for the evolution to a common value of Q^2.

5.4.3 The Bjorken sum rule and the strong coupling constant

Recently a determination of the strong coupling constant, α_s, from the Bjorken-sum data was published by Ellis *et al.* [170, 171]. The emphasis of this paper is on a study of the perturbation series, $f(a)$, using the technique of Padé approximants, where

$$\Gamma_1^{\mathrm{p}} - \Gamma_1^{\mathrm{n}} = \frac{1}{6} g_a f(a) \tag{5.15}$$

and

$$f(a) = \sum_{n=0}^{\infty} c_n a^n, \qquad \text{with } a = \frac{\alpha_s}{\pi}. \tag{5.16}$$

It is known that the coefficients c_n eventually show a factorial ($n!$) growth. This is due to an exponential decrease of the average virtuality of the involved gluons with increasing n in certain Feynman graphs related to the running of α_s. Re-expressing the low-scale coupling constant relevant for these gluons by that at the large external scale, Q^2, causes the growth of the coefficients c_n [172].

In order to obtain a reliable determination of α_s from the Bjorken sum one either has to stay in a regime, where α_s is small and where using the perturbative series up to $n \simeq 1/\alpha_s$ is sufficient, or one has to estimate the full perturbation series reliably. The latter approach is studied in Ref. [171], in which the perturbation series, $f(a)$, for the Bjorken sum is approximated for $n_f = 3$ by

$$f^{\mathrm{PA}}(a) = \frac{1 - 8.805a + 11.974a^2}{1 - 7.805a + 7.763a^2}. \tag{5.17}$$

Using this result and an experimental value of $\Gamma_1^{\mathrm{p}} - \Gamma_1^{\mathrm{n}} = 0.164 \pm 0.011$ at $Q_0^2 = 3$ GeV^2 they obtain

$$\alpha_s(M_{\mathrm{Z}}^2) = 0.116^{+0.003}_{-0.005} \pm 0.003, \tag{5.18}$$

where the second error accounts for the theoretical uncertainty including higher-twist contributions, see Sect. 5.9. The values for α_s at $Q^2 = 3$ GeV^2 differ considerably when evaluated using the perturbation series up to third and fourth order and using Eq. 5.17

$$\alpha_s^{(3)} = 0.390^{+0.053}_{-0.063}, \qquad \alpha_s^{(4)} = 0.364^{+0.044}_{-0.057}, \qquad \alpha_s^{\mathrm{PA}} = 0.328^{+0.026}_{-0.037}. \tag{5.19}$$

The error on α_s^{PA} is smaller by about a factor two than that on $\alpha_s^{(3)}$. This is due to the larger sensitivity $\mathrm{d}f^{\mathrm{PA}}/\mathrm{d}a = -4.7$ at $a = 0.1$ compared to that for the perturbation series up to third and fourth order of -2.3 and -2.8, respectively.

The coefficients of the perturbation series are known up to c_3 and the coefficient c_4 was estimated (Table 2.1) (p. 21). A more conservative approach is therefore to include the difference between the third order and the Padé result in the error on α_s. As discussed in Sect. 5.4.1 at low $Q^2 \simeq 3$ GeV^2 only the E-143 result for the Bjorken sum with an error of 0.019 should be used. This error may still be underestimated as far as the small-x extrapolation is concerned. Such a procedure yields an uncertainty in $\alpha_s(3\ \mathrm{GeV}^2)$ in the order of 0.12 corresponding to a probably more realistic error of

$$\delta\alpha_s(M_{\mathrm{Z}}^2) \simeq {}^{+0.012}_{-0.020}, \tag{5.20}$$

about four times larger than the one quoted in Eq. 5.18.

Table 5.4: Results for $\Delta\Sigma_{\rm inv}$ and corresponding values of Δs

experiment	target	$\Delta\Sigma_{\rm inv}$	Δs
SMC	deuteron	0.25 (8)	−0.11 (3)
E-143[b]	deuteron	0.30 (5)	−0.09 (2)
SMC	proton	0.27 (16)	−0.10 (5)
E-143[b]	proton	0.24 (10)	−0.11 (3)
SMC[a]	proton	0.21 (16)	−0.12 (5)
E-143[c]	proton	0.18 (10)	−0.13 (3)

For the superscripts see Table 5.2 (p. 76).

Also target-mass corrections [173] need to be considered which for the polarised case were studied in Ref. [174]. For the Bjorken sum they are related to $g_2^{\rm p}-g_2^{\rm n}$ and upper limits were given by Kawamura and Uematsu [175]. These limits correspond to an uncertainty in the Bjorken sum of 0.013 using the SMC $A_2^{\rm p}$ data only. With the new E-143 A_2 data and the SMC $A_2^{\rm d}$ data these limits need to be re-evaluated and target-mass effects will be smaller and maybe negligible.

In addition to the points raised above, there remains the question of consistency of the Q^2 evolutions of g_1 and of the Bjorken sum. On one hand the g_1 data are at best evolved in next-to-leading order involving Q^2 slopes of order α_s^2, on the other hand the Bjorken sum is evolved in order α_s^4 or higher when using the Padé estimate. Clearly the evolutions of Γ_1 obtained in the two ways are different. This must lead to a dependence of the extracted α_s value on the Q_0^2 value chosen for the evaluation of Γ_1. This problem was discussed by Chýla and Rameš [176] for the very similar case of the Gross–Llewelyn Smith sum rule [177], where the evolution of the structure function, xF_3, is known much better. From their (anti)neutrino-scattering data the CCFR collaboration finds for the Gross–Llewelyn Smith sum rule at $Q^2 = 3$ GeV^2 [178]

$$\int_0^1 F_3(x,Q^2)\,{\rm d}x = 2.50 \pm 0.018({\rm stat.}) \pm 0.078({\rm syst.}). \tag{5.21}$$

Including information from several other data sets and using correction up to $\mathcal{O}(\alpha_s^3)$ and a higher-twist contribution of -0.27 ± 0.14 GeV$^2/Q^2$ they obtain for the strong coupling constant [179],

$$\alpha_s(M_{\rm Z}^2) = 0.108 \pm^{0.003}_{0.005} \pm 0.004 \pm^{0.004}_{0.006}, \tag{5.22}$$

where the third error accounts for the uncertainty of higher-twist contribution. This corresponds to $\alpha_s(3\ {\rm GeV}^2) = 0.26 \pm^{0.02}_{0.03} \pm 0.02 \pm 0.03$.

5.5 The spin structure of the nucleon

The Ellis–Jaffe sum rules (Eq. 2.112, p. 21)

$$\Gamma_1^{\rm p,n}(Q^2) = \frac{1}{12}\left\{\pm g_a + \frac{1}{\sqrt{3}}a_8\right\} C^{\rm NS}(Q^2) + \frac{1}{9}\Delta\Sigma\, C^{\rm S}(Q^2) \tag{5.23}$$

were originally derived without the QCD corrections and assuming that the polarisation of the strange quarks vanishes, or — more precisely — that the nucleon matrix elements of the flavour-singlet and nonsinglet axial-vector currents are related by $\Delta\Sigma = \sqrt{3}a_8 = 3F - D$. The violation of the Ellis–Jaffe sum rules tells us that this relation does not hold. In turn one can now determine $\Delta\Sigma$ and thus Δs from the measurements of Γ_1. The results for $\Delta\Sigma_{\rm inv}$ (Eq. 2.106, p. 20) and Δs from the SMC and E-143 data are summarised in Table 5.4. They were evaluated with the same values for α_s, F/D, g_a, and n_f as used in Sect. 5.4.1. The value of $\Delta\Sigma$ at the Q^2 of the measurement can be obtained using $\Delta\Sigma(Q^2)/\Delta\Sigma_{\rm inv} = 1.08$ (1.06) for $Q^2 = 3$ GeV^2 (10 GeV^2).

The data from both experiments and from the proton and deuteron targets are in good agreement. The most significant results come from the deuteron data, which also have the advantage of being less sensitive to the assumptions made for the Q^2 evolution of the g_1 data. The flavour-singlet matrix element $\Delta\Sigma_{\rm inv}$ is small and the strange sea is negatively polarised

$$\Delta\Sigma_{\rm inv} \simeq 0.28 \pm 0.07 \qquad \text{and} \qquad \Delta s \simeq -0.10 \pm 0.03 \tag{5.24}$$

very much in line with the original findings of the EMC. The error given here also covers an estimated uncertainty of 0.06 due to the Q^2 evolution of the data, where the value for the proton data was taken as an upper limit to be conservative. The results of Eq. 5.24 imply

$$\Delta u = 0.77 \pm 0.03, \qquad \Delta d = -0.49 \pm 0.03, \qquad \Delta s = -0.10 \pm 0.03. \tag{5.25}$$

The negative value for Δs is supported by elastic (anti)neutrino scattering, $\nu p \to \nu p$, data [180]. The data corresponds to $\Delta s = -0.15 \pm 0.09$ [159].

The E-142 collaboration reported from their neutron data [23] a value of $\Delta\Sigma(Q^2) = 0.57 \pm 0.11$ at $Q^2 = 2$ GeV^2 corresponding to $\Delta\Sigma_{\rm inv} = 0.53$. Including QCD corrections up to $\mathcal{O}(\alpha_s^3)$ this values becomes $\Delta\Sigma_{\rm inv} = 0.47$, while the re-analysed data [169] yield $\Delta\Sigma_{\rm inv} = 0.31$ in good agreement with the results from the SMC and the E-143 experiment.

All new data confirm the EMC result that in the quark parton model interpretation the quarks contribute little to the nucleon spin. This still puzzling result led over the last eight years to many speculations of how to reconcile the parton-model expectation with the experimental results. The behaviour of g_1 for $x \to 0$ is now much more bound by the SMC data and early suggestions [181] that the Ellis–Jaffe sum rules may be accounted for at small x seem now very unlikely, in particular because the Bjorken sum rule is confirmed by the same data.

The validity of SU(3) flavour symmetry, needed to obtain a_8 from hyperon decay data, was questioned and discussed by many authors [52, 81, 182–187]. The direct contribution of a_8 to the first moment of g_1 is small. Therefore, a modification of a_8 primarily affects the Ellis–Jaffe prediction via the assumption, $\Delta\Sigma = \sqrt{3}a_8$. This implies that changing a_8 changes in the first place the expectation for $\Delta\Sigma$ rather than its value as derived from the measurements. If the expectation is made small enough, the Ellis–Jaffe sum rule is – of course – fulfilled, with the main difference that now $\Delta s \simeq 0$. For the central values given above a relative change in a_8 causes roughly half (double) that change with opposite sign in $\Delta\Sigma$ (Δs). Thus a small modification of a_8 due to SU(3) breaking mainly causes a redistribution of Δq between valence and sea quarks, keeping the sum, $\Delta\Sigma$, about constant. One proposal for a possible SU(3) breaking is to extrapolate the ratio F/D to zero mass difference of the initial and final hyperon in the weak decay [186]. The extrapolation used

yields $F/D = 0.40 \pm 0.07$ instead of 0.575 ± 0.016. With such a low value the Ellis–Jaffe predictions agree with the experimental results. This approach was criticised in Ref. [187] because it changes F/D strongly while keeping "miraculously" $F + D = g_a$ fixed. Apart from the neutron decay this combination also governs the decay $\Xi^- \to \Sigma^0 e\nu$, where SU(3) breaking as defined in Ref. [186] should be very large due to the mass differences involved.

The Skyrme model [188] of the nucleon implies in lowest order $\Delta\Sigma = 0$ [189] and the nucleon spin is carried by orbital angular momentum [159]. In this model the number of colours, N_c, is a free parameter and the results are obtained in the limit $N_c \to \infty$. In a model using a generalised Skyrme Lagrangian [190, 191] values of $\Delta\Sigma = 0.18$–0.32 can be accommodated.

Because of the axial anomaly (Sect. 2.12) it was suggested [74–76] that not $\Delta\Sigma$ as obtained above should be compared to the parton-model expectation, but the modified quantity (Eq. 2.123, p. 23)

$$\widetilde{\Delta\Sigma} = \Delta\Sigma(Q^2) + n_f \frac{\alpha_s(Q^2)}{2\pi} \Delta g(Q^2). \tag{5.26}$$

In the scale-independent quantity $\widetilde{\Delta\Sigma}$ the negative gluon contribution to $\Delta\Sigma(Q^2)$ due to the axial anomaly is added back. If $\widetilde{\Delta\Sigma}$ is interpreted as the fraction of the nucleon's spin carried by the quark spins, this fraction can again be equal to $3F - D$ and the entire violation of the Ellis–Jaffe sum rules can be attributed to the anomalous gluon contribution to Γ_1. This requires a large first moment of the polarised gluon distribution function of $\Delta g = 1.6$ and 2.5 for $Q^2 = 3$ GeV^2 and 10 GeV^2, respectively. Beyond leading order the separation of quark singlet and gluon contributions is in general ambiguous and can be redefined. However, there is no agreement [192] in the literature whether there is any advantage in using $\widetilde{\Delta\Sigma}$ over $\Delta\Sigma$.

The two options correspond to two renormalisation/factorisation schemes, which differ in the renormalisation prescription for γ_5. This is an additional ambiguity in the polarised case and both schemes correspond to the $\overline{\text{MS}}$ scheme in the unpolarised case. The physics pictures behind the two schemes differ in which soft gluon contributions are absorbed in the parton distribution functions [193, 194]. A discussion of the two pictures can also be found in Ref. [195]. Following Ref. [55] we will keep the notation $\overline{\text{MS}}$ for the scheme, where the singlet quark distribution corresponds to $\Delta\Sigma$, and refer to the scheme, where the quark singlet distribution corresponds to $\widetilde{\Delta\Sigma}$, as Adler–Bardeen scheme. The name is motivated by the Adler–Bardeen theorem [80] originally derived in the context of QED which states the scale independence of $\widetilde{\Delta\Sigma}$ to all orders.

In leading order there is no direct gluon contribution to Γ_1. In next-to-leading order the gluon contribution vanishes in the $\overline{\text{MS}}$ scheme because the first moment of the relevant coefficient function, C^g, vanishes. In the Adler–Bardeen scheme the gluon contribution is given by Eq. 5.26. There is a prescription of how to convert $\Delta\Sigma$ and Δg from one scheme to the other [55, 196]. It turns out that the first moment of the gluon distribution, Δg, is the same in both schemes and that only $\Delta\Sigma$ gets modified. As far as g_1 and Γ_1 are concerned all the schemes are on equal footing.

The key question is what to use in the helicity sum rule,

$$S_z = \frac{1}{2}\Delta\Sigma + L_q + \Delta g + L_g = \frac{1}{2}, \tag{5.27}$$

where $\Delta\Sigma$ and Δg denote the quark and gluon helicities and L_q and L_g their orbital angular momentum. Or maybe better: What are L_q and L_g in the two schemes? This

question was recently addressed by Ji *et al.* [197]. The authors derive a leading-order evolution equation for the quark and gluon orbital angular momenta, which couples them with each other and with the quark and gluon helicities. For $Q^2 \to \infty$ the solution yields asymptotic spin fractions carried by the quarks and gluons of

$$\begin{aligned} \Delta\Sigma + 2L_q &= \frac{3n_f}{16+3n_f} = 2J_q = 0.43 \\ 2\Delta g + 2L_g &= \frac{16}{16+3n_f} = 2J_g = 0.57, \qquad (n_f = 4) \end{aligned} \tag{5.28}$$

which are exactly the same as the asymptotic momentum fractions [39]. The authors argue that in next-to-leading order the anomalous gluon contribution to $\Delta\Sigma$ must be cancelled by a similar contribution to L_q with opposite sign and that J_q is anomaly free and invariant under such redefinitions. If the spin fractions given in Eqs. 5.28 are still valid at the scale where the experiments are performed, Q^2 = 3–10 GeV^2, we obtain from the result in Eq. 5.24 a value of $L_q = 0.075$.

The operator description of the gluon spin contribution to the nucleon spin was recently studied by Jaffe [198]. The author finds a significant *negative* contribution to Δg in contrast to what is expected in the anomaly interpretation of the sum rule violations.

To my knowledge the only proposal to access the orbital momentum of quarks experimentally is based on a semi-classical model, in which L_q leads to an azimuthal asymmetry in the distribution of hadrons produced by an unpolarised beam from a transversely polarised target [199]. The signal should show a periodicity with 2φ, where φ is the azimuth angle in the plane perpendicular to the momentum transfer. However, the azimuthal distribution of hadrons as obtained from an analysis of the hadronic tensor up to order $1/Q$ is very complicated [200] and involves terms periodic in φ, 2φ and 3φ.

5.6 QCD analyses of the g_1 data

After the complete next-to-leading order calculation of the two-loop splitting functions by Mertig and van Neerven [57] and by Vogelsang [58] three analyses of the g_1 data in the framework of the next-to-leading order Altarelli–Parisi equations (Eqs. 2.88, 2.89, p. 17) were published by Glück, Reya, Stratmann, and Vogelsang (GRSV) [201], by Gehrmann and Stirling (GS) [202], and by Ball, Forte, and Ridolfi (BFR) [55]. In two of them (GRSV, GS) the $\overline{\text{MS}}$ scheme was used and the BFR analysis was performed in the Adler–Bardeen scheme (AB), see Sect. 5.5. The parton distribution functions are parametrised at a starting scale Q_0^2, and their normalisation is contrained by the nonsinglet combinations

$$\begin{aligned} g_a = & \quad \Delta u - \Delta d & = 1.2573 \pm 0.0028, \\ 3F - D = & \quad \Delta u + \Delta d - 2\Delta s & = 0.579 \quad \pm 0.025. \end{aligned} \tag{5.29}$$

The asymptotic behaviour of the parton distribution functions [204] is used to fix some of the parameters. From the parton distribution functions evolved to Q^2 the prediction for each $g_1(x, Q^2)$ data point is calculated using Eq. 2.90 and the best set of parameters is obtained by minimising χ^2. All fits describe the data well and as an example the BFR fits to the proton and deuteron data are shown in Fig. 5.14. The curves show the fitted g_1 for 1 and 10 GeV^2 and for the Q^2 of the measurements for both, the SMC and E-143 data.

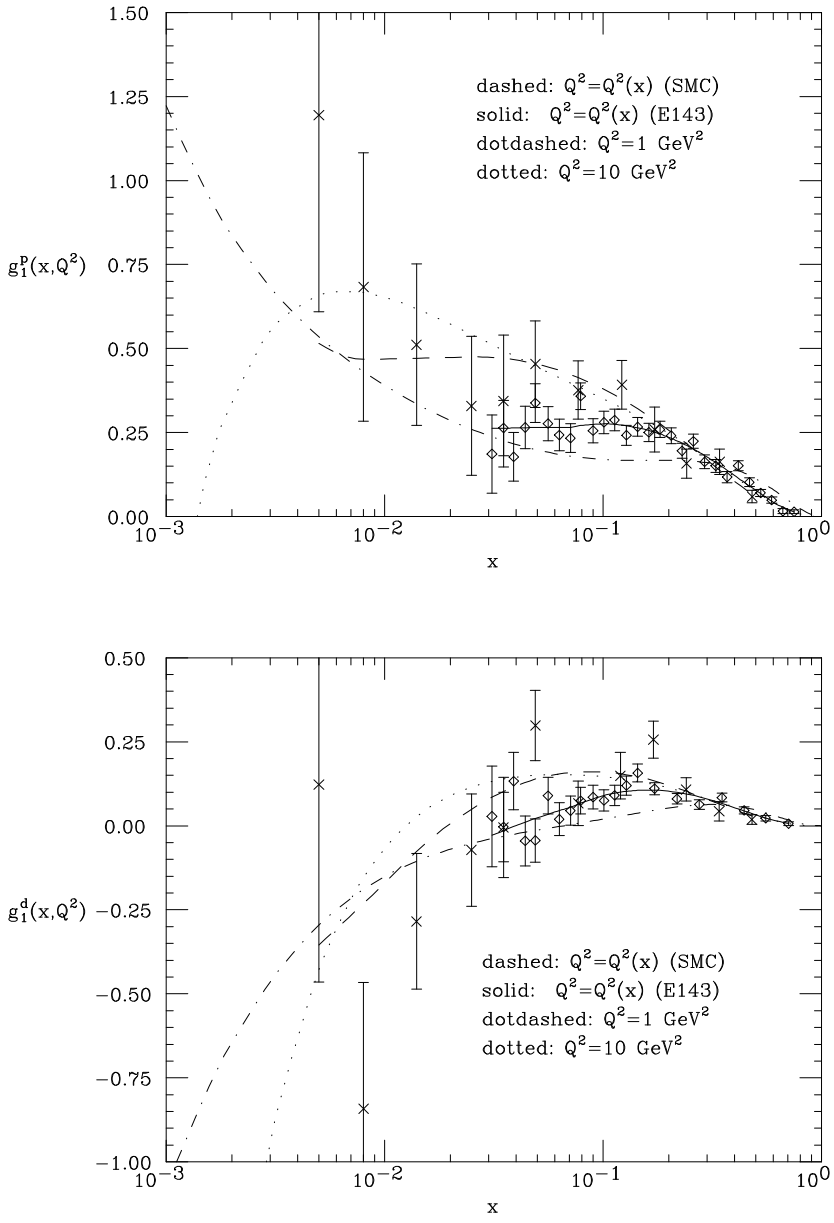

Figure 5.14: Next-to-leading order QCD analysis of the SMC and the E-143 proton (top) and deuteron data (bottom) [55].

Table 5.5: Results from NLO pQCD analyses

group	fit	Ref.	scheme	Q_0^2	Δg		data used
				GeV^2	Q_0^2	10 GeV^2	
GRSV	standard	[146]	$\overline{\text{MS}}$	0.34	0.2	0.9	all p,d,n
GS	Gluon B	[202]	$\overline{\text{MS}}$	4.0	1.6	1.9	all p,d,n
BFR		[55]	AB	1.0	1.5	2.8	SMC, E-143, p,d
BFR	Rome	[203]	AB	1.0	1.0	1.9	all p,d

The values for $\Delta g(10\ \text{GeV}^2)$ for GS and BFR were scaled from Q_0^2 with $\alpha_s(Q_0^2)/\alpha_s(10\ \text{GeV}^2)$.

Some characteristic parameters of the analsyses and the results for Δg are summarised in Table 5.5. In all analyses positive values for Δg are found, however the sensitivity to Δg is rather weak. Only for the BFR analysis an error on Δg is given. The original result is $\Delta g(Q_0^2) = 1.5 \pm 0.8$ and an extented analysis yields $\Delta g(Q_0^2) = 1.0 \pm 0.4$ [203], both for $Q_0^2 = 1\ \text{GeV}^2$. In the GRSV and GS analyses three quark distribution functions are fitted apart from $\Delta g(x)$, namely $\Delta u_\text{v}(x)$, $\Delta d_\text{v}(x)$, and $\Delta \bar{q}(x)$. In the BFR analysis only two, the singlet and nonsinglet quark distribution function, $\Delta q^\text{ns}(x)$ and $\Delta q^\text{s}(x)$, are fitted. The difference of the proton and neutron nonsinglet distribution functions as defined in Eq. 2.86 is only taken into account concerning different normalisations according to Eq. 5.29. However, the same x shape is assumed for both to limit the number of free parameters in view of the limited precision of the data. Assuming that the antiquark distribution functions are the same for all quark flavours, this leads to an unphysical relation between the up and down-quark valence distribution functions, $(2a+1)\Delta u_\text{v}(x) = -(2+a)\Delta d_\text{v}(x)$, where $a = -0.73$ is the ratio of the neutron and proton nonsinglet normalisations. If this can lead to an underestimate of the error of Δg has to be investigated.

In the GRSV and BFR analyses $\Delta\Sigma(Q_0^2)$, is determined in the fit, while it is fixed to the experimental value in the GS analysis. The results at $Q^2 = 10\ \text{GeV}^2$ are $\Delta\Sigma(Q^2) = 0.29$ (GRSV) and $\widetilde{\Delta\Sigma} = 0.5 \pm 0.1$ (BFR). The latter corresponds to $\Delta\Sigma = 0.14 \pm 0.10^{+0.12}_{-0.05}$, where the first error is statistical and the second accounts for theoretical uncertainties.[2] The rather low value is coming from the small values found for the first moments of g_1, which are

$$\begin{aligned} \Gamma_1^\text{p} &= 0.122 \pm 0.013^{+0.011}_{-0.005} && \text{proton} \\ \Gamma_1^\text{d} &= 0.025 \pm 0.013^{+0.012}_{-0.004} && \text{deuteron.} \end{aligned}$$

This is most likely due to the steep drop of g_1 at $Q^2 = 10\ \text{GeV}^2$ at small x, see Fig. 5.14. The first moments obtained in the GRSV analysis are 0.143 and 0.042 for the proton and the deuteron, respectively.

5.7 Semi-inclusive deep-inelastic scattering

The interest in semi-inclusive data is due to the fact that the produced hadron carries information on the flavour of the initially struck quark, particularly when it carries a large

[2] Note that in the notation of Ref. [55] (BFR) $\widetilde{\Delta\Sigma}$ is $\Delta\Sigma$ and $\Delta\Sigma$ is a_0.

fraction of the energy transfer, $z = E_h/\nu$. Presently the only semi-inclusive data are those from the SMC [22], apart from older EMC data [17] which were not analysed in terms of parton distribution functions. Only the fully inclusive process can be treated in the operator product expansion (Sect. 2.10). Therefore, the interpretation of the semi-inclusive data, where at least one hadron is observed, makes explicit use of the quark parton model. In the fragmentation process of a quark q into a hadron h, $q \to h$, hadrons containing the initial quark as valence quark are favoured. Therefore u and $\bar{\mathrm{d}}$ quarks preferentially fragment into positive pions while d and $\bar{\mathrm{u}}$ quarks fragment dominantly into negative pions. Combining data from proton and deuteron targets for the production of positive and negative pions the helicity distribution functions for up and down quarks and antiquarks can be determined. In the unpolarised case this can be done with high precision by combining data from charged-lepton and from charged-current neutrino scattering. Because neutrino experiments require targets of several hundred tons no such experiments can be performed in the polarised case and semi-inclusive data provide presently the only direct information on the valence-quark helicity distribution functions, $\Delta q_v(x) = \Delta q(x) - \Delta\bar{q}(x)$. At high momentum transfers charged-current events can be studied in ep collisions at HERA. With a polarised proton beam and high luminosity the parity violating structure functions could be studied there, see Sect. 6.2.

The differential cross section for the production of hadrons factorises and can in the quark parton model be written in the terms of the parton distribution and the fragmentation functions, $q(x, Q^2)$ and $D_q^h(z, Q^2)$. The latter is related to the probability for a quark q to fragment into a hadron, h, carrying the fraction z of the quark's energy, which is taken to be the energy transfer ν. For charged hadrons, which were studied in the SMC analysis, we obtain

$$\frac{1}{\sigma^\mu}\frac{\mathrm{d}\sigma^\pm}{\mathrm{d}z} = \frac{1}{N^\mu}\frac{\mathrm{d}N^\pm}{\mathrm{d}z} = \frac{\sum_q e_q^2\, q(x,Q^2)\, D_q^{h^\pm}(z,Q^2)}{\sum_q e_q^2\, q(x,Q^2)}, \tag{5.30}$$

where $N^\pm$ is the number of produced hadrons, N^μ the is the number of deep-inelastic events, and $\sigma^\pm$ and σ^μ are the corresponding differential cross sections. The sums run over $q = \mathrm{u}, \mathrm{d}, \mathrm{s}, \bar{\mathrm{u}}, \bar{\mathrm{d}}, \bar{\mathrm{s}}$ and e_q are the quark charges. The fragmentation function, $D_q^{h^\pm}$, accounts for the fragmentation into positive and negative hadrons, respectively. In the SMC analysis contributions from pions, kaons, and protons and their antiparticles were considered.

The asymmetries obtained in the SMC analysis [22] for the production positive and negative hadrons from proton and deuteron targets are shown in Fig. 5.15. In the quark parton model these asymmetries are given by

$$A_1^\pm(x,Q^2) = \frac{\sum_q e_q^2 \Delta q(x,Q^2) D_q^\pm(Q^2)}{\sum_q e_q^2 q(x,Q^2) D_q^\pm(Q^2)}, \tag{5.31}$$

where $D_q^\pm(Q^2) = \sum_{h^\pm} \int_{z_{min}}^1 D_q^{h^\pm}(z,Q^2)\mathrm{d}z$ with $z_{min} = 0.2$ in the SMC analysis. The fragmentation functions in Eq. 5.31 are the same for the polarised and unpolarised case, provided the final state hadrons are spinless or it is summed over their spin orientations. These functions were measured by the EMC for up and down quarks fragmenting into charged pions, kaons, and protons [205]. The only substantial contributions to the sums in Eq. 5.31 arise from the fragmentation of light quarks into pions.

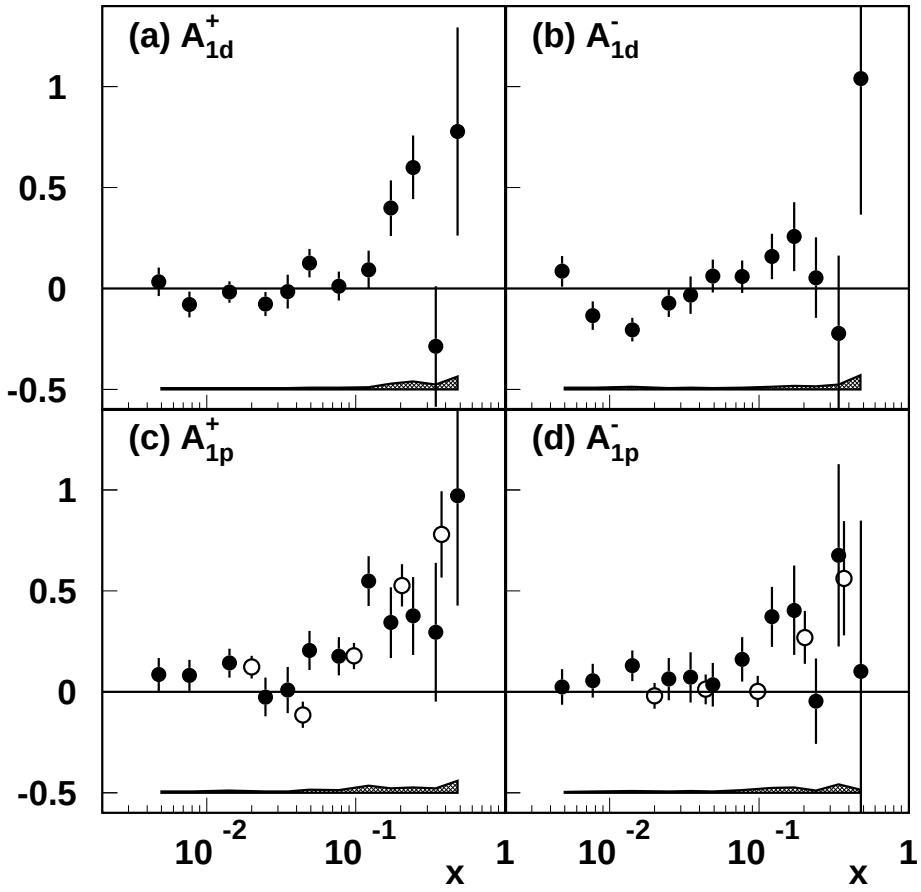

Figure 5.15: Virtual-photon asymmetries for the production of charged hadrons, $A_1^{\pm}$, as a function of x, for (a,c) positive and (b,d) negative hadrons from (c,d) proton and (a,b) deuteron targets. The data are from the SMC (full circles) [22] and the EMC (open circles) [17]. Statistical errors are shown on the data points and systematic errors for the SMC data are indicated by the shaded areas.

The quark helicity distribution functions are determined from the measured hadron asymmetries, Eq. 5.31, and and the inclusive asymmetries

$$A_1(x,Q^2) = \frac{\sum_q e_q^2 \Delta q(x,Q^2)}{\sum_q e_q^2 q(x,Q^2)}. \tag{5.32}$$

The correlation between the data sets is taken into account in the SMC analysis. For the unpolarised quark distribution functions the parametrisations of the Durham group [206] and the Dortmund group [207] are used to estimate the uncertainty. The results given here refer to the Durham parametrisation. The quark distributions and the fragmentation functions are evaluated for $Q^2 = 10$ GeV^2 and it is assumed that the asymmetries do not depend on Q^2. In principle all six quark and antiquark helicity distributions can be determined from the six measured asymmetries for positive and negative hadrons from proton and deuteron targets plus the two inclusive asymmetries. However, the sensitivity

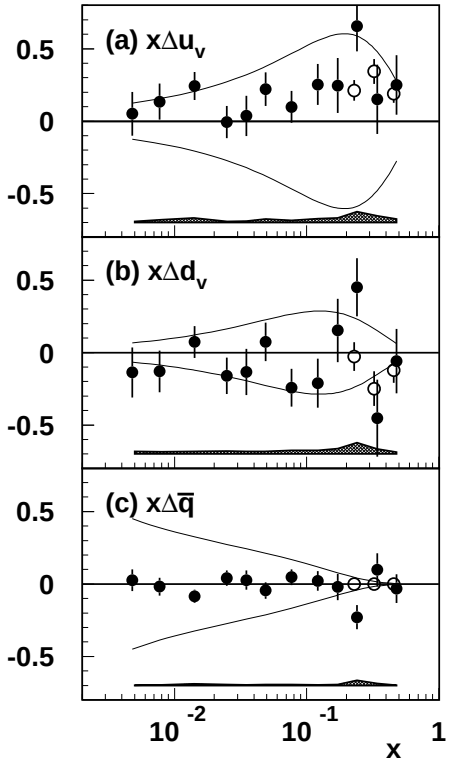

Figure 5.16: SMC results for $x\Delta q(x)$ as a function of x at $Q^2 = 10$ GeV^2 for (a) the up valence quarks, (b) the down valence quarks, (c) the light sea quarks (see text).

to the strange quark and antiquark distribution functions is very weak and they are therefore fixed in the analysis. Their shape is assumed to be equal to that of the unpolarised distribution functions and the normalisation is taken from the analysis of the Ellis–Jaffe sum using the inclusive data, $\int_{0.003}^{0.7}(\Delta s + \Delta\bar{s})\mathrm{d}x = -0.12$. In addition the light-antiquark distribution functions are assumed to be equal, $\Delta\bar{q}(x) := \Delta\bar{u}(x) = \Delta\bar{d}(x)$. This is necessary because of the limited statistics of the data and may be released in a future analysis including the SMC data from the 1995 deuteron and 1996 proton experiments. From the violation of the Gottfried sum rule [10, 208] and the result from Drell–Yan dimuon production [209] it is well known that this assumption is unjustified in the unpolarised case.

The SMC results for the valence-quark and antiquark helicity distribution functions, $\Delta q_v(x)$ and $\Delta\bar{q}(x)$, are shown in Fig. 5.16 for $Q^2 = 10$ GeV^2. The polarisations of the valence quarks are within the statistical accuracy independent of x and amount to

$$\frac{\Delta u_{\mathrm{v}}(x)}{u_{\mathrm{v}}(x)} = 0.5 \pm 0.1, \qquad \frac{\Delta d_{\mathrm{v}}(x)}{d_{\mathrm{v}}(x)} = -0.6 \pm 0.2. \tag{5.33}$$

As expected in the constituent quark model the polarisation of the up valence quarks is positive and that of the down valence quarks is negative. The polarisation of the light-quark sea is compatible with zero. Also shown as solid lines are the limits from

the unpolarised parton distributions, $|\Delta q(x)| \leq q(x)$. The open points at large x are obtained when the antiquark distributions are set to zero for $x > 0.2$. For these points the systematic error covers the range $\Delta q(x) = \pm q(x)$.

The valence-quark helicity distribution functions can also be determined from an asymmetry constructed from the differences of the cross sections for the production of positive and negative hadrons [210]. The advantage of this method is that the fragmentation functions cancel and that the asymmetry only depends on the valence quarks. However, an experimental problem is that the sightly different spectrometer acceptances for negative and positive hadrons do not cancel in these asymmetries. These acceptances were studied in dedicated runs with opposite-sign beam muons and reversed spectrometer-magnet field. The semi-inclusive data were also analysed using the method of Ref. [210] and the results from both methods agree. A direct comparison is shown in Ref. [22].

To evaluate the contribution of the valence quarks to the nucleon spin the helicity distribution functions must be integrated over the entire x range, $\Delta q = \int_0^1 \Delta q(x) \mathrm{d}x$. Outside the measured region $0.003 \leq x \leq 0.7$ the polarisation of the valence quarks, $\Delta q_{\mathrm{v}}(x)/q\mathrm{v}(x)$ was assumed to be constant, while for the sea quarks $\Delta\bar{q}(x)$ was assumed to be constant. Only the extrapolations to $x \to 0$ give sizable contributions to the first moments amounting to 0.11 ± 0.11, -0.06 ± 0.06, and 0 ± 0.02 for Δu_v, Δd_v, and $\Delta\bar{q}$, respectively. The results for the entire x region are

$$\begin{aligned} \Delta u_v &= 1.01 \pm 0.19 \pm 0.14 \\ \Delta d_v &= -0.57 \pm 0.22 \pm 0.11 \\ \Delta\bar{u} = \Delta\bar{d} &= -0.02 \pm 0.09 \pm 0.03. \end{aligned} \tag{5.34}$$

Assuming that the first moments for up, down, and strange antiquarks are equal, one obtains $2\Delta\bar{q}(x) = \Delta s + \Delta\bar{s} = -0.10$. Within the error margins this relation is fulfilled. Note that this analysis does not make explicit use of the matrix elements obtained from hyperon decays and of SU(3) flavour symmetry apart from how the normalisation of the strange quark distribution functions is fixed.

In the quark parton model we have the relation

$$\begin{aligned} g_1^{\mathrm{p}}(x) - g_1^{\mathrm{n}}(x) &= \frac{1}{6}\left\{\Delta u(x) - \Delta d(x)\right\} \\ &= \frac{1}{6}\left\{\Delta u_{\mathrm{v}} - \Delta d_{\mathrm{v}}\right\} + \frac{1}{3}\left\{\Delta\bar{u}(x) - \Delta\bar{d}(x)\right\}. \end{aligned} \tag{5.35}$$

Assuming isospin symmetry for the quark sea, $\Delta\bar{u}(x) = \Delta\bar{d}(x)$, as in the present analysis of the semi-inclusive data the last term vanishes and we obtain a relation between the structure functions and the valence distribution functions. To compare the two quantities the SMC repeated the analysis of the semi-inclusive data without using the inclusive asymmetries. The two analyses shown in Fig. 5.17 are in good agreement demonstrating the internal consistency of the two methods.

The question of how the anomaly contributes in semi-inclusive scattering was addressed in Ref. [211]. Theoretically the situation is unclear and arguments exist for an unchanged contribution as well as for a suppression of the anomalous contribution in the semi-inclusive channel. The SMC results are compatible with both scenarios. In the future the HERMES experiment will contribute precise data for $0.01 < x$ to this kind of studies. Lower x values can be reached with high precision by the COMPASS experiment (Sect. 6.1).

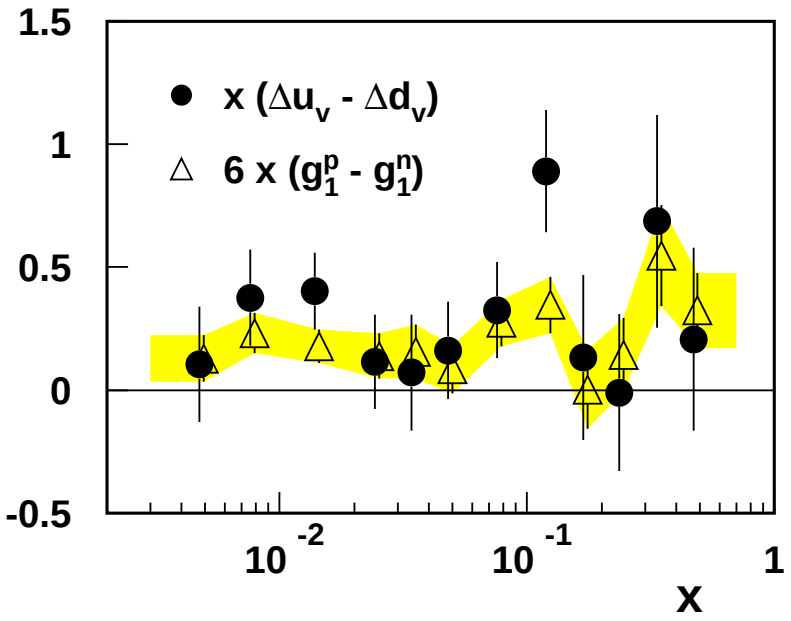

Figure 5.17: The difference $6x\{g_1^{\rm p}(x) - g_1^{\rm n}(x)\}$ from inclusive asymmetries and $x\{\Delta u_{\rm v} - \Delta d_{\rm v}\}$ from semi-inclusive asymmetries from the SMC data. Only statistical errors are shown.

5.8 Results from lattice gauge theory

A successful theory of strong interactions must eventually be able to predict such fundamental quantities as structure functions and their moments from first principles. Such an attempt is made in lattice gauge theories [212]. Considerable progress has been made in the last years partly due to the developments in computer technology. Now reliable calculations of the moments of structure functions begin to emerge. Recently, three groups from Germany [213], Japan [213], and Kentucky [214] published results for the axial charge, $\Delta\Sigma$. They obtain $\Delta\Sigma = 0.18 \pm 0.02$ [213], 0.18 ± 0.10 [215], and 0.25 ± 0.10 [214], respectively. The agreement between the calculations and with the experimental value of 0.28 ± 0.07 is remarkable. The first and the two latter calculations use different methods. Recently, a partial calculation of $\Delta\Sigma$ by the German group using a similar technique as in Refs. [214, 215] became available [216]. In the following we refer to these results. The calculations were performed in so-called "quenched" QCD neglecting internal quark loops [214, 215]. Typical parameters are a lattice size of $16^3 \times 20$ and a lattice spacing of $a = 0.14$ fm [215]. The relevant scale is a^{-2}. The results for the chiral limit, $m_q = 0$, are extrapolated from calculations for several quark masses around 100–300 MeV. The heavier strange quark is treated separately. The German group used a somewhat larger lattice in the time coordinate, $16^3 \times 32$ [216]. However, in this work only the contributions from operators directly coupled to the valence quarks in the nucleon (connected part) were calculated. The calculation of the disconnected part related to sea quarks is in progress. The results from the three groups are in good agreement and are summarised in Table 5.6. It is found that the connected part reproduces about the value expected for $\Delta\Sigma$ from the Ellis–Jaffe sum rule, while the disconnected part is responsible for the small total value of

Table 5.6: Results from lattice QCD for the axial charges.

Part	Ref.	Δu		Δd		Δs		$\Delta\Sigma$	
conn.	[216]	0.83	(7)	−0.24	(2)	–		0.59	(7)
conn.	[215]	0.76	(4)	−0.23	(2)	–		0.53	(4)
disc.		−0.12	(4)	−0.12	(4)	−0.11	(3)	−0.35	(4)
total		0.64	(5)	−0.35	(5)	−0.11	(3)	0.18	(10)
conn.	[214]	0.91	(11)	−0.30	(11)	–		0.62	(9)
disc.		−0.12	(1)	−0.12	(1)	−0.12	(1)	−0.37	(3)
total		0.79	(11)	−0.42	(11)	−0.12	(1)	0.25	(12)
Experiment		0.77	(3)	−0.49	(3)	−0.10	(3)	0.28	(7)

$\Delta\Sigma$.

The axial vector coupling constant, $g_a^{\mathrm{n}\to\mathrm{p}} = F + D = \Delta u - \Delta d$, is often difficult to reproduce in lattice QCD. This nonsinglet combination should receive no or only small contributions from the disconnected part. The values obtained by the three groups are 1.07 ± 0.09 [216], 0.985 ± 0.025 [215], and 1.20 ± 0.11 [217]. The first two fall short of the experimental value 1.2573 ± 0.0028 [51], while the result from the Kentucky group is only 4 % below. This calculation also gives the $\Delta\Sigma$ value closest to the experimental result. The results of the German group for the higher moments of g_1 and g_2 are discussed in the context of higher-twist effects in Sect. 5.9.

Recently a calculation of the tensor charge, $\delta\Sigma$

$$2(S_\mu P_\nu - S_\nu P_\mu)\delta\Sigma = \langle P,S|\bar{\psi} i\sigma_{\mu\nu}\gamma_5\psi|P,S\rangle, \tag{5.36}$$

was reported [218]. The tensor charge is given by the difference of the first moments of the transversity structure function, h_1, for quarks and antiquarks. Gluon operators do not contribute to h_1 in any order and the tensor charge is therefore anomaly free. The lattice calculation shows a large value for the tensor charge

$$\delta\Sigma(Q^2) = 0.56\ (13) \qquad \text{compared to} \qquad \Delta\Sigma(Q^2) = 0.18\ (10), \tag{5.37}$$

at $Q^2 = 3$ GeV^2. This is an interesting result in view of the measurements of h_1 foreseen for HERMES and proposed by the COMPASS collaboration at CERN and the RHIC spin collaboration at Brookhaven.

5.9 Higher-twist contributions to the first moments

In addition to the QCD corrections given by the perturbative series also higher-twist contributions proportional to $1/Q^{2n}$ must be considered for the Ellis–Jaffe and Bjorken sum rules. There are in principle two kinds of such power contributions, which appear in the Bjorken sum rule like

$$\Gamma_1^{\mathrm{n}} - \Gamma_1^{\mathrm{n}} = \frac{g_a}{6}\left(1 - \frac{\alpha_s(Q^2)}{\pi} + \cdots \pm \frac{C^{\mathrm{R}}}{Q^2}\right) + \frac{C^{\mathrm{HT}}}{Q^2} + \mathcal{O}\left(\frac{M^4}{Q^4}\right), \tag{5.38}$$

Table 5.7: Higher twist reduced matrix elements

	Ref.	$a^{(2)} \times 10^3$ proton	deuteron	Bjorken	$d^{(2)} \times 10^3$ proton	deuteron	Bjorken
E-143	[27]	24.2 (2.0)	8.0 (1.6)	31 (5)	5.4 (5.0)	3.9 (9.2)	2 (22)
sum	[219]				−3 (3)	−13 (5)	22 (10)
rules	[220]				−6 (3)	−17 (5)	26 (10)
lattice	[216]	30 (6)	13 (4)	33 (8)	−48 (5)	−24 (3)	−44 (6)
bag	[147]				6	2.9	6
models	[221]	59	27	59	21	10	21
	[149]	21.0	8.7	6	17.4	6.8	6
	[222, 223]				10	5	9
					$f^{(2)} \times 10^3$		
sum	[219]				−49 (10)	−18 (10)	−60 (10)
rules	[224]				−37 (6)	−23 (6)	−23 (7)
bag m.	[221]				35	16	35

with the nucleon mass M. The term with C^{R} arises from ambiguities in the summation of the perturbative series and is often referred to as "renormalon ambiguity". This ambiguity must be cancelled in the physical result by a corresponding ambiguity in the second term involving C^{HT}. The latter describes "genuine" higher-twist effects arising from parton-parton correlations in the nucleon, while C^{R} is target independent. In a recent review by Braun [172] the size of the two terms was estimated to $(g_a/6)C^{\mathrm{R}} = 0.004$–$0.015$ GeV^2 and $C^{\mathrm{HT}} = -0.015 \pm 0.010$ GeV^2 with the conclusion that the "true" higher-twist effects are about a factor of two larger than the renormalon ambiguity. A quite different value of $(g_a/6)C^{\mathrm{R}} = 0.040 \pm 0.016$ GeV^2 was reported in Ref. [171]. Thus the estimates for the size of the "true" higher-twist effects are in the order of the renormalon ambiguities. The difference between the third and fourth order correction to the Bjorken sum rule evaluated at 3 GeV^2 corresponds to 0.008 GeV^2 more in line with the smaller value given by Braun. In the remaining part of this section, we focus on the genuine higher-twist term, C^{HT}.

Neglecting perturbative QCD corrections, the first moment of g_1 is given by the operator product expansion in the form [225, 226]

$$\Gamma_1(Q^2) = \frac{1}{2}a^{(0)} + \frac{1}{9}\left\{a^{(2)} + 4d^{(2)} + 4f^{(2)}\right\}\frac{M^2}{Q^2} + \mathcal{O}\left(\frac{M^4}{Q^4}\right). \tag{5.39}$$

The matrix elements a, d, and f, refer to operators of twist two, three, and four, respectively. Two of them, a and d, are related to moments of g_1 and g_2 by

$$\int_0^1 g_1(x, Q^2)\,\mathrm{d}x = \frac{1}{2}a^{(0)}, \tag{5.40}$$

$$\int_0^1 x^2 g_1(x, Q^2)\,\mathrm{d}x = \frac{1}{2}a^{(2)}, \tag{5.41}$$

$$\int_0^1 x^2 g_2(x, Q^2)\,\mathrm{d}x = \frac{1}{3}\left(d^{(2)} - a^{(2)}\right), \tag{5.42}$$

ignoring terms of $\mathcal{O}(M^2/Q^2)$. These formulæ can be obtained from Eqs. 2.108 and 2.109 (p. 20) with $h^{(n)} = \sum_i \varepsilon_i h^i_{n+1}$ for $h = a, d$. No such relation is known for $f^{(2)}$. It is interesting to note that $d^{(2)}$ corresponds to the twist-3 part, $\overline{g}_2$, of g_2,

$$\int_0^1 x^2 \overline{g}_2(x, Q^2)\,\mathrm{d}x = \frac{1}{3} d^{(2)}, \tag{5.43}$$

and $a^{(2)}$ corresponds to the Wandzura–Wilczek contribution (Eq. 2.118). Usually twist-3 contributions appear on top of large twist-2 contributions. The case of g_2, where a twist-3 part can directly be determined from the difference of measurable quantities, $g_2 - g_2^{\mathrm{ww}}$, is probably unique.

The matrix element, $a^{(2)}$ and $d^{(2)}$ were recently determined from the E-143 measurements of g_2^{p} and g_2^{d} [27], see Sect. 5.3.1. These results are summarised in Table 5.7 together with calculations using QCD sum rules [219,220,224], bag models [147,149,221], and lattice QCD [216]. The predictions for $d^{(2)}$ and $f^{(2)}$ vary widely and opposite signs are obtained from QCD sum rules and lattice QCD on one hand and from bag models on the other hand. Bag models are based on the movement of single quarks in a mean-field. It has been questioned [227] that such models can give reliable predictions for matrix elements related to quark-gluon correlations like $d^{(2)}$. The QCD-based methods, QCD sum rules and lattice QCD, should *a priori* be in a much better position to describe parton correlations. Therefore it is to some extend surprising that the data favour positive values of $d^{(2)}$ as predicted in the bag models. The large negative lattice-QCD value of $d^{(2)} = -0.048$ for the proton can be excluded. This result was obtained in a quenched calculation not containing possible contributions from "disconnected" diagrams corresponding to sea quarks, which might reduce the result. The predictions from lattice QCD for $a^{(2)}$ are in good agreement with the measurements.

To estimate the possible correction of the Bjorken sum rule, we combine the experimental result for $a^{(2)}$ with the predictions from those calculations, where also the twist-4 term, $f^{(2)}$, is available. From the QCD sum rule calculation of Braun *et al.* [219] and that of Stein *et al.* [220, 224], and the MIT bag model result of Ji and Unrau [221] we obtain $C_{\mathrm{Bj}}^{\mathrm{HT}} = -0.012, 0.003, 0.023$ GeV^2, respectively. Thus the present status of higher-twist corrections to the Bjorken sum rule can be summarised as

$$\Delta^{\mathrm{HT}}\Gamma_{\mathrm{Bj}} = \frac{C_{\mathrm{Bj}}^{\mathrm{HT}}}{Q^2} = \frac{0.004 \pm 0.020 \text{ GeV}^2}{Q^2}, \tag{5.44}$$

where the central value comes from the experimental results ignoring the contribution of $f^{(2)}$. The experimental value for $d_{\mathrm{Bj}}^{(2)}$ is compatible with the three predictions used to obtain the estimate in Eq.5.44 and thus does not further limit the uncertainty of $C_{\mathrm{Bj}}^{\mathrm{HT}}$. For $Q^2 = 3$ GeV^2 the uncertainty due to higher-twist contributions is in the order of one third of the present experimental error.

When applying higher-twist corrections to sum rules it is unclear which value of Q^2 should be used. Experimentally the structure functions are measured at different Q^2 for each value of x. Therefore, the x dependence of higher-twist corrections is needed in principle to correct the data. It does not make sense to apply a higher-twist correction evaluated at e.g. 3 GeV^2 to the high-x data, which were taken in the E-143 experiment at 9 GeV^2, or the small-x data taken at 1.3 GeV^2. The subsequent evolution of the data to 3 GeV^2 does not take into account higher-twist effects. For the spin-averaged structure

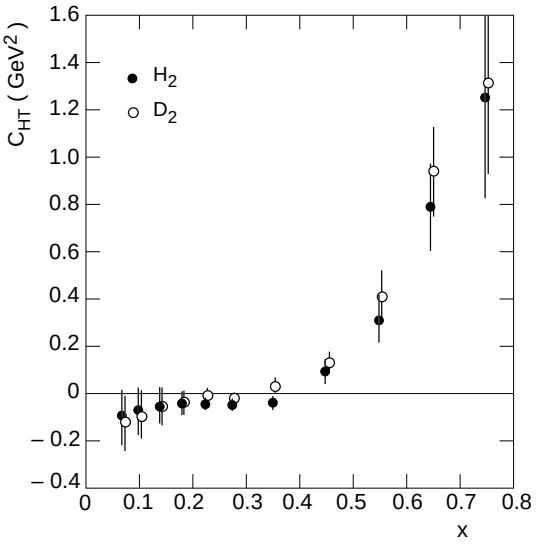

Figure 5.18: Higher-twist coefficients, c, for F_2 of the proton and the deuteron as a function of x from the BCDMS and SLAC data [228].

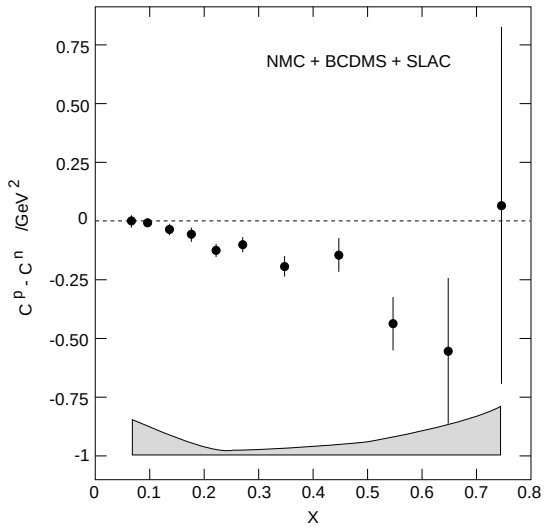

Figure 5.19: Difference of the higher-twist coefficients, $c^{\mathrm{p}} - c^{\mathrm{n}}$, for F_2 of the proton and the neutron as a function of x from the NMC, BCDMS and SLAC data [124].

function, F_2, a separation of perturbative and $1/Q^2$ scaling violations was attempted in a common analysis [228] of the BCDMS and SLAC F_2 data using the following form

$$F_2(x, Q^2) = \widehat{F}_2(x, Q^2) \left(1 + \frac{c(x)}{Q^2}\right), \tag{5.45}$$

where $\widehat{F}_2$ accounts for next-to-leading order perturbative Q^2 evolution and target mass corrections. The resulting parameters, $c(x_i)$, for each x bin are shown in Fig. 5.18. Large effects are observed at large x. However, this rise with x is partly due to the parametrisation in Eq. 5.45. The relative importance of the higher-twist contributions increases due to the drop of F_2. The difference, $c^{\mathrm{p}} - c^{\mathrm{n}}$, of the proton and neutron higher-twist contributions was studied by the NMC [124] using their data for the structure function ratio $F_2^{\mathrm{n}}/F_2^{\mathrm{p}}$ together with data from SLAC and BCDMS. The result of this analysis in shown in Fig. 5.19. Using these results the higher-twist contribution to the Gottfried sum rule [229]

$$S_G = \int \frac{F_2^{\mathrm{p}} - F_2^{\mathrm{n}}}{x}\,\mathrm{d}x = \frac{1}{3}\int_0^1 (u_{\mathrm{v}} - d_{\mathrm{v}})\,\mathrm{d}x + \frac{2}{3}\int_0^1 (\bar{u} - \bar{d})\,\mathrm{d}x, \tag{5.46}$$

was studied, which is equal to 1/3 for two up and one down valence quark and an isospin-symmetric quark sea, $\bar{u} = \bar{d}$. The experimental is result is $S_G(4\ \mathrm{GeV}^2) = 0.235 \pm 0.026$ [208]. The difference of the higher-twist contributions from the proton and the neutron amounts to 0.01, which is a 5 % effect.

Chapter 6

Prospects of future experiments

Several new experiments were proposed to further investigate the spin structure of the nucleon. The emphasis is on the polarisation of the gluons and on the transversity structure function h_1. A key issue is high luminosity. Apart from the RHIC spin programme at Brookhaven, which is approved, the COMPASS project at CERN is most advanced. A polarisation of the HERA proton beam would open up a new kinematic domain of spin physics, provided an integrated luminosity larger than 100 pb^{-1} can be reached.

6.1 The COMPASS experiment at CERN

An unambiguous determination of the gluon polarisation, Δg, can only be obtained from a process involving the gluon in leading-order. Such a process receives corrections in next-to-leading order proportional to $\alpha_s \Delta q$, which vanish for $Q^2 \to \infty$. A particularly clean such case is charm production, where in leading order only the photon-gluon fusion process, shown in Figs. 6.1 and 6.2, contributes. Quark contributions can be neglected because there is no or only a small intrinsic charm quark content in the nucleon. The interpretation of data from open charm production [230–233] is more direct than that of data from J/ψ production. In the latter a model for the formation of the ($\mathrm{c\bar{c}}$) colour-singlet state must be assumed, see analyses in Refs. [155, 234, 235] and references therein.

In this section we discuss a measurement of the cross-section asymmetry for open charm muoproduction proposed at CERN based on the identification of D^0 mesons via their $\mathrm{D} \to \mathrm{K}\pi$ decay channels. The COMPASS experiment will also provide high statistics data for g_1, semi-inclusive muon scattering, and for the third twist-2 nucleon structure function, h_1, often called transversity. The experiment is on the level of a proposal and was favourably discussed by the programme committee. If approved later this year, measurements could start in 1999.

6.1.1 Open charm leptoproduction

For real or quasi-real photons the charm-production cross section for the photon-gluon fusion process, $\gamma\mathrm{g} \to \mathrm{c\bar{c}}$, can be written as

$$\sigma^{\gamma \mathrm{g} \to \mathrm{c\bar{c}}} = \sigma(\hat{s}) + \lambda_\gamma \lambda_\mathrm{g} \Delta\sigma(\hat{s}), \tag{6.1}$$

where $\hat{s} = (q+k)^2$ is the energy squared and $\lambda_{\gamma,\mathrm{g}}$ are the helicities in the photon-gluon c.m. system (Fig. 6.2). The spin-averaged part, $\sigma(\hat{s})$, and the spin-dependent part, $\Delta\sigma(\hat{s})$,

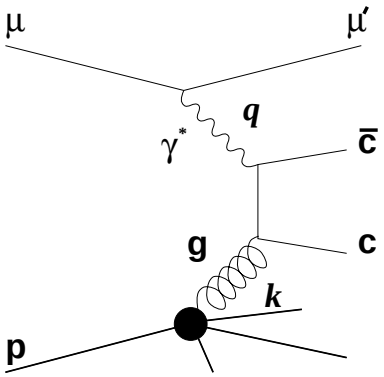

Figure 6.1: The photon-gluon fusion diagram

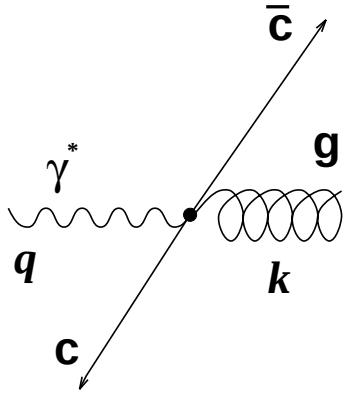

Figure 6.2: Photon-gluon fusion in the photon-gluon c.m. system

are given in leading order by [230, 231]

$$\begin{aligned}\Delta\sigma(\hat{s}) &= \frac{4}{9}\frac{2\pi\alpha_e\alpha_s(\hat{s})}{\hat{s}}\left\{3\beta - \ln\frac{1+\beta}{1-\beta}\right\},\\ \sigma(\hat{s}) &= \frac{4}{9}\frac{2\pi\alpha_e\alpha_s(\hat{s})}{\hat{s}}\left\{-\beta(2-\beta^2) + \frac{1}{2}(3-\beta^4)\ln\frac{1+\beta}{1-\beta}\right\},\end{aligned} \tag{6.2}$$

where $\beta = \sqrt{1-4m_c^2/\hat{s}}$ is the c.m. velocity of the charmed quarks and antiquarks. Both terms, σ and $\Delta\sigma$, rise sharply at the threshold, $\hat{s} = 4m_c^2$, and $\Delta\sigma$ changes sign at about four times the threshold (Fig. 6.3). For the discussion below we assume a charm-quark mass of $m_c = 1.5$ GeV and use the parametrisation of the polarised gluon distribution function, $\Delta g(x)$, from Gehrmann and Stirling [236] (set B). From coherence arguments [204] it is expected that the gluon polarisation behaves like $\Delta g(x)/g(x) \propto x$ for $x \to 0$. Such a behaviour is used in most parametrisations of the polarised gluon distribution function. Therefore, $\Delta g/g$ is expected to be large only at rather large values of x. For $x \geq 0.15$ the gluon polarisation can be as large as 0.5. A collection of polarised parton distribution functions can be found in Ref. [237].

The photon-nucleon cross-section asymmetry, $A_{\gamma N}^{c\bar{c}}$, for the process $\gamma N \to c\bar{c}$ is obtained by integrating the cross sections over $x_g^{\min} \leq x_g \leq 1$

$$A_{\gamma N}^{c\bar{c}}(\nu) = \frac{\Delta\sigma^{\gamma N\to c\bar{c}X}}{\sigma^{\gamma N\to c\bar{c}X}} = \frac{\int_{4m_c^2}^{2M\nu} \mathrm{d}\hat{s}\,\Delta\sigma(\hat{s})\,\Delta g(x_g,\hat{s})}{\int_{4m_c^2}^{2M\nu} \mathrm{d}\hat{s}\,\sigma(\hat{s})\,g(x_g,\hat{s})}. \tag{6.3}$$

Here $x_g = \hat{s}/2M\nu$ denotes the nucleon momentum fraction carried by the gluon, which in this process is different from the kinematic variable, $x = Q^2/2M\nu$. Large photon energies, ν, correspond to small $x_g^{\min} = 4m_c^2/2M\nu$. Due to the rise of the unpolarised gluon distribution function towards small x_g and the change-over in sign of $\Delta\sigma(\hat{s})$ (Fig. 6.3) the asymmetry $A_{\gamma N}^{c\bar{c}}$ drops with increasing ν (Fig. 6.4). To obtain a large asymmetry a large

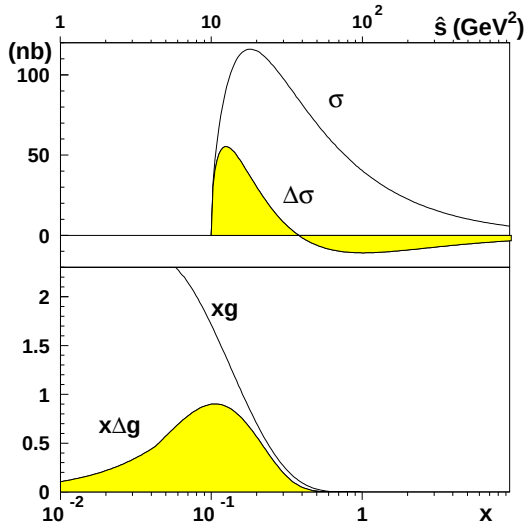

Figure 6.3: The photon-gluon cross sections, σ and $\Delta\sigma$, as a function of $\hat{s}$ (top) and the gluon distribution functions, xg and $x\Delta g$, as a function of $x = x_{\mathrm{g}}$ (bottom).

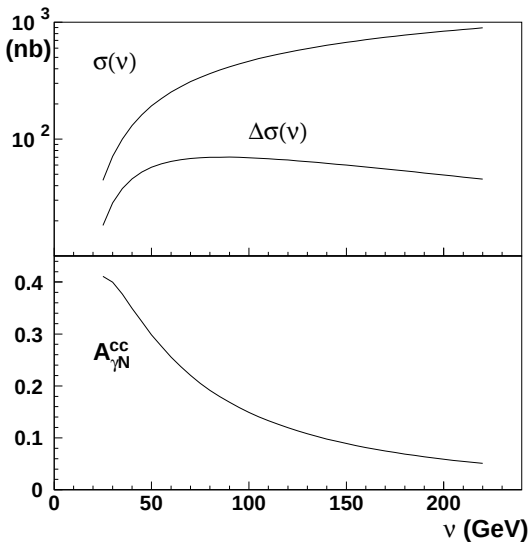

Figure 6.4: The photon-nucleon cross sections, σ and $\Delta\sigma$, (top) and the photon-nucleon asymmetry, $A_{\gamma\mathrm{N}}^{\mathrm{c\bar{c}}}$, (bottom) as a function of ν .

overlap of Δg with $\Delta\sigma$ on one hand and an as-small-as-possible overlap of g with σ on the other hand is desirable. Depending on the actual shape of Δg and g this requires a photon energy of order 80–100 GeV. For $\nu = 100$ GeV the $\hat{s}$ and x_{g} axes in Fig. 6.3 correspond to each other.

Presently, only leading-order QCD calculations of the polarised photon-gluon fusion process exist. For the unpolarised process considerable next-to-leading order corrections were found, however they are smaller than those for charm hadroproduction [238]. In the polarised case some corrections could also have opposite sign and thus reduce the asymmetry [239]. For the analysis of $\Delta g/g$ a next-to-leading order calculation is needed.

The cross section for muoproduction of open charm is given by

$$\frac{\mathrm{d}^2\sigma^{\mu\mathrm{N}\to\mathrm{c\bar{c}}X}}{\mathrm{d}Q^2\mathrm{d}\nu} = \Gamma(E;Q^2,\nu)\,\sigma^{\gamma^\star\mathrm{N}\to\mathrm{c\bar{c}}X}(Q^2,\nu) \tag{6.4}$$

with the virtual photon flux Γ

$$\Gamma(E;Q^2,\nu) = \frac{\alpha_e}{2\pi}\frac{2(1-y)+y^2+Q^2/2E^2}{Q^2(Q^2+\nu^2)^{1/2}}. \tag{6.5}$$

The virtual-photon cross section for charm production, $\sigma^{\gamma^\star\mathrm{N}\to\mathrm{c\bar{c}}X}(Q^2,\nu)$, is related to the photoproduction cross section, $\sigma^{\gamma\mathrm{N}\to\mathrm{c\bar{c}}X}(\nu)$, by

$$\sigma^{\gamma^\star\mathrm{N}\to\mathrm{c\bar{c}}X}(Q^2,\nu) = \frac{\sigma^{\gamma\mathrm{N}\to\mathrm{c\bar{c}}X}(\nu)}{(1+Q^2/M_0^2)^2}. \tag{6.6}$$

The mass parameter $M_0 = 3.9$ GeV is known from a fit to experimental data [240] and the photoproduction cross sections $\sigma^{\gamma\mathrm{N}\to\mathrm{c\bar{c}}X}(\nu)$ were measured in several experi-

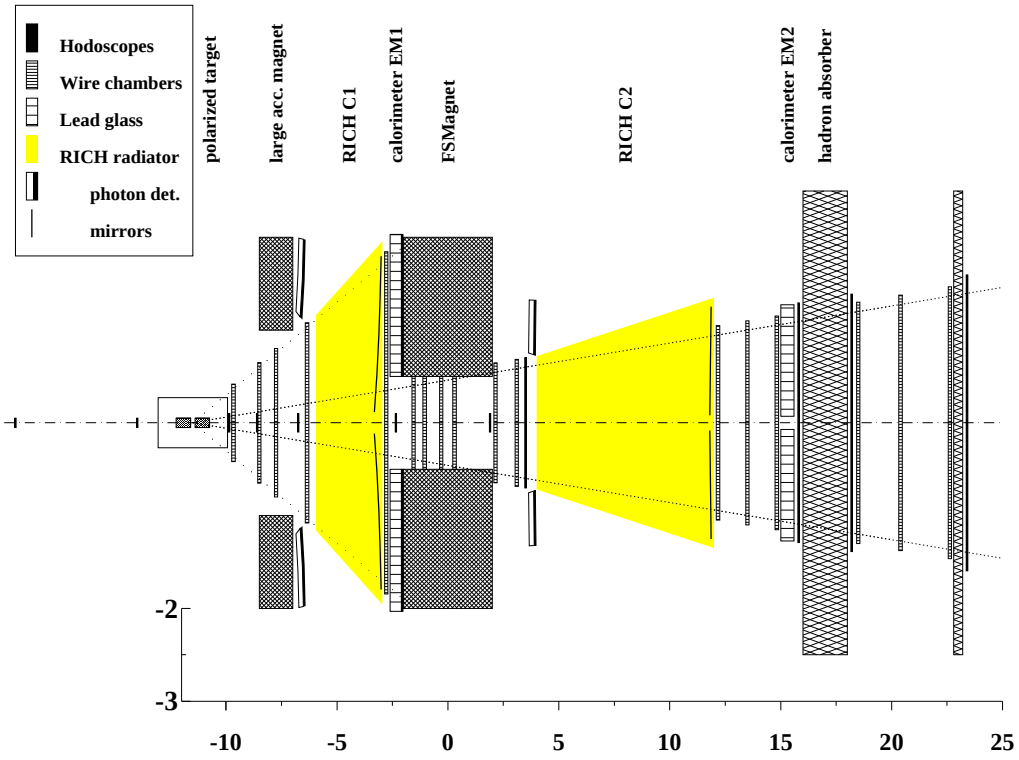

Figure 6.5: The COMPASS spectrometer as used for the muon programme.

ments (see Ref. [241] and references therein). They agree well with next-to-leading order QCD calculations involving the unpolarised gluon distribution function [238]. The charm-leptoproduction cross section is dominated by quasi-real photons and the proposed experiment takes advantage of the entire photon spectrum down to $Q^2_{\rm min} = m_\mu^2 y^2/(1-y)$.

6.1.2 The COMPASS experiment

COMPASS is a fixed-target experiment proposed at the CERN SPS using a "Common Muon and Proton Apparatus for Structure and Spectroscopy" [242]. The COMPASS physics programme is a merger of the nucleon spin structure programme with a muon beam as originally outlined in the "HMC" Letter of Intent [243] and the programme of the CHEOPS Letter of Intent [244], which focuses on charm production and light meson spectroscopy with pion, proton, and hyperon beams. Here, only the programme relevant to spin physics is discussed.

The apparatus for the muon programme (Fig. 6.5) is similar to the one of the SMC, however most components have to be rebuilt due to their age and to the rate and read-out requirements of the new experiment. The main differences in the layout are the new hadron spectrometer stage upstream of the present Forward Spectrometer Magnet (FSM) and the detectors for particle identification. The hadron stage of the spectrometer has an acceptance of ± 200 mrad for particles originating from the target centre and its new large-aperture dipole magnet provides a bending power of 1 Tm. Particle identification will be performed by ring-imaging Cherenkov counters and by electromagnetic and hadronic

calorimeters in each of the two spectrometer stages. The upstream and downstream RICH provide pion-kaon separation in the momentum range 3–65 GeV/c and 30–120 GeV/c, respectively. For the photon detection multi-wire proportional chambers with CsI photocathodes will be employed. Existing lead-glass arrays will be used for the electromagnetic calorimeters. The hadronic calorimeters will in the muon programme mainly serve trigger purposes and tag deep-inelastic events. Both spectrometer stages end with a muon wall consisting of a hadron absorber followed by tracking chambers and trigger hodoscopes. The tracking in the beam region will be performed by scintillating fibre detectors. The large angles of the produced hadrons with respect to the incoming beam also require a new polarised target solenoid with an opening of about ± 200 mrad matching that of the first spectrometer stage. As target materials lithium deuteride, ^{6}LiD, for the deuteron and ammonia, NH_3, for the proton are foreseen, polarised to 50 % and 85 %, respectively. The latter is being used successfully by the SMC in the 1996 run with polarisations of 89 %. The nuclear structure of ^{6}LiD is well described by the "alpha + deuteron" picture, which results in the favourable dilution factor (Eq. 4.5), of $f = 0.50$ compared to $f = 0.16$ for ammonia. Recently, the average polarisations of the neutron and the proton in ^{6}LiD were calculated assuming a three-body bound state of "α+p+n" [138]. The authors find polarisations of 92 % parallel to the ^{6}Li spin, which is the same as for the deuteron. The choice of the muon energy is driven by the maximum photon energy, ν, in Eq. 6.3, i.e. the minimum x_g value one wants to access. The muon energy should only be slightly larger than ν, in order to obtain a large average depolarisation factor, D, (Eq. 2.43). Along these lines a muon energy of 100 GeV appears to be the optimal choice given the present predictions for the shape of $\Delta g(x)/g(x)$. A muon intensity of 2×10^8 positive muons per spill of 2.4 s and a repetition rate of 1/14.4 s provides together with the 120 cm long double-cell target a luminosity of about $\mathcal{L} = 5 \times 10^{32}\mathrm{cm}^{-2}\mathrm{s}^{-1}$.

Charm quarks fragment preferentially into D mesons. For the kinematics of the COMPASS experiment we find in average 1.2 D^0 mesons per initial $\mathrm{c\bar{c}}$ pair and about 0.3 $\mathrm{D}^\pm$ mesons. This includes the contribution from $\mathrm{D}^\star$ mesons which decay into D mesons. The cleanest D^0 decay channels are

$$\mathrm{D}^0(\mathrm{c\bar{u}}) \to \mathrm{K}^-\pi^+ \qquad \text{and} \qquad \overline{\mathrm{D}}^0(\mathrm{\bar{c}u}) \to \mathrm{K}^+\pi^-$$

with a branching ratio of 0.0401 ± 0.0014. Mainly these channels will be used for the D identification. A major concern is the combinatorial background of kaon-pion pairs unrelated to D decays. Often the distance between the production and the decay vertex is used in charm experiments to clean up the kaon-pion sample. This technique cannot be applied in the COMPASS experiment, because this distance of 0.6–5 mm cannot be resolved due to multiple scattering in the target. Also the definition of the primary vertex is difficult because of the small scattering angle of the muon. In the D rest frame the kaon and the pion have large momenta of 861 MeV/c. For decays with large kaon angles in this reference frame with respect to the D direction in the laboratory frame, θ^*_K, this leads to rather large transverse momenta, e.g. $p_T = 750$ MeV/c for $\cos\theta^*_\mathrm{K} = 0.5$. Kaon-pion pairs from ordinary fragmentation have small transverse momenta and thus dominantly mimic decays with small θ^*_K. In Figure 6.6 the distribution of decay and of background events is shown as a function of $\cos\theta^*_\mathrm{K}$ and of the energy fraction $z_\mathrm{D} = E_\mathrm{D}/\nu$ obtained for a 40 MeV window around the D^0 mass. These distributions were obtained by Monte-Carlo simulations using the AROMA event generator [245] for the photon-gluon fusion process, for which it was particularly designed following Ref. [246]. The best result is obtained with

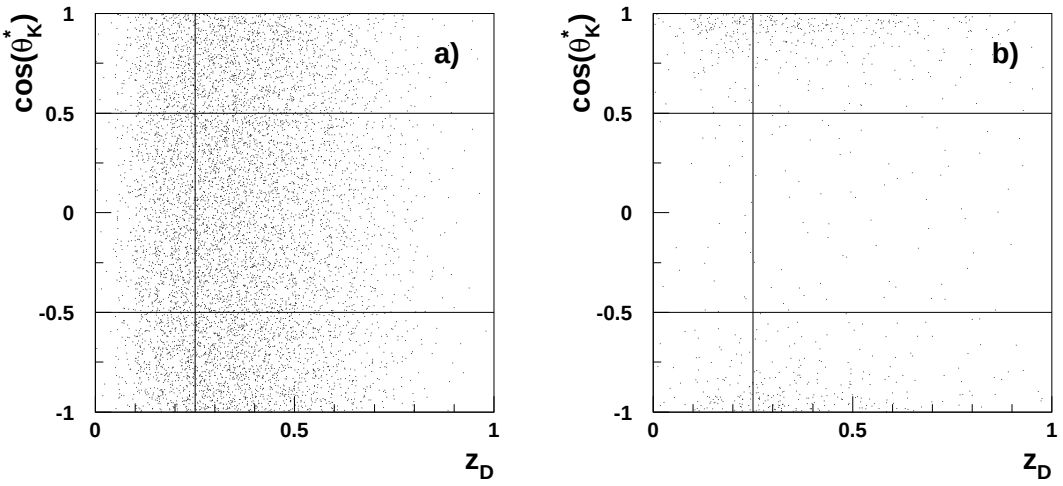

Figure 6.6: Monte-Carlo simulation: a) $D \to K\pi$ and b) combinatorial background versus z_D and $|\cos\theta^*_K|$. The lines indicates the cuts used in the rate estimates.

the requirements $|\cos\theta^*_K| \leq 0.5$ and $z_D \geq 0.25$, which improve the signal-to-background ratio by a factor 1750 on the expense of loosing 65 % of the D mesons.

As in the inclusive case the event-number asymmetry is reduced from the virtual-photon asymmetry by the depolarisation factor, D, the beam and target polarisations, P_μ and P_t, and the target dilution factor, f,

$$\frac{N^{\rightleftarrows} - N^{\rightrightarrows}}{N^{\rightleftarrows} + N^{\rightrightarrows}} = P_\mu P_t f A^{c\bar{c}}_{\mu N} \qquad \text{with} \quad A^{c\bar{c}}_{\gamma N} \simeq \frac{A^{c\bar{c}}_{\mu N}}{D} \tag{6.7}$$

where $(\rightrightarrows, \rightleftarrows)$ indicate parallel and antiparallel longitudinal polarisation of the muon and target spins, respectively. The error on the asymmetry is then given by,

$$\delta A^{c\bar{c}}_{\mu N} = \frac{1}{P_t P_\mu f \overline{D}} \frac{1}{\sqrt{N^{c\bar{c}}}} \sqrt{1 + \frac{N^B}{N^{c\bar{c}}}}, \tag{6.8}$$

with the charm and background event numbers, $N^{c\bar{c}}$ and N^B. From Eq. 6.4 we find an integrated cross section of 1.9 nb for charm leptoproduction in the range $35 \leq \nu \leq 85$ GeV. The average depolarisation factor is $\overline{D} = 0.66$. For the background we use the total quasi-real photon-nucleon cross section of 100 μb/$(1 + Q^2/0.31\ \text{GeV}^2)$ [247]. This leads with the cuts discussed above to $N^B/N^{c\bar{c}} \simeq 3.8$. For a running time of 2 1/2 years with 150 days/year and assuming a combined efficiency of 0.25 for the muon beam and the experimental apparatus the statistical error of the measured asymmetry is $\delta A^{c\bar{c}}_{\gamma N} = 0.076$. This can be improved using $D^\star$ tagging by the soft pion in the decay

$$D^{\star +} \to D^0 \pi^+_s \to (K^- \pi^+)\pi^+_s. \tag{6.9}$$

The small $D^{\star +}$–D^0 mass difference of 145.4 MeV is almost entirely accounted for by the pion mass of 139.6 MeV. Even with a moderate resolution the mass difference $\Delta M =$

$m(\mathrm{K}^-\pi^+\pi_s^+) - m(\mathrm{K}^-\pi^+)$ can be measured to a precision of 2.5 MeV providing a very clean tag for the $\mathrm{D}^\star$ meson. Considering only the soft pions with momenta larger than 1 GeV/c and taking possible re-interaction in the target into account the statistical error of the asymmetry reduces to

$$\delta A_{\gamma N}^{\mathrm{c\bar{c}}} = 0.05 \qquad \text{corresponding to} \quad \delta\frac{\Delta g}{g} = 0.14. \tag{6.10}$$

This result is shown in Fig. 6.7. The sensitivity to $\Delta g/g$ peaks at $x_\mathrm{g} = 0.14$ and covers the range $0.07 \leq x_\mathrm{g} \leq 0.4$ (Fig. 6.8). Apart from the c.m. energy, $\hat{s}$, the asymmetry for the elementary photon-gluon fusion process, $\Delta\sigma(\hat{s},\hat{\theta})/\sigma(\hat{s})$, also depends on $\hat{t}$ or on the c.m. angle, $\hat{\theta}$, between the photon-gluon axis and the $\mathrm{c\bar{c}}$ axis (Fig. 6.2) [239, 248]. The sensitivity is larger for small angles corresponding in the laboratory frame to small transverse momenta, p_T. Rejecting D mesons with $p_T > 1$ GeV/c thus leads to a smaller uncertainty of

$$\delta A_{\gamma N}^{\mathrm{c\bar{c}}} = 0.04 \qquad \text{corresponding to} \quad \delta\frac{\Delta g}{g} = 0.11. \tag{6.11}$$

The three and four-body decay channels

$$\begin{array}{lll} \mathrm{D}^0 & \rightarrow & \mathrm{K}^-\pi^+\pi^\circ \qquad (13.8\ \%) \\ \mathrm{D}^0 & \rightarrow & \mathrm{K}^-\pi^+\pi^+\pi^- \qquad (\ 8.1\ \%) \\ \mathrm{D}^+ & \rightarrow & \mathrm{K}^-\pi^+\pi^+ \qquad (\ 9.1\ \%) \end{array}$$

may further improve the precision, in particular if the $\mathrm{D}^\star$ tagging can be used. This is still under investigation.

A measurement of the transversity structure function, $h_1(x)$, is also foreseen using a transversely polarised target. In the quark parton model $h_1(x)$ is given by

$$h_1(x) = \frac{1}{2}\sum_i e_i^2 \left\{\Delta_T q(x) + \Delta_T \bar{q}(x)\right\}. \tag{6.12}$$

The parton distribution functions, $\Delta_T q(x)$, are related to the difference of the probabilities to find in a transversely polarised nucleon partons with a polarisation parallel and antiparallel to the nucleon spin. This twist-two structure function involves tensor currents and has an odd-chirality structure related to a spin-flip amplitude. In inclusive electromagnetic scattering it is suppressed by a factor $m_q/\sqrt{Q^2}$ because the chirality along the quark line in the corresponding "hand-bag diagram" can only be flipped by a quark-mass insertion. The insertion of the fragmentation process interrupts the quark line and h_1 can thus contribute in semi-inclusive scattering weighted by the corresponding fragmentation function. Also in Drell–Yan production of lepton pairs h_1 can be measured because the left and the right-handed quarks exchanged between the two nucleons follow different lines. A systematic discussion of the twist and chirality structure of the fragmentation and structure functions is given in Ref. [30]. In non-relativistic quark models g_1 and h_1 are identical. Bag model predictions indicate that h_1 could even be larger than g_1 [249]. Recently, also a calculation of the tensor charge — the difference of the quark and antiquark first moments of h_1 — was performed in lattice QCD [218]. The result also indicates that h_1 is large, see Sect. 5.8.

The proposed measurement of h_1 makes use of the spin dependence of the fragmentation process to obtain information on the polarisation of the struck quark. A complete

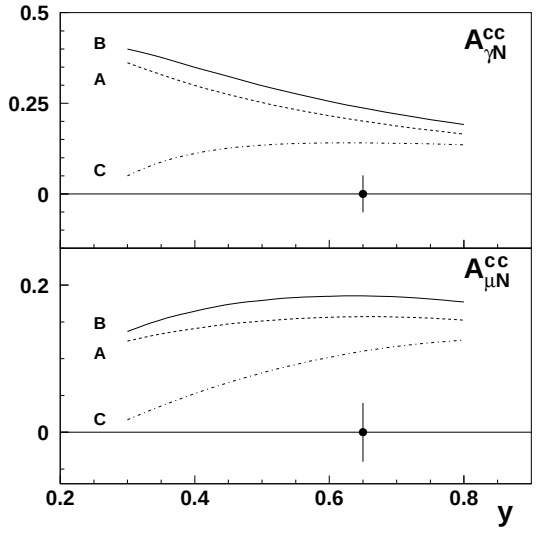

Figure 6.7: Photon-nucleon asymmetry, $A_{\gamma N}^{c\bar{c}}$ (top), and muon-nucleon asymmetry, $A_{\mu N}^{c\bar{c}}$ (bottom), as a function of $y = \nu/E$. The curves correspond to the gluon distributions of Ref. [236]. The data points shown at $A^{c\bar{c}} = 0$ indicate the projected precision of the COMPASS measurement.

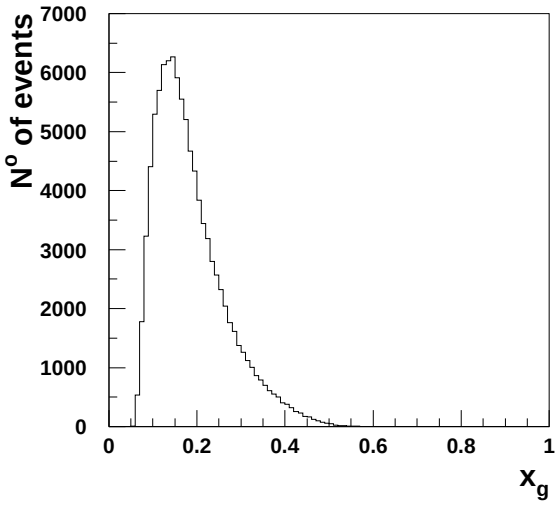

Figure 6.8: Number of accepted photon-gluon fusion events as a function of x_g for the range $35 \leq \nu \leq 85$ GeV.

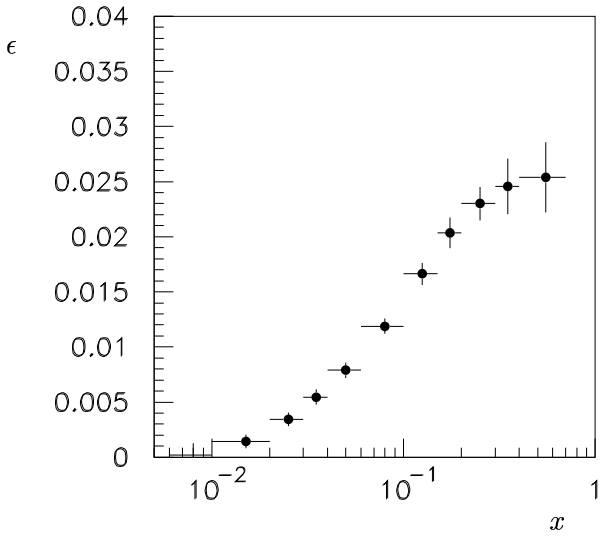

Figure 6.9: The asymmetry ϵ as a function of x as projected for the COMPASS experiment.

classification of all distribution and fragmentation functions up to twist three and including the intrinsic transverse momenta of the quarks is given in Ref. [200]. Maybe the most promising observable is the azimuthal distribution of leading pions in the plane perpendicular to the momentum transfer as originally suggested by Collins [250]. The analysing power, a_c, of this effect is unknown, however calculations in several models indicate that it should be large. The model of Ref. [251], which reproduces the pion asymmetries as measured by the E704 collaboration [252], was used in the COMPASS proposal. The amplitude of the azimuthal modulation is given by the asymmetry

$$\epsilon \simeq f P_t D_{nn} a_c \frac{h_1(x)}{F_1(x)}, \tag{6.13}$$

with the dilution factor, f, the target polarisation, P_t, and the calculable parton-level spin-transfer coefficient, D_{nn}. In Figure 6.9 a projected 30 day measurement of $\epsilon(x)$ with an NH_3 target is shown. For this projection an $h_1(x)$ parametrisation similar to $g_1(x)$ and an analysing power in the order of $a_c = 0.2$ were assumed.

Simultaneously with the measurement of Δg with longitudinal target polarisation inclusive and semi-inclusive cross-section asymmetries for $\pi^{+,-}$, $K^{+,-,0}$ will be studied. Apart from the additional information on the particle identity, a reduction of the statistical error bars by about a factor three (four) for the proton (deuteron) data is projected compared to the final SMC result at the end of 1996. For the first moments of the valence quark and antiquark distribution functions we project the errors

$$\begin{array}{lcl} \delta\Delta u_{\rm v} & = & 0.05, \\ \delta\Delta d_{\rm v} & = & 0.07, \\ \delta\Delta \bar{q} & = & 0.02, \\ \delta\Delta \bar{s} & = & 0.11. \end{array} \tag{6.14}$$

The values are compatible with those aimed at in the HERMES experiment [28], however the accessible x range extends to about a factor five smaller values for 100 GeV muon energy. This reduces the extrapolation error, which will dominate in the HERMES results.

The polarisation of lambda hyperons in both, the target and current fragmentation regions will also be studied. Large negative lambda polarisations are expected in the target fragmentation region in the polarised $s\bar{s}$ model [253]. In the current fragmentation region the spin transfer function from the struck quark to the lambda hyperon can be measured.

In summary, the COMPASS fixed-target experiment offers a rich spin-physics programme at high Q^2 with a high luminosity. Apart from the two major missing pieces of the nucleon spin structure, the gluon polarisation and the transversity structure function, many detailed questions including spin-averaged quantities like the strange-quark distribution functions can be studied.

6.2 Polarised protons at HERA

A very interesting longer-term project is a possible polarisation of the HERA 820 GeV proton beam. Self-polarisations of up to 70 % were reached for the electron beam due to the Sokolov–Ternov effect [140], which is proportional to $(E/m)^5$. However, no technique is known to polarise high-energy protons efficiently. Therefore, polarised protons must be transported through the entire accelerator chain at DESY. The feasibility of polarising the

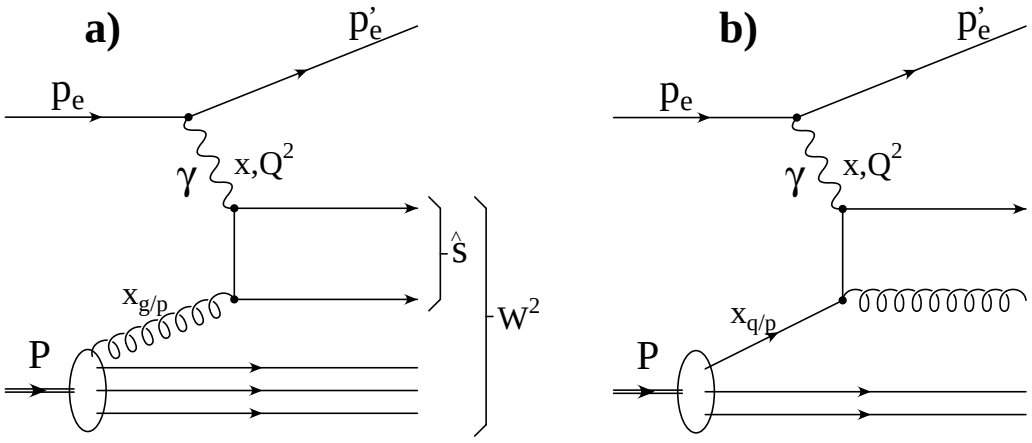

Figure 6.10: Diagrams for a) the photon-gluon fusion process and b) the QCD-Compton process.

proton beam is presently studied by a joined working group from DESY, Russia, and the USA, in the context of the *"Future Physics at HERA"* Workshop. Such a project would involve a powerful polarised H^- source, Sibirian snakes in DESY III, Petra, and HERA, and spin rotators to change from transverse to longitudinal polarisation. In addition beam polarimeters must be developed. Presently the focus is to study if a "God-given" high energetic polarised proton beam can be kept polarised in HERA for a reasonable amount of time.

Apart from polarisation, high luminosity is central issue for a possible spin-physics programme at the HERA collider as it is for future experiments with unpolarised beams. In 1995 an integrated luminosity of 12 pb^{-1} was collected, the luminosity projected for the time after a machine upgrade in 1998 is 170 pb^{-1} per year. A polarised proton beam programme could start in 2004 if technically feasible. Due to the small magnetic moment of the deuteron a polarised deuteron beam is considered to be infeasible, while a ^{3}He beam might be possible.

Three experiments are particularly promising

- a determination of Δg from jet production,
- a measurement of g_1 at high Q^2 and small x, and
- parity violating structure functions.

The H1 collaboration has determined the unpolarised gluon distribution function from so-called (2+1) jet events [254]. The notation "+1" refers to the target jet, which disappears undetected in the beam pipe. The Feynman diagrams contributing in leading order to the cross section are shown in Fig. 6.10. Like in the COMPASS experiment the photon-gluon fusion process is exploited, however in a different kinematic region and not particularly focused on charm production. The quark-antiquark pair is produced at c.m.

energies, $\hat{s} \geq 100$ GeV^2, far above threshold leading to an opposite-sign asymmetry compared to the COMPASS kinematics. This can be seen in Fig. 6.3 for the case of a charm quark pair. In contrast to the COMPASS experiment, where normally only one charmed meson will be detected, with the H1 and ZEUS detectors both jets arising from the quark pair can be detected. From the momenta of the particles in the jets the c.m. energy of the photon-gluon subsystem, $\sqrt{\hat{s}}$, can be determined and the momentum fraction carried by the gluon, x_{g}, can be recontructed using

$$x_{\mathrm{g}} = x\left(1 + \frac{\hat{s}}{Q^2}\right), \tag{6.15}$$

where x is Bjorken's scaling variable. The kinematics covered by the unpolarised experiments is $0.002 \leq x_{\mathrm{g}} \leq 0.2$ with $0.0003 \leq x \leq 0.0015$. The background from the QCD-Compton process (Fig. 6.10b) accounts for about 25 % of the cross section within the analysis cuts. The result for the gluon distribution function is shown in Fig. 6.11 together with several other measurements. The data correspond to an integrated luminosity of 0.24 pb^{-1}. First leading-order Monte–Carlo simulations of polarised (2+1)-jet events [255] using the polarised gluon distribution from Gehrmann and Stirling (set A) show a large sensitivity to the gluon polarisation peaking around $x_{\mathrm{g}} \simeq 0.008$. After analysis cuts the accessable region is about $0.004 \leq x_{\mathrm{g}} \leq 0.08$ with cross-section asymmetries in the order of 2–4 %. With an integrated luminosity of 100 pb^{-1} and beam polarisations of 0.7 such an asymmetry could be measured with about seven standard deviation significance [256].

More demanding in terms of luminosity is a measurement of $g_1(x, Q^2)$ at HERA. A detailed study of the impact of additional g_1 data was performed [257] by extending a next-to-leading order analysis [55] of existing g_1 data to projected data in the kinematic domain of HERA. Compared to fixed-target experiments the precision of the structure function measurements at HERA is moderate and suffers in the polarised case in addition from an unfavourable depolarisation factor. In this respect an experiment at lower energies is more favourable. This is presently being studied in a workshop at the GSI, Darmstadt, where a scenario of a 5 GeV electron versus 50 GeV proton collider is duscussed. A similar project was discussed at KEK in Japan. The asymmetries at small x are expected to be very small due to the rise of F_1. Therefore the false asymmetries must be controlled at least to the 10^{-4} level. This seems feasible when bunch trains with alternating proton polarisations can be used. With an integrated luminosity in the range of 200–1000 pb^{-1} a sensible measurement could be performed in the kinematic range $5 \times 10^{-5} < x < 0.6$ and 1.8 GeV$^2 < Q^2 < 1.8 \times 10^4$GeV^2. With the present g_1 data an error on Δg of 0.4 at $Q^2 = 1$ GeV^2 is obtained in this analysis [203], which could be reduced to about 0.2 with HERA data corresponding to 1000 pb^{-1} [257].

Probably a stronger motivation for a g_1 measurement at HERA is the interest in the small-x behaviour of structure functions, which has attracted much attention since the observation of the strong increase of F_2 towards small x at HERA [258, 259]. In this respect the small-x behaviour of g_1 is as fundamental as that of F_2, although different. A study of this behaviour in the double-logarithmic approximation of perturbative QCD for the nonsinglet and singlet parts of g_1 is presented in Refs. [260,261]. It is concluded that g_1 is strongly enhanced compared to the growth expected from the Gribov–Lipatov–Altarelli–Parisi (GLAP) evolution and that the difference is larger than the one expected in the unpolarised case between the GLAP and the Balitskij–Fadin–Kuraev–Lipatov behaviour

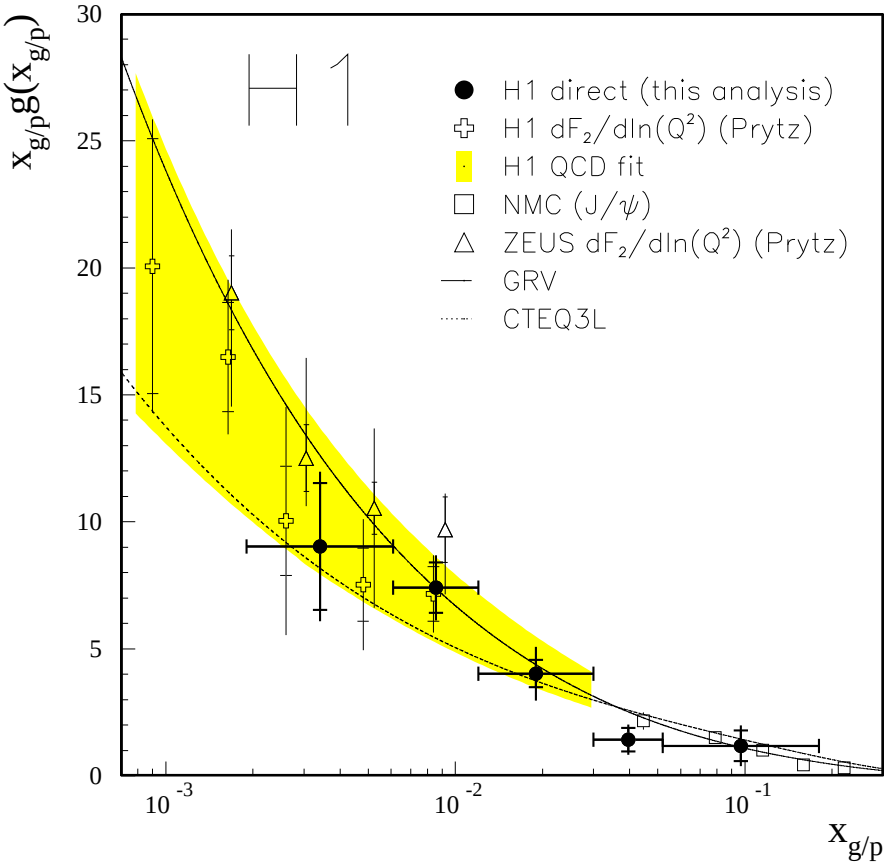

Figure 6.11: The gluon distribution function $x_{\rm g}g(x_{\rm g})$ at $Q^2 = 30$ GeV^2 as a function of $x_{\rm g}$ from several experiments. The H1 result from the (2+1)-jet analysis is shown in full circles.

Finally at high Q^2 the charged-current processes $\mathrm{e}^-\mathrm{p} \to \nu X$ and $\mathrm{e}^+\mathrm{p} \to \bar{\nu} X$ open up the possibility to access new flavour combinations and new structure functions like $g_5^{\mathrm{W}^\pm}$ (Eq. 2.69). Using electron and positron beams one could measure the combinations

$$\begin{aligned} g_1^{\mathrm{W}^-} + g_1^{\mathrm{W}^+} &= \Delta u + \Delta d + \Delta s + \Delta c, \\ g_1^{\mathrm{W}^-} - g_1^{\mathrm{W}^+} &= \Delta u_{\mathrm{v}} - \Delta v_{\mathrm{v}}, \\ g_5^{\mathrm{W}^-} + g_5^{\mathrm{W}^+} &= \Delta u_{\mathrm{v}} + \Delta d_{\mathrm{v}}, \end{aligned} \tag{6.16}$$

where Δq_{v} denotes the valence distribution functions and the (x, Q^2) dependence is omitted for simplicity. These events were studied [256, 262] for a polarised proton beam at HERA requiring a missing transverse momentum of $p_T > 25$ GeV/c for the (anti)neutrino. Due to the large asymmetries involved such a measurement is very promising for integrated luministites in excess of 100 pb^{-1}. Thus a polarised HERA is a unique tool to study the spin-flavour structure of the nucleon.

Chapter 7

Conclusions

In 1987 the EMC discovered that the matrix element of the axial singlet current, $\Delta\Sigma$, which in the quark parton model is the fraction of the nucleon's spin carried by the quark spins, is much smaller than predicted by the Ellis–Jaffe sum rules. Triggered by this discovery the Spin Muon Collaboration, the HERMES collaboration, and later the SLAC collaborations E-142 and E-143 started out with two main goals, namely the confirmation of the EMC result for the proton and the test of the fundamental Bjorken sum rule. This required an extension of the measurements of g_1^{p} to lower x and a measurement of the neutron structure function, g_1^{n}.

These objectives are now largely achieved and there remains no doubt that the Ellis–Jaffe sum rules for the proton and for the neutron are violated in a way as to satisfy the Bjorken sum rule. These conclusions are obtained independently from the SMC and the E-143 data for the proton and the deuteron. The SMC data cover the range $0.003 < x < 0.7$ with an average Q^2 of 10 GeV^2 and those from the E-143 experiment $0.029 < x < 0.8$ with $Q^2 = 3$ GeV^2. The data from the two experiments are in excellent agreement and yield $\Delta\Sigma \simeq 0.28 \pm 0.07$ and $\Delta s \simeq -0.1 \pm 0.03$. A simple averaging of the SMC and E-143 result for the Bjorken sum yields for $Q^2 = \infty$ a value of 0.198 ± 0.020 compared to the prediction of 0.2096 ± 0.004. Thus, once again the QCD predictions are found to be valid, while the nonperturbative structure of the nucleon holds surprises.

Now that the smallness of $\Delta\Sigma$ is firmly established and rather precise data are available the interest has shifted towards the rôle of the gluon polarisation and its anomalous contribution to $\Delta\Sigma$. The gluons contribute to the structure function only in next-to-leading order. In the unpolarised case the gluon distribution function was successfully determined in next-to-leading order QCD analyses of structure function data. Such analyses became possible also for the polarised case after the calculation of the two-loop splitting functions last year. Although, the precision of the polarised data is at the verge of constraining the gluon distribution function the precision and the coverage of the kinematic plane are still far from those of the unpolarised structure function data. The QCD analyses largely rely on the different average Q^2 of the SMC and SLAC data and on the very small-x data points from the SMC, where the structure functions are particularly sensitive to the gluons.

The gluon polarisation can only be determined unambiguously in processes where it appears in leading order. The measurement of such a process must be the next step in understanding the nucleon spin structure. The best candidate is the photon-gluon fusion process leading to open charm, J/ψ, or dijet production. Several activities go in this

direction. Presently the most advanced proposal is that of the COMPASS collaboration at CERN, in which the gluon polarisation is accessed via open charm production. The charm quarks are tagged by their fragmentation into D mesons and the subsequent decay into kaon-pion pairs. The projected precision for the measurement in the range $0.07 < x < 0.4$ is $\delta\Delta g/g = 0.11$.

If feasible also the option of polarising the HERA proton beam together with a considerable increase in the luminosity beyond 100 pb^{-1}/year is very exciting. The gluon polarisation could be measured from the asymmetries in dijet production. Measurements of charged-current structure functions like $g_5^{\mathrm{W}^\pm}$ could provide valuable input for the spin-flavour decomposition of the nucleon structure. Otherwise, such information can only be obtained rather indirectly via semi-inclusive scattering, where the flavour of the struck quark is tagged by the hadrons it fragments into. Precise semi-inclusive data are expected from the HERMES experiment and at a higher energy, where the factorisation ansatz is maybe better justified, from the COMPASS experiment.

A complementary approach is followed by the RHIC Spin Collaboration at the Relativistic Heavy Ion Collider in Brookhaven [263]. Here $\Delta g/g$ will be determined from prompt-photon and jet production in polarised proton-proton collisions. The measured asymmetries always involve two parton distribution functions, e.g. $\Delta g(x)$ and $\Delta q(x)$, where $\Delta q(x)$ must be known from other experiments. The covered range in x_g is about $0.03 < x_\mathrm{g} \leq 0.1$ with a maximum at 0.06. A precision in the order of $\delta\Delta g/g = 0.07$ was projected neglecting the uncertainty in $\Delta q(x)$.

Finally, for an understanding of the nucleon spin structure also the knowledge of the third twist-2 structure function, h_1, which describes the transverse polarisation of quarks in a transversely polarised nucleon, is mandatory. This structure function will be addressed by the HERMES and COMPASS experiments in semi-inclusive deep-inelastic scattering and by the RHIC Spin Collaboration in Drell–Yan dilepton production.

A clarification of the nucleon's spin-flavour structure can only be achieved by new high luminosity experiments accessing the gluon polarisation and the transversity structure function, which became the new objectives in spin structure physics. Polarised deep-inelastic scattering thus remains an exciting and most active field.

Bibliography

[1] M. Breidenbach *et al.*, Phys. Rev. Lett. **23** (1969) 935.

[2] R. Taylor, Rev. Mod. Phys. **63** (1991) 573; H. Kendall, Rev. Mod. Phys. **63** (1991) 597; J. Friedman, Rev. Mod. Phys. **63** (1991) 615.

[3] B. D. Bjorken, Phys. Rev. **179** (1969) 1547.

[4] M. Gell–Mann, Phys. Lett. **8** (1964) 214;
G. Zweig, Preprint CERN/TH-401, 412 (Geneva, 1964).

[5] R. P. Feynman, Phys. Rev. Lett. **23** (1969) 1415.

[6] D. J. Gross and F. A. Wilczek, Phys. Rev. Lett. **30** (1973) 1343;
H. D. Pollitzer, Phys. Rev. Lett. **30** (1346)

[7] G. Altarelli and G. Parisi, Nucl. Phys. B **126** (1977) 298.

[8] The EM Collaboration, J. J. Aubert *et al.*, Phys. Lett. B **123** (1983) 275.

[9] The EM Collaboration, J. Ashman *et al.*, Phys. Lett. B **206** (1988) 364.

[10] The NM Collaboration, P. Amaudruz *et al.*, Phys. Rev. Lett. **66** (1991) 2712.

[11] The E-80 Collaboration, M. J. Alguard *et al.*, Phys. Rev. Lett. **37** (1976) 1261.

[12] The E-130 Collaboration, G. Baum *et al.*, Phys. Rev. Lett. **51** (1983) 1135.

[13] V. W. Hughes and J. Kuti, Ann. Rev. Nucl. Sci. **33** (1983) 611.

[14] J. D. Bjorken, Phys. Rev. **148** (1966) 1467; Phys. Rev. D **1** (1970) 1376.

[15] V. W. Hughes, in: J. Blümlein and W.-D. Nowak, eds., Proceedings *Workshop on the Prospects of Spin Physics at Hera*, Zeuthen, Germany, August 28–31, 1995, DESY 95-200 (DESY Zeuthen, Germany, 1995) 358.

[16] J. Ellis and R. L. Jaffe, Phys. Rev. D **9** (1974) 1444; Phys. Rev. D **10** (1974) 1669.

[17] The EM Collaboration, J. Ashman *et al.*, Nucl. Phys. B **328** (1989) 1.

[18] The SM Collaboration, B. Adeva *et al.*, Phys. Lett. B **302** (1993) 533.

[19] The SM Collaboration, D. Adams *et al.*, Phys. Lett. B **329** (1994) 399; erratum Phys. Lett. B **339** (1994) 332.

[20] The SM Collaboration, D. Adams *et al.*, Phys. Lett. B **336** (1994) 125.

[21] The SM Collaboration, D. Adams *et al.*, Phys. Lett. B **357** (1995) 248.

[22] The SMC Collaboration, B. Adeva *et al.*, Phys. Lett. B **369** (1996) 93.

[23] The E-142 Collaboration, D. L. Anthony *et al.*, Phys. Rev. Lett. **71** (1993) 959.

[24] The E-143 Collaboration, K. Abe *et al.*, Phys. Rev. Lett. **74** (1995) 346.

[25] The E-143 Collaboration, K. Abe *et al.*, Phys. Rev. Lett. **75** (1995) 25.

[26] The E-143 Collaboration, K. Abe *et al.*, Phys. Lett. B **364** (1995) 61.

[27] The E-143 Collaboration, K. Abe *et al.*, Phys. Rev. Lett. **76** (1996) 587.

[28] The HERMES Collaboration, Technical Design Report, DESY-PRC 93/06, (Hamburg, Germany, July 1993).

[29] M. Gell–Mann *et al.*, Phys. Rev. **133** (1964) B145.

[30] R. L. Jaffe, in: B. Frois, N. de Groot, and V. W. Hughes, Proceedings *The Spin Structure of the Nucleon*, Erice, Italy, Aug. 3–10, 1995, (World Scientific, Singapore), to be published.

[31] M. Anselmino, A. Efremov, and E. Leader, Phys. Rep. **261** (1995) 1.

[32] B. L. Ioffe, Preprint ITEP-61-94 (Moscow, Russia, 1994), hep–ph/9408291.

[33] E. Reya, in: L. Mathelitsch and W. Plessas, eds., Proceedings *International University School of Nuclear and Particle Physics, 32nd: Substructures of Matter as Revealed with Electroweak Probes*, Schladming, Austria, Feb 24 - Mar 5, 1993, Lecture Notes in Physics 426, (Springer Verlag, 1994).

[34] A. V. Manohar, Preprint UCSD-PTH-92-10 (UC San Diego, CA, 1992), hep–ph/9204208.

[35] F. E. Close, *An Introduction to Quarks and Partons*, (Academic Press, London, U. K., 1979).

[36] F. Halzen and A. D. Martin, *Quarks and Leptons*, (Wiley, New York, 1984).

[37] C. Itzykson and J.-B. Zuber, *Quantum Field Theory*, (McGraw-Hill, New York, 1985).

[38] M. Kaku, *Quantum Field Theory*, (Oxford Univ. Press, New York, 1993).

[39] R. G. Roberts, *The Structure of the Proton*, (Cambridge Univ., Cambridge, U. K., 1990).

[40] R. L. Jaffe, Comments Nucl. Part. Phys. **19** (1990) 239.

[41] L. N. Hand, Phys. Rev. **129** (1963) 1834.

[42] M. G. Doncel and E. de Rafael, Nuovo Cim. **4A** (1971) 363.

[43] P. Hoodbhoy, R. L. Jaffe, and A. Manohar, Nucl. Phys. B **312** (1989) 571.

[44] R. L. Jaffe and A. Manohar, Nucl. Phys. B **321** (1989) 343.

[45] R. L. Jaffe and A. Manohar, Phys. Lett. B **223** (1989) 218.

[46] H. Khan and P. Hoodbhoy, Phys. Lett. B **298** (1993) 181.

[47] B. D. Bjorken and E. A. Paschos, Phys. Rev. **185** (1969) 1975.

[48] G. Altarelli, Phys. Rep. **81** (1982) 1.

[49] C. G. Callan and D. J. Gross, Phys. Rev. Lett. **22** (1969) 156.

[50] M. Anselmino, P. Gambino, and J. Kalinowski, Z. Phys. C **64** (1994) 267.

[51] The Particle Data Group, L. Montanet *et al.*, Phys. Rev. D **50** (1994) 1173.

[52] F. E. Close and R. G. Roberts, Phys. Lett. B **316** (1993) 165.

[53] V. N. Gribov and L. N. Lipatov, Sov. J. Nucl. Phys. **15** (1972) 438;
L. N. Lipatov, Sov. J. Nucl. Phys. **20** (1975) 94.

[54] Y. L. Dokshitzer, Sov. Phys. JETP **46** (1977) 461.

[55] R. D. Ball, S. Forte, and G. Ridolfi, Phys. Lett. B **378** (1996) 255.

[56] J. Kodaira, S. Matsuda, K. Sasaki, and T. Uematsu, Nucl. Phys. B **159** (1979) 99;
J. Kodaira, S. Matsuda, T. Muta, and T. Uematsu, Phys. Rev. D **20** (1979) 627.

[57] R. Mertig and W. L. van Neerven, Z. Phys. C **70** (1996) 637.

[58] W. Vogelsang, Phys. Rev. D **54** (1996) 2023.

[59] B. Lampe, Fortsch. Phys. **43** (1995) 673.
[60] Th. Gehrmann and W. J. Stirling, Phys. Lett. B **365** (1996) 347.
[61] K. G. Wilson, Phys. Rev. **179** (1969) 1499.
[62] J. Kodaira, Prog. Theo. Phys. Suppl. **120** (1995) 37.
[63] S. A. Larin, Phys. Lett. B **334** (1994) 192.
[64] J. Kodaira, Nucl. Phys. B **165** (1980) 129.
[65] S. A. Larin and J. A. M. Vermaseren, Phys. Lett. B **259** (1991) 345.
[66] A. L. Kataev and V. V. Starshenko, Mod. Phys. Lett. A **10** (1995) 235, hep–ph/9502348; Preprint CERN/TH 94-7198 (Geneva, May 1994), hep–ph/9405294.
[67] H. Burkhardt and W. N. Cottingham, Ann. Phys. **56** (1970) 453.
[68] R. Mertig and W. L. van Neerven, Z. Phys. C **60** (1993) 489.
[69] G. Altarelli , B. Lampe, P. Nason, and G. Ridolfi, Phys. Lett. B **334** (1994) 187.
[70] J. Kodaira *et al.*, Phys. Lett. B **345** (1995) 527.
[71] S. Wandzura and F. Wilczek, Phys. Lett. B **72** (1977) 195.
[72] X. Artru and M. Mekhfi, Z. Phys. C **45** (1990) 669.
[73] J. L. Cortes, B. Pire, and J. P. Ralston, Z. Phys. C **55** (1992) 409.
[74] A. V. Efremov and O. V. Teryaev, Preprint E2-88-287 (Dubna, Russia, 1988), in: J. Fischer *et al.*, eds., Proceedings *Int. Hadron Symposium*, Bechyne, Czechoslovakia, 1988, (Czech. Academy of Science, Prague, 1989) 302.
[75] R. D. Carlitz, J. C. Collins, and A. H. Mueller, Phys. Lett. B **214** (1988) 229.
[76] G. Altarelli and G. G. Ross, Phys. Lett. B **212** (1988) 391.
[77] S. I. Adler, Phys. Rev. **177** (1969) 2426; J. S. Bell and R. Jackiw, Nuovo Cim. **51A** (1969) 47.
[78] P. D. B. Collins, A. D. Martin, and E. J. Squires, *Particle Physics and Cosmology*, (Wiley & Sons, New York, 1989).
[79] M. A. Shifman, Phys. Rep. **209** (1991) 341.
[80] S. Adler and W. Bardeen, Phys. Rev. **182** (1969) 1517.
[81] R. L. Jaffe and A. Manohar, Nucl. Phys. B **337** (1990) 509.
[82] R. Clifft and N. Doble, Preprint CERN/SPSC–7412 (Geneva, 1974).
[83] N. Doble *et al.*, Nucl. Instrum. Methods A **343** (1994) 351.
[84] C. S. Wu *et al.*, Phys. Rev. **105** (1957) 1413.
[85] L. Michel, Proc. Phys. Soc. A **63** (1950) 514; C. Bouchiat and L. Michel, Phys. Rev. **106** (1957) 170.
[86] F. Combley and E. Picasso, Phys. Rep. **C14** (1974) 20.
[87] F. Scheck, Phys. Rep. **44** (1978) 187.
[88] The SM Collaboration, B. Adeva *et al.*, Nucl. Instrum. Methods A **343** (1994) 363.
[89] F. Marie, Ph. D. Thesis, Univ. Claude Bernard Lyon I, (Lyon, France, 1994).
[90] T. Gaussiran, Ph. D. Thesis, Rice University, (Houston, TX, 1994).
[91] St. Eichblatt, Ph. D. Thesis, Rice Univ., (Houston, TX, June 1996).
[92] A. M. Bincer, Phys. Rev. **107** (1957) 1434.
[93] N. de Botton, A. Daël, J. Martino, IEEE Transactions on Magnetics **30** (1994) 2447.

[94] G. Scott and H. Sturner, Phys. Rev. **184** (1969) 490.
[95] L. G. Levchuk, Nucl. Instrum. Methods A **345** (1994) 496.
[96] Ch. Iselin, CERN Yellow Report 74-17, (Geneva, 1974).
[97] A. Abragam and M. Goldman, Rep. Prog. Phys. **41** (1978) 395.
[98] T. O. Niinikoski, Nucl. Instrum. Methods **192** (1982) 151; S. C. Brown *et al.*, in: W. Meyer, ed., *4th International Workshop on Polarised Target Materials and Techniques*, (Bad Honnef, Germany, 1984) 102.
[99] N. Hayashi, Ph. D. Thesis, (Nagoya Univ., Japan, 1994).
[100] L. Klostermann, Ph. D. Thesis, Technical Univ. Delft, (Delft, The Netherlands, 1995).
[101] Ch. Dulya, Ph. D. Thesis, Univ. of California, (Los Angeles, CA, 1996).
[102] S. Bültmann, Ph. D. Thesis, (Bielefeld Univ., Germany, 1996).
[103] J. Kyynäräinen, AIP Conf. Proc. **343** (1995) 555.
[104] The SM Collaboration, B. Adeva *et al.*, Nucl. Instrum. Methods A **349** (1994) 334.
[105] The SM Collaboration, B. Adeva *et al.*, Nucl. Instrum. Methods A **372** (1996) 339.
[106] A. Daël *et al.*, IEEE Transact. on Magnetics **Vol. 28** (1992) 560.
[107] J.-M. Le Goff *et al.*, Nucl. Instrum. Methods A **356** (1995) 96.
[108] N. Hayashi *et al.*, Nucl. Instrum. Methods A **356** (1995) 91.
[109] G. R. Court *et al.*, Nucl. Instrum. Methods A **324** (1993) 433.
[110] The EM Collaboration, O. C. Allkofer *et al.*, Nucl. Instrum. Methods **179** (1981) 445.
[111] M. Litmaath, Ph. D. Thesis, NIKHEF, (Amsterdam, The Netherlands, 1996).
[112] M. Velasco, Ph. D. Thesis, Northwestern Univ., (Evanston, IL, 1995).
[113] D. Fasching, Ph. D. Thesis, Northwestern Univ., (Evanston, IL, 1996).
[114] L. Betev, Ph. D. Thesis, Ludwig Maximilian Univ., (Munich, Germany, 1996), in preparation.
[115] A. Gomez, Ph. D. Thesis, (Santiago de Compostela Univ., Spain, April 1993).
[116] M. Grosse Perdekamp, Ph. D. Thesis, Univ. of California, (Los Angeles, CA, 1995).
[117] H. Wind, Nucl. Instrum. Methods **115** (1974).
[118] A. Steinmetz, Ph. D. Thesis, Inst. f. Kernphysik, (Mainz Univ., Germany, 1996), in preparation.
[119] M. Rodriguez, Ph. D. Thesis, (Santiago de Compostela Univ., Spain, 1994).
[120] P. Shanahan, Ph. D. Thesis, Northwestern Univ., (Evanston, IL, 1995).
[121] R. Piegaia, Private Communication, 1994.
[122] U. Stiegler, Internal Note SMC/95-19, CERN, (Geneva, 1995).
[123] The SM Collaboration, B. Adeva, *et al.*, to be published in Phys. Rev. D .
[124] The NM Collaboration, P. Amaudruz *et al.*, Nucl. Phys. B **371** (1992) 3.
[125] The NM Collaboration, P. Amaudruz *et al.*, Nucl. Phys. B **441** (1995) 3.
[126] The NM Collaboration, M. Arneodo *et al.*, Nucl. Phys. B **441** (1995) 12.
[127] The E-139 Collaboration, J. Gomez *et al.*, Phys. Rev. D **49** (1994) 4348.
[128] A. A. Akhundov, D. Yu. Bardin, and N. M. Shumeiko, Sov. J. Nucl. Phys. **26** (1977) 660; *ibid.* **44** (1986) 988; JINR Dubna preprints E2–10147 (1976), E2–10205 (1976), E2–86–104 (1986); D. Yu. Bardin and N. M. Shumeiko, Sov. J. Nucl. Phys. **29** (1979) 499.

[129] T. V. Kukhto and N. M. Shumeiko, Nucl. Phys. B **219** (1983) 412; I. V. Akushevich and N. M. Shumeiko, J. Phys. G **20** (1994) 513.

[130] G. Gracia, talk at *XXXIst Rencontres de Moriond, "QCD and High Energy Hadronic Interactions"*, Les Arcs, France, March 23–30, 1996.

[131] The SM Collaboration, B. Adeva, *et al.*, to be published in Phys. Lett. B.

[132] L. Betev, Contribution to *Int. Workshop on Deep Inelastic Scattering and related Phenomena (DIS96)*, Roma, Italy, April 15–19, 1996.

[133] The NM Collaboration, M. Arneodo *et al.*, Phys. Lett. B **364** (1995) 107.

[134] L. W. Whitlow *et al.*, Phys. Lett. B **250** (1990) 193.

[135] D. De Schepper, Contribution to *Int. Workshop on Deep Inelastic Scattering and related Phenomena (DIS496)*, Roma, Italy, April 15–19, 1996.

[136] T. E. Chupp *et al.*, Phys. Rev. C **45** (1992) 915.

[137] G. G. Petrakos *et al.*, Preprint SLAC-PUB-5678 (Stanford, CA, 1991).

[138] N. W. Schellingerhout *et al.*, Phys. Rev. C **48** (1993) 2714.

[139] M. Düren, *The HERMES Experiment: From the Design to the First Results*, Habilitationsschrift, Universität Erlangen–Nürnberg, (Erlangen, Germany, 1995).

[140] A. A. Sokolov and I. M. Ternov, Sov. Phys. Doklady **8** (1964) 1203.

[141] D. P. Barber *et al.*, Phys. Lett. B **343** (1995) 436.

[142] F. Stock *et al.*, Nucl. Instrum. Methods A **343** (1994) 334.

[143] K. Lee *et al.*, Phys. Rev. Lett. **70** (1993) 738.

[144] J. Kuti and V. F. Weisskopf, Phys. Rev. D **4** (1971) 3418.

[145] R. Carlitz and J. Kaur, Phys. Rev. Lett. **38** (1977) 673; *ibid.* **38** (1977) 1102; J. Kaur, Nucl. Phys. B **128** (1977) 219.

[146] M. Glück, E. Reya, M. Stratmann, and W. Vogelsang, Phys. Rev. D **53** (1996) 4775.

[147] M. Stratmann, Z. Phys. C **60** (1993) 763.

[148] X. Song and J. S. McCarthy, Phys. Rev. D **49** (1994) 3169, erratum *ibid.* **50** (1994) 4718.

[149] X. Song, Phys. Rev. D **54** (1996) Number 1.

[150] The E665 Collaboration, M. R. Adams *et al.*, Phys. Rev. Lett. **75** (1995) 1466.

[151] W. Buck and F. Gross, Phys. Rev. D **20** (1979) 2361; M. Z. Zuilhof and J. A. Tjon, Phys. Rev. C **22** (1980) 2369; M. Lacombe *et al.*, Phys. Rev. C **21** (1980) 861; R. Machleidt *et al.*, Phys. Rep. **149** (1987) 1; A. Yu. Umnikov *et al.*, Preprint Alberta-Thy-29-94 (University of Alberta, 1994).

[152] R. M. Woloshyn, Nucl. Phys. A **496** (1989) 749.

[153] C. Ciofi degli Atti, S. Scarpetta, E. Pace, and G. Salmè, Phys. Rev. C **48** (1993) R968.

[154] S. A. Kulagin, W. Melnitchouk, G. Piller, and W. Weise, Phys. Rev. C **52** (1995) 932.

[155] The NM Collaboration, P. Amaudruz *et al.*, Z. Phys. C **51** (1991) 387.

[156] D. Day *et al.*, Phys. Rev. Lett. **43** (1979) 1143.

[157] C. J. Benesh and J. P. Vary, Phys. Rev. C **44** (1991) 2175.

[158] R. L. Heimann, Nucl. Phys. B **64** (1973) 429.

[159] J. Ellis and M. Karliner, Phys. Lett. B **213** (1988) 73.

[160] The H1 Collaboration, U. Straumann, in: J. Lemonne, C. Vander Velde, and F. Verbeure, eds., Proceedings*Int. Europhysics Conf. on High Energy Physics*, Brussels, Belgium, 27 July – 2 Aug., 1995, (World Scientific, Singapore, 1996) 118.

[161] S. D. Bass and P. V. Landshoff, Phys. Lett. B **336** (1994) 537.

[162] F. E. Close and R. G. Roberts, Phys. Lett. B **336** (1994) 257.

[163] A. Anselmino, B. L. Ioffe, and E. Leader, Yad. Fiz. **49** (1989) 214; Sov. J. Nucl. Phys. **49** (1989) 136.

[164] M. A. Ahmed and G. G. Ross, Phys. Lett. B **56** (1975) 385.

[165] R. D. Ball, S. Forte, and G. Ridolfi, Nucl. Phys. B **444** (1995) 287, erratum Nucl. Phys. B **449** (1995) 680.

[166] R. D. Ball and S. Forte, Phys. Lett. B **335** (1994) 77.

[167] The SMC Collaboration, B. Adeva *et al.*, Phys. Lett. B **320** (1994) 400.

[168] J. McCarthy, O. A. Rondon, and T. J. Liu, Phys. Rev. D **54** (1996) 2391.

[169] D. M. Kawall, Ph. D. Thesis, (Stanford Univ., CA, 1995).

[170] J. Ellis and M. Karliner, Phys. Lett. B **397** (1995) 397.

[171] J. Ellis, E. Gardi, M. Karliner, and M. A. Samuel, Phys. Lett. B **366** (1996) 268.

[172] V. M. Braun, in: Proceedings *XXXth Rencontres de Moriond "QCD and High Energy Hadronic Interactions"*, Les Arcs, France, March 1995, hep–ph/9505317.

[173] H. Georgi and H. D. Politzer, Phys. Rev. D **14** (1976) 1829; A. de Rújula, H. Georgi, and H. D. Politzer, Ann. Phys. **103** (1977) 315.

[174] S. Matsuda and T. Uematsu, Nucl. Phys. B **168** (1980) 181.

[175] H. Kawamura and T. Uematsu, Phys. Lett. B **343** (1995) 346.

[176] J. Chýla and J. Rameš, Phys. Lett. B **343** (1995) 351.

[177] D. J. Gross and C. H. Llewellyn Smith, Nucl. Phys. B **14** (1969) 337.

[178] The CCFR Collaboration, W. C. Leung *et al.*, Phys. Lett. B **317** (1993) 655.

[179] The CCFR Collaboration, D. A. Harris *et al.*, in: J. Tran Thanh Van, ed., Proc *XXXth Rencontres de Moriond: QCD and High Energy Hadronic Interactions*, Meribel les Allues, France, 19-25 Mar 1995, (Editions Frontières, France, 1995) 247, hep–ex/9506010.

[180] L. A. Ahrens *et al.*, Phys. Rev. D **35** (1987) 785.

[181] F. E. Close and R. G. Roberts, Phys. Rev. Lett. **60** (1988) 1471.

[182] H. J. Lipkin, Phys. Lett. B **214** (1988) 429.

[183] Z. Dziembowski and J. Franklin, J. Phys. G **17** (1991) 213.

[184] H. J. Lipkin, Phys. Lett. B **337** (1994) 157.

[185] J. Lichtenstadt and H. J. Lipkin, Phys. Lett. B **353** (1995) 119.

[186] B. Ehrnsperger and A. Schäfer, Phys. Lett. B **348** (1995) 619.

[187] P. G. Ratcliffe, Phys. Lett. B **365** (1996) 383.

[188] T. H. R. Skyrme, Proc. Roy. Soc. London, Series A **260** (1961) 127; *ibid.* **262** (1961) 237; Nucl. Phys. **31** (1962) 556.

[189] S. J. Brodsky, J. Ellis, and M. Karliner, Phys. Lett. B **206** (1988) 309.

[190] G. Kälbermann, J. M. Eisenberg, and A. Schäfer Phys. Lett. B **339** (1994) 211.

[191] G. Kälbermann and J. M. Eisenberg, Nucl. Phys. A **587** (1995) 609.

[192] R. D. Carlitz and A. V. Manohar, *Theoretical interpretation of the EMC results: Summary of the round-table discussion.*, Proceedings *Workshop "Colliders with Polarized Beams"*, Penn State, November, 1990.

[193] G. Altarelli and B. Lampe, Z. Phys. C **47** (1990) 315.

[194] W. Vogelsang, Z. Phys. C **50** (1991) 275.

[195] H.-Y. Cheng, Preprint IP-ASTP-25-95, Academia Sinica (Taipei, Taiwan, December 1995), hep–ph/9512267.

[196] W. Furmanski and R. Petronzio, Z. Phys. C **11** (1982) 293.

[197] X. Ji, J. Tang, and P. Hoodbhoy, Phys. Rev. Lett. **76** (1996) 740.

[198] R. L. Jaffe, Preprint MIT-CTP-2466 (Cambridge, MA, October 1995), hep–ph/9509279.

[199] T. C. Meng *et al.*, Phys. Rev. D **40** (1989) 769.

[200] P. J. Mulders and R. D. Tangerman, Nucl. Phys. B **461** (1996) 197.

[201] M. Glück, E. Reya, M. Stratmann, and W. Vogelsang, Phys. Rev. D **53** (1996) 4775.

[202] T. Gehrmann and W. J. Stirling, Phys. Rev. D **53** (1996) 6100.

[203] S. Forte, Contribution to *Int. Workshop on Deep Inelastic Scattering and related Phenomena (DIS96)*, Roma, Italy, April 15–19, 1996; R. Ball, S. Forte, G. Ridolfi, A. Deshpande, V. W. Hughes, and J. Lichtenstadt, Private Communication.

[204] S. J. Brodsky, M. Burkardt, and I. Schmidt, Nucl. Phys. B **441** (1994) 197.

[205] The EM Collaboration, M. Arneodo *et al.*, Nucl. Phys. B **321** (1989) 541.

[206] A. D. Martin, W. J. Stirling, and R. G. Roberts, Phys. Lett. B **306** (1993) 145.

[207] M. Glück, E. Reya, and A. Vogt, Phys. Lett. B **306** (1993) 391.

[208] The NM Collaboration, M. Arneodo *et al.*, Phys. Rev. D **50** (1994) R1.

[209] The NA51 Collaboration, A. Baldit *et al.*, Phys. Lett. B **332** (1994) 244.

[210] L. L. Frankfurt *et al.*, Phys. Lett. B **230** (1989) 141.

[211] St. Güllenstern *et al.*, Phys. Lett. B **312** (1993) 166.

[212] G. Martinelli and C. T. Sachrajda, Nucl. Phys. B **316** (1989) 355; G. Martinelli, Nucl. Phys. B (Proc. Suppl.) **9** (1989) 134.

[213] R. Altmeyer *et al.*, Phys. Rev. D **49** (1994) R3087.

[214] S. J. Dong, J.-F. Lagaë, and K. F. Liu, Phys. Rev. Lett. **75** (1995) 2096.

[215] M. Fukugita *et al.*, Phys. Rev. Lett. **75** (1995) 2092.

[216] M. Göckeler *et al.*, Phys. Rev. D **53** (1996) 2317.

[217] K. F. Liu, S. J. Dong, T. Draper, and J. M. Wu, Phys. Rev. D **49** (1994) 4755.

[218] S. Aoki, M. Doui, and T. Hatsuda, Preprint UTHEP-337 (Tsukuba Univ., Japan, June 1996), hep–lat/9606006.

[219] I. I. Balitsky, V. M. Braun, and A. V. Kolesnichenko, Phys. Lett. B **242** (1990) 245, erratum *ibid.* **318** (1993) 648.

[220] E. Stein, P. Górnicki, L. Mankiewicz, A. Schäfer, and W. Greiner, Phys. Lett. B **343** (1995) 369.

[221] X. Ji and P. Unrau, Phys. Lett. B **333** (1994) 228.

[222] R. L. Jaffe and X. Ji, Phys. Rev. D **43** (1991) 724.

[223] F. N. Steffens, H. Holtmann, and A. W. Thomas, Phys. Lett. B **358** (1995) 139.

[224] E. Stein, P. Górnicki, L. Mankiewicz, and A. Schäfer, Phys. Lett. B **353** (1995) 107.

[225] E. V. Shuryak and A. I. Vainshtein, Nucl. Phys. B **199** (1982) 451; Nucl. Phys. B **201** (1982) 141.

[226] B. Ehrnsperger, L. Mankiewicz, and A. Schäfer, Phys. Lett. B **323** (1994) 439.

[227] A. Schäfer, in: J. Blümlein and W.-D. Nowak, eds., Proceedings *Workshop on the Prospects of Spin Physics at Hera*, Zeuthen, Germany, August 28–31, 1995, DESY 95-200 (DESY Zeuthen, Germany, 1995) 318.

[228] M. Virchaux and A. Milstajn, Phys. Lett. B **274** (1992) 221.

[229] K. Gottfried, Phys. Rev. Lett. **18** (1967) 1154.

[230] A. D. Watson, Z. Phys. C **12** (1982) 123.

[231] M. Glück and E. Reya, Z. Phys. C **39** (1988) 569.

[232] G. Altarelli and W. J. Stirling, Particle World **1** (1989) 40.

[233] W. Vogelsang, in: W. Buchmüller and G. Ingelman, eds., Proceedings *Workshop Physics at HERA*, DESY Hamburg, Germany, 1991(389)408

[234] The NM Collaboration, P. Amaudruz *et al.*, Nucl. Phys. B **371** (1992) 553.

[235] The EM Collaboration, J. Ashman *et al.*, Z. Phys. C **56** (1992) 21.

[236] T. Gehrmann and W. J. Stirling, Z. Phys. C **65** (1994) 461.

[237] G. A. Ladinsky, in: J. Blümlein and W.-D. Nowak, eds., Proceedings *Workshop on the Prospects of Spin Physics at Hera*, Zeuthen, Germany, August 28–31, 1995, DESY 95-200 (DESY Zeuthen, Germany, 1995) 109, hep–ph/9601287

[238] S. Frixione, M. L. Mangano, P. Nason, and G. Ridolfi, Nucl. Phys. B **341** (1994) 453.

[239] M. Karliner and R. W. Robinett, Phys. Lett. B **324** (1994) 209.

[240] The EM Collaboration, J. J. Aubert *et al.*, Phys. Lett. **167B** (1986) 127.

[241] The NA14 Collaboration, M. P. Alvarez *et al.*, Z. Phys. C **60** (1993) 53.

[242] The COMPASS Collaboration, COMPASS proposal, CERN/SPSLC 96-14, SPSC/P297 (Geneva, March 1996); CERN/SPSLC 96-30 (Geneva, May 1996).

[243] Letter of Intent, CERN/SPSLC 95-27, SPSC/I204, (Geneva, March 1995).

[244] Letter of Intent, CERN/SPSLC 95-22, SPSLC/I202, (Geneva, March, 1995).

[245] G. Ingelman, J. Rathsman, and G. Schuler, DESY preprint, AROMA version 2.1 Manual.

[246] G. A. Schuler, Nucl. Phys. B **299** (1988) 21.

[247] H. Abramowicz, E. M. Levin, A. Levy, and U. Maor, Phys. Lett. B **269** (1991) 465.

[248] A. P. Contagouris, S. Papadopoulos, and B. Kamal, Phys. Lett. B **246** (1990) 523.

[249] R. L. Jaffe and X. Ji, Nucl. Phys. B **375** (1992) 527.

[250] J. Collins, Nucl. Phys. B **396** (1993) 161.

[251] X. Artru, J. Czyzewski, and H. Yabuki, Preprint LYCEN/9423 (1994); X. Artru, Private Communication.

[252] The E704 Collaboration, D. L. Adams *et al.*, Phys. Lett. B **264** (1991) 462.

[253] J. Ellis, M. Karliner, D. E. Kharzeev, and M. G. Sapozhnikov, Phys. Lett. B **353** (1995) 319; M. Alberg, J. Ellis, and D. E. Kharzeev, Phys. Lett. B **356** (1995) 113; J. Ellis, D. E. Kharzeev, and A. Kotzinian, Z. Phys. C **69** (1996) 467.

[254] The H1 Collaboration, S. Aid *et al.*, Nucl. Phys. B **449** (1995) 3.

[255] J. Feltesse, F. Kunne, M. Maul, E. Mirkes, A. Schäfer, and Wu, Contributions to the Workshop *Future Physics at HERA*, (Hamburg, Germany, April 1996).

[256] J. Feltesse and A. Schäfer, Summary Talks for the Polarisation Working Group, Workshop *Future Physics at HERA*, (Hamburg, Germany, May 1996).

[257] A. Deshpande *et al.*, Contribution to the Workshop *Future Physics at HERA*, (Hamburg, Germany, April 1996).

[258] The H1 Collaboration, I. Abt *et al.*, Nucl. Phys. B **407** (1993) 515.

[259] The ZEUS Collaboration, M. Derrick *et al.*, Phys. Lett. B **316** (1993) 412.

[260] J. Bartels, B. I. Ermolaev, and M. G. Ryskin, Z. Phys. C **70** (1996) 273; Preprint DESY 96–025 (Hamburg, Germany, 1995), hep–ph/9603204, March 1996.

[261] J. Blümlein and A. Vogt, Preprint DESY 95–175 (Hamburg, Germany, 1995).

[262] J. Kalinowski *et al.*, M. Maul and A. Schäfer, Contributions to the Workshop *Future Physics at HERA*, (Hamburg, Germany, April 1996).

[263] The RHIC Spin Collaboration, M. Beddo *et al.*, Proposal on Spin Physics Using the RHIC polarized Collider, (BNL, Upton, NY, August, 1992).

Acknowledgements

The time in the New Muon and the Spin Muon Collaboration was a great experience for me and I like to thank the members of both collaborations for the pleasant and stimulating atmosphere which was essential for the development of this work.

It gives me particular pleasure to thank our spokesman Prof. Dr. Vernon W. Hughes from whose knowledge and experience I greatly profited.

I appreciated very much the enthusiasm and competence of the Ph. D. students in the SMC, who made co-ordinating the experiment a pleasure despite the efforts it required.

CERN I like to thank for support during part of my time as contactman.

Particulièrement, j'aimerais remercier Liz Cumiskey, Yolande Camp, and Lynn Veronneau pour tout leurs efforts. Elles ont rendu la vie quotidienne au CERN beaucoup plus facile. Leurs fameux *Collaboration Barbecues* étaient très important pour la vie sociale de notre groupe. Un grand merci aussi à Jean-Marc Demolis, qui a fait l'impossible possible dans la experience.

Den Mitgliedern der Mainzer Arbeitsgruppe in der NMC und SMC danke ich für die gute und konstruktive Zusammenarbeit.

Insbesondere gilt mein Dank Herrn Prof. Dr. Th. Walcher, auf dessen Anregung hin ich die Arbeit in der NMC begann und der mir auch die Möglichkeit dazu bot.

Herrn Prof. Dr. D. von Harrach danke ich ganz herzlich für viele bereichernde Diskussionen bereits während seiner Zeit als Sprecher der NMC und für die Möglichkeit, innerhalb der SMC die Arbeiten auf den Gebiet der tiefinelastischen Streuung fortsetzen zu können. Von seinem Weitblick und Enthusiasmus habe ich in vielerlei Hinsicht gelernt.

Meiner Frau und meinen Kindern, denen ich viel Zeit schulde, danke ich für ihr Verständnis und ihre Unterstützung.